

UNIVERSITY OF OKLAHOMA  
GRADUATE COLLEGE

UAV-BASED IN SITU ANTENNA CHARACTERIZATION: ANALYSIS AND  
DESIGN REQUIREMENTS

A THESIS

SUBMITTED TO THE GRADUATE FACULTY

in partial fulfillment of the requirements for the

Degree of

MASTER OF SCIENCE

By

SIMON DUTHOIT  
Norman, Oklahoma  
2018

UAV-BASED IN SITU ANTENNA CHARACTERIZATION: ANALYSIS AND  
DESIGN REQUIREMENTS

A THESIS APPROVED FOR THE  
SCHOOL OF ELECTRICAL AND COMPUTER ENGINEERING

BY

---

Dr. Jorge Salazar-Cerreño, Chair

---

Dr. Caleb Fulton

---

Dr. Phillip Chilson

---

Dr. Djordje Mirković



## Acknowledgments

First and foremost, I would like to express my gratitude and thanks to some people who have contributed in various ways to this thesis. I am grateful to all my committee members for their time, patience, and invaluable insight on this work. An extra mention to Jorge Salazar for supporting me throughout the entirety of my graduate studies, and giving me this great opportunity at the ARRC in the first place.

I also owe my graduate achievements to my wife, Betsy, who has been a great source of support, and more simply an unwavering shoulder to rest on all along. On a broader scale, and despite the distance that has kept us apart for almost 4 years, I am eternally indebted to my parents who have done their best and made many sacrifices to shape me into who I am, and without whom I would not have made it thus far.

Last but definitely not least, some of the friendships that I have had the privilege to share with some great people have also been important to this success. Here in the USA, Paulius and Braden have been great sources of support. Back on my native Old Continent, Remi, Damien, Mathieu, Fabien, Justine, Camille, Oussama, Ismail and Adnane have each contributed to my success and happiness, cheers to this awesome bunch. The prestige of being the last person in this section is bestowed upon Cedric, who is my first friend from college. Exchanging daily morale boosts and jokes helps the day to be better. I have no doubt about success in his own graduate studies.

# Table of Contents

<b>Acknowledgments</b>	<b>iv</b>
<b>List Of Tables</b>	<b>vii</b>
<b>List Of Figures</b>	<b>viii</b>
<b>Abstract</b>	<b>xv</b>
<b>1 Introduction</b>	<b>1</b>
1.1 Motivation . . . . .	1
1.2 Literature Review . . . . .	2
1.3 Proposed System . . . . .	7
1.4 Organization of the Thesis . . . . .	8
<b>2 System Requirements</b>	<b>10</b>
2.1 Antenna Requirements . . . . .	10
2.1.1 Frequency Bands and Applications . . . . .	10
2.1.2 Weather and Surveillance Radars . . . . .	16
2.1.3 Communication Systems . . . . .	18
2.2 Measurement Requirements . . . . .	20
2.2.1 Phase . . . . .	22
2.2.2 Amplitude . . . . .	27
2.2.3 Ground Reflections . . . . .	31
2.2.4 Link Budget . . . . .	35
2.3 Summary . . . . .	38
<b>3 Design Considerations and Tradeoffs</b>	<b>40</b>
3.1 Scan Types . . . . .	40
3.2 Ground Reflections . . . . .	49
3.3 Positioning Accuracy . . . . .	60
3.3.1 Inertial Measurement Unit . . . . .	60
3.3.2 Standard Global Positioning System . . . . .	63
3.3.3 Real Time Kinematics Global Positioning System . . . . .	66
3.3.4 Gimbal . . . . .	69
3.3.5 Effect on the measurements . . . . .	73
3.4 Structural Effects on the Probe's RF Performance . . . . .	76
3.4.1 Platform Comparison with $3 \times 3$ Array . . . . .	78
3.4.2 Hexacopter with $3 \times 3$ Array . . . . .	86
3.4.3 $2 \times 2$ Array . . . . .	94

3.5	Summary . . . . .	96
<b>4</b>	<b>UAV Design</b>	<b>98</b>
4.1	Classification . . . . .	98
4.2	Model and Components . . . . .	102
4.2.1	Dynamics . . . . .	102
4.2.2	Block Diagram . . . . .	104
4.3	Design . . . . .	107
4.3.1	Frame and gimbal . . . . .	107
4.3.2	Propulsion Systems . . . . .	109
4.4	Other components . . . . .	113
4.5	Summary . . . . .	115
<b>5</b>	<b>Preliminary Results</b>	<b>116</b>
5.1	Setup . . . . .	117
5.2	Source Modeling . . . . .	120
5.3	Indoor Measurements . . . . .	122
5.4	Outdoor Measurements . . . . .	124
5.5	Summary . . . . .	125
<b>6</b>	<b>Conclusion</b>	<b>127</b>
	<b>Bibliography</b>	<b>133</b>
	<b>Appendix A</b>	
	Hexacopter part list . . . . .	138
	<b>Appendix B</b>	
	ATD . . . . .	139
B.1	Link Budget . . . . .	139
B.2	Scan Types . . . . .	140
B.3	Ground Reflections . . . . .	141
B.4	Positioning Accuracy . . . . .	141

# List Of Tables

1.1	Reported past in situ antenna characterization measurement campaigns using UAVs . . . . .	6
2.1	Weather and surveillance radar antenna requirements . . . . .	17
2.2	Antenna and radar systems parameters for the link budget study . . . . .	37
3.1	Summary of UAV IMU characteristics . . . . .	62
3.2	Standard deviation—in cm—for all datasets of the Emlid Reach in GPS and RTK GPS modes as well as the hexacopter with a standard GPS, along each axis. . . . .	69
3.3	Effect of the UAV position drift on $\Delta\Phi$ , $\Delta\theta$ , and $\Delta PL$ for the WSR-88D, RaXPol, and the 5G base station antenna . . . . .	75
3.4	Effect of the UAV gimbal drift on $\Delta D_p$ for a single patch antenna, a $3\times 3$ patch antenna array, and $8\times 8$ patch antenna array . . . . .	76
3.5	Maximum oscillation level (dB), from $-45$ to $45^\circ$ for the antenna patterns of the $3\times 3$ S-Band single layer FR4 microstrip array mounted on the DJI Phantom 3, hexacopter, and octocopter . . . . .	86
3.6	Maximum oscillation level (dB), from $-45$ to $45^\circ$ for the antenna patterns of the $3\times 3$ S-Band single layer FR4 microstrip array mounted on the hexacopter . . . . .	93
3.7	Maximum oscillation level (dB), from $-45$ to $45^\circ$ for the antenna patterns of the $2\times 2$ S-Band single layer FR4 microstrip array mounted on the hexacopter . . . . .	96
4.1	UAV classification . . . . .	99
4.2	UAV comparison focused on miniaturization (1 = bad, 3 = good) . . . . .	100
4.3	Weight estimate of the ARRC in-house hexacopter . . . . .	111
A.1	Part list of the ARRC in-house hexacopter . . . . .	138
B.1	Effect of the UAV position drift on $\Delta\Phi$ , $\Delta\theta$ , and $\Delta PL$ for the ATD . . . . .	141

# List Of Figures

1.1	Illustration of the proposed system for in situ antenna characterization. a) The UAV flies around the radar system/antenna to carry out measurements. b) The drone hovers while the radar system/antenna rotates to carry out measurements. . . . .	8
2.1	Illustration of the FF measurement configuration. . . . .	23
2.2	FF distance versus frequency for 3 given uniform square aperture antennas ( $\theta_3 = 2, 10$ and $100^\circ$ ), and for 3 different phase error requirements ( $\Delta\phi = 5.625, 11.25$ and $22.5^\circ$ ). . . . .	24
2.3	Aperture phase taper versus normalized aperture coordinates for a uniform square aperture, and 3 different FF phase error requirements ( $\Delta\phi = 5.625, 11.25$ and $22.5^\circ$ ). . . . .	26
2.4	Effect of 3 different FF phase error requirements ( $\Delta\phi = 5.625, 11.25$ and $22.5^\circ$ ) on the principal plane antenna pattern of a $40 \times 40 \lambda$ uniform square aperture with a Taylor $\bar{n} = 6, -40$ dB distribution. . . . .	27
2.5	Illustration of the probe's antenna pattern projection onto the AUT's aperture. . . . .	28
2.6	Projected beamwidth onto a uniform square aperture and electric field of a single patch antenna and a $3 \times 3$ uniform array of patch antennas ( $\frac{\lambda}{2}$ spacing) at its edge, versus its beamwidth. . . . .	30
2.7	Projected beamwidth onto a uniform square aperture and electric field of a single patch antenna and a $3 \times 3$ uniform array of patch antennas ( $\frac{\lambda}{2}$ spacing) at its edge, versus its beamwidth. A minimum of 10 m for the FF distance was used. . . . .	31
2.8	Propagation model between the probe and the AUT for FF measurements. . . . .	32
2.9	Normalized horizontal electric field magnitude at the AUT versus probe height (distance of 400 m and AUT height of 10 m) and distance (probe height of 6 m and AUT height of 10 m), in the presence of ground reflections. . . . .	34
2.10	Normalized vertical electric field magnitude at the AUT versus probe height (distance of 400 m and AUT height of 10 m) and distance (probe height of 6 m and AUT height of 10 m), in the presence of ground reflections. . . . .	35

2.11	Link budget (SNR) for the WSR-88D versus its antenna gain—blue, RaXPoI versus its antenna gain—red, and 5G 30-dBi gain antenna versus its gain—yellow. Parameters for these antennas are summed up in table 2.2. The FF distances were chosen according to the $8\frac{a^2}{\lambda}$ criterion for accurate sidelobe level measurements. Concerning the 5G antenna, a distance of 100 m was used, which is within the coverage of a 5G base station. A 12-dBi 3×3 patch antenna array was used, and the noise floor is -80 dBW. . . . .	38
3.1	Illustration of the possible and common scan types with the UAV-based system. The first row illustrates planar scans, along $x$ and $z$ (a), and above the antenna in the $x$ - $y$ plane (b); the second cylindrical scans and the third spherical scans in both azimuth and elevation. . .	43
3.2	The different scanning strategies illustrated with the WSR-88D at a FF distance of 1459 m. The distance to be covered is shown versus the range of angles covered for the measured cut. The time needed to cover a certain distance with the UAV is shown, for different flight speeds. a) shows the spherical scan at different elevation angles in azimuth, while the elevation scans are represented by the azimuth scan at $\theta = 90^\circ$ . b) shows the planar scan in the $x - y$ plane above the antenna. c) shows the cylindrical scan both in azimuth in elevation. d) shows the time needed for the UAV to complete a mission of a given distance, for different speeds. . . . .	46
3.3	The different scanning strategies illustrated with the RaXPoI at a FF distance of 374 m. The distance to be covered is shown versus the range of angles covered for the measured cut. The time needed to cover a certain distance with the UAV is shown, for different flight speeds. a) shows the spherical scan at different elevation angles in azimuth, while the elevation scans are represented by the azimuth scan at $\theta = 90^\circ$ . b) shows the planar scan in the $x - y$ plane above the antenna. c) shows the cylindrical scan both in azimuth in elevation. d) shows the time needed for the UAV to complete a mission of a given distance, for different speeds. . . . .	47
3.4	The different scanning strategies illustrated with the 5G base station antenna at a FF distance of 100 m. The distance to be covered is shown versus the range of angles covered for the measured cut. The time needed to cover a certain distance with the UAV is shown, for different flight speeds. a) shows the spherical scan at different elevation angles in azimuth, while the elevation scans are represented by the azimuth scan at $\theta = 90^\circ$ . b) shows the planar scan in the $x - y$ plane above the antenna. c) shows the cylindrical scan both in azimuth in elevation. d) shows the time needed for the UAV to complete a mission of a given distance, for different speeds. . . . .	48
3.5	Reflection coefficient versus incident angle for 3 different permittivities, representative of soil properties, $3 - j0$ , $10 - j2$ , and $25 - j6$ . . .	53

3.6	Incident angle $\theta_i$ for the WSR88-D, a), RaXPOL, b), and a 5G base station antenna, c). The top plot shows $\theta_i$ versus distance for 3 different values of $h_1 + h_2$ , representing low, medium, and maximum. The bottom plot shows $\theta_i$ versus $h_1 + h_2$ for the 3 different values of the measurement distance, once the FF distance, twice the FF distance, and four times the FF distance. . . . .	55
3.7	Parameters that influence the ground reflections for a $1^\circ$ 3 dB beamwidth and 30 dB sidelobe-level weather radar versus a representative range of incident angles. The top plot is the reflection coefficient for H- and V-polarizations, the middle plot is the probe directivity, and the bottom plot is the radar directivity. . . . .	56
3.8	Maximum amplitude of the total electric field received at the radar versus a representative range of incident angles, for both H- and V-polarizations. . . . .	57
3.9	Parameters that influence the ground reflections for a 30 dB 5G antenna. The top plot is the reflection coefficient for H- and V-polarizations, the middle plot is the probe directivity, and the bottom plot is the radar directivity. . . . .	58
3.10	Maximum amplitude of the total electric field received at the 5G antenna versus a representative range of incident angles, for both H- and V-polarizations. . . . .	59
3.11	Position distributions during hover mode for the in-house ARRC hexacopter. The top plot shows the position along the North, the middle plot the position along the East, and the bottom plot the position along the axis pointing toward the center of the Earth. The blue histogram represents the actual data while the red plot is the gaussian fit applied to it. . . . .	66
3.12	Comparison between RTK GPS position data and standard GPS position data for the Emlid Reach, for 2 datasets in static configuration. The top plot shows the $x - y$ plane while the bottom plot shows the $x - z$ plane. a) shows the RTK GPS dataset 1, b) shows the RTK GPS dataset 2, c) shows the GPS dataset 1, and d) shows the GPS dataset 2. . . . .	68
3.13	Received power at the MVG SH-2000 antenna terminals, when excited by the central embedded element of a S-Band single layer FR4 microstrip array at 3 GHz, mounted on the UAV's gimbal. The gimbal's motors were mechanically blocked and both antennas were aligned along their broadside directions. . . . .	71
3.14	Received power at the MVG SH-2000 antenna terminals, when excited by the central embedded element of a S-Band single layer FR4 microstrip array at 3 GHz, mounted on the UAV's gimbal. The gimbal was controlled by the flight controller and its own controller (using feedback from its own IMUs and the GPS) and both antennas were aligned along their broadside directions. . . . .	72

3.15	Illustration of the position drift effect on the antenna pattern measurements. The UAV measures the AUT radiation pattern at different angles in azimuth and elevation. $\Delta\Phi$ and $\Delta\theta$ correspond to these errors respectively. . . . .	73
3.16	Illustration of the gimbal drift effect on the antenna pattern measurements. The probe mounted on the UAV excites the AUT—or receive its signal—at different angles in azimuth and elevation. $\Delta\Phi$ and $\Delta\theta$ correspond to these errors respectively. . . . .	73
3.17	Effect of the DJI Phantom 3 structure on the antenna pattern: single cell of a single layer FR4 microstrip array, horizontally polarized. (a) Current density on the probe and the UAV structure. (b) E-Plane antenna patterns with and without the UAV (red and blue respectively). (c) D-Plane antenna patterns with and without the UAV (red and blue respectively). (d) H-Plane antenna patterns with and without the UAV (red and blue respectively). . . . .	79
3.18	Effect of the DJI Phantom 3 UAV structure on the antenna pattern: single cell of a single layer FR4 microstrip array, vertically polarized. (a) Current density on the probe and the UAV structure. (b) E-Plane antenna patterns with and without the UAV (red and blue respectively). (c) D-Plane antenna patterns with and without the UAV (red and blue respectively). (d) H-Plane antenna patterns with and without the UAV (red and blue respectively). . . . .	80
3.19	Effect of the hexacopter UAV structure on the antenna pattern: central embedded element of a $3\times 3$ S-Band single layer FR4 microstrip array, horizontally polarized. (a) Current density on the probe and the UAV structure. (b) E-Plane antenna patterns with and without the UAV (red and blue respectively). (c) D-Plane antenna patterns with and without the UAV (red and blue respectively). (d) H-Plane antenna patterns with and without the UAV (red and blue respectively). . . . .	81
3.20	Effect of the hexacopter UAV structure on the antenna pattern: central embedded element of a $3\times 3$ S-Band single layer FR4 microstrip array, vertically polarized. (a) Current density on the probe and the UAV structure. (b) E-Plane antenna patterns with and without the UAV (red and blue respectively). (c) D-Plane antenna patterns with and without the UAV (red and blue respectively). (d) H-Plane antenna patterns with and without the UAV (red and blue respectively). . . . .	82
3.21	Effect of the octocopter UAV structure on the antenna pattern: central embedded element of a $3\times 3$ S-Band single layer FR4 microstrip array, horizontally polarized. (a) Current density on the probe and the UAV structure. (b) E-Plane antenna patterns with and without the UAV (red and blue respectively). (c) D-Plane antenna patterns with and without the UAV (red and blue respectively). (d) H-Plane antenna patterns with and without the UAV (red and blue respectively). . . . .	83

3.22	Effect of the octocopter UAV structure on the antenna pattern: central embedded element of a $3\times 3$ S-Band single layer FR4 microstrip array, vertically polarized. (a) Current density on the probe and the UAV structure. (b) E-Plane antenna patterns with and without the UAV (red and blue respectively). (c) D-Plane antenna patterns with and without the UAV (red and blue respectively). (d) H-Plane antenna patterns with and without the UAV (red and blue respectively).	84
3.23	Effect of the UAV structure on the antenna pattern: central row of a $3\times 3$ S-Band single layer FR4 microstrip array, horizontally polarized. (a) Current density on the probe and the UAV structure. (b) E-Plane antenna patterns with and without the UAV (red and blue respectively). (c) D-Plane antenna patterns with and without the UAV (red and blue respectively). (d) H-Plane antenna patterns with and without the UAV (red and blue respectively).	87
3.24	Effect of the UAV structure on the antenna pattern: central row of a $3\times 3$ S-Band single layer FR4 microstrip array, vertically polarized. (a) Current density on the probe and the UAV structure. (b) E-Plane antenna patterns with and without the UAV (red and blue respectively). (c) D-Plane antenna patterns with and without the UAV (red and blue respectively). (d) H-Plane antenna patterns with and without the UAV (red and blue respectively).	88
3.25	Effect of the UAV structure on the antenna pattern: central column of a $3\times 3$ S-Band single layer FR4 microstrip array, horizontally polarized. (a) Current density on the probe and the UAV structure. (b) E-Plane antenna patterns with and without the UAV (red and blue respectively). (c) D-Plane antenna patterns with and without the UAV (red and blue respectively). (d) H-Plane antenna patterns with and without the UAV (red and blue respectively).	89
3.26	Effect of the UAV structure on the antenna pattern: central column of a $3\times 3$ S-Band single layer FR4 microstrip array, vertically polarized. (a) Current density on the probe and the UAV structure. (b) E-Plane antenna patterns with and without the UAV (red and blue respectively). (c) D-Plane antenna patterns with and without the UAV (red and blue respectively). (d) H-Plane antenna patterns with and without the UAV (red and blue respectively).	90
3.27	Effect of the UAV structure on the antenna pattern: all elements of a $3\times 3$ S-Band single layer FR4 microstrip array, horizontally polarized. (a) Current density on the probe and the UAV structure. (b) E-Plane antenna patterns with and without the UAV (red and blue respectively). (c) D-Plane antenna patterns with and without the UAV (red and blue respectively). (d) H-Plane antenna patterns with and without the UAV (red and blue respectively).	91

3.28	Effect of the UAV structure on the antenna pattern: all elements of a $3\times 3$ S-Band single layer FR4 microstrip array, vertically polarized. (a) Current density on the probe and the UAV structure. (b) E-Plane antenna patterns with and without the UAV (red and blue respectively). (c) D-Plane antenna patterns with and without the UAV (red and blue respectively). (d) H-Plane antenna patterns with and without the UAV (red and blue respectively). . . . .	92
3.29	Effect of the UAV structure on the antenna pattern: all elements of a $2\times 2$ S-Band single layer FR4 microstrip array, horizontally polarized. (a) Current density on the probe and the UAV structure. (b) E-Plane antenna patterns with and without the UAV (red and blue respectively). (c) D-Plane antenna patterns with and without the UAV (red and blue respectively). (d) H-Plane antenna patterns with and without the UAV (red and blue respectively). . . . .	94
3.30	Effect of the UAV structure on the antenna pattern: all elements of a $2\times 2$ S-Band single layer FR4 microstrip array, vertically polarized. (a) Current density on the probe and the UAV structure. (b) E-Plane antenna patterns with and without the UAV (red and blue respectively). (c) D-Plane antenna patterns with and without the UAV (red and blue respectively). (d) H-Plane antenna patterns with and without the UAV (red and blue respectively). . . . .	95
4.1	The arrangement used for the dynamical model of the quadcopter, illustrated on a DJI Phantom UAV. . . . .	101
4.2	The block diagram of the in-house hexacopter at the ARRC. . . . .	104
4.3	The in-house hexacopter platform with its components shown. . . . .	106
4.4	The two most popular frame types for the quadcopter: + and X frames. The direction of rotation for each motor is also indicated—Clockwise(CW) and Counter-Clockwise (CCW). . . . .	108
4.5	The two most popular frame types for the hexacopter: + and X frames. The direction of rotation for each motor is also indicated—Clockwise(CW) and Counter-Clockwise (CCW). . . . .	109
5.1	Top view of the scanning modes for the testings. a) The UAV flies around the AUT in a circle at 0-degree elevation. b) The UAV hovers in front of the AUT at 0-degree elevation while it spins on its turntable.	116
5.2	The setup used for the preliminary measurements. A DJI Phantom 3 was equipped with an X-Band monopole, fed by a Windfreak synthesizer. The AUT is an X-Band polyrod antenna, placed on a Velmex turntable, hooked up to an RF receiver, which is composed of an amplifier board and a Fieldfox power analyzer. The turntable and the power analyzer are controlled by the computer. . . . .	117
5.3	The amplifier board and its 5 amplifiers. . . . .	118
5.4	The gain for each amplifier in the frequency range of interest. a) Minicircuits V63, b) Minicircuits V83, c) Pasernack PE1524, d) AvanteK AWT-18057, and e) Miteq AFS3. . . . .	119

5.5	The losses versus frequency for both cables: 6-foot (blue) and 33-foot (red). . . . .	120
5.6	Effect of the UAV structure on the antenna pattern: $\frac{\lambda}{4}$ monopole, vertically polarized. (a) Current density on the probe and the UAV structure. (b) E-Plane antenna patterns with and without the UAV (red and blue respectively). (c) D-Plane antenna patterns with and without the UAV (red and blue respectively). (d) H-Plane antenna patterns with and without the UAV (red and blue respectively). . . . .	121
5.7	The indoor arrangement—top—and results—bottom. The testings were carried out inside a FF anechoic chamber at the ARRC, with the setup represented in figure 5.2. The results show 4 different patterns: the probe without the UAV, the probe with the UAV off, the probe with the UAV on and not flying, and the probe with the UAV hovering.	123
5.8	The outdoor arrangement alongside the results. a) shows the UAV in the sky in the background and the AUT on its turntable and telescopic mast in the foreground. b) shows the UAV in hover mode with the corresponding antenna pattern on the right. c) shows the UAV in flight mode—circular scan, with the corresponding antenna pattern on the right. . . . .	125
B.1	Link budget (SNR) for the ATD versus its antenna gain. Parameters for these antennas are summed up in appendix B. The FF distance was chosen according to the $8\frac{a^2}{\lambda}$ criterion for accurate sidelobe level measurements. A 12-dBi $3 \times 3$ patch antenna array was used, and the noise floor is -80 dBW. . . . .	139
B.2	The different scanning strategies illustrated with the ATD at a FF distance of 341 m. The distance to be covered is shown versus the range of angles covered for the measured cut. The time needed to cover a certain distance with the UAV is shown, for different flight speeds. a) shows the spherical scan at different elevation angles in azimuth, while the elevation scans are represented by the azimuth scan at $\theta = 90^\circ$ . b) shows the planar scan in the $x - y$ plane above the antenna. c) shows the cylindrical scan both in azimuth in elevation. d) shows the time needed for the UAV to complete a mission of a given distance, for different speeds. . . . .	140
B.3	Incident angle $\theta_i$ for the ATD. The top plot shows $\theta_i$ versus distance for 3 different values of $h_1 + h_2$ , representing low, medium, and maximum. The bottom plot shows $\theta_i$ versus $h_1 + h_2$ for the 3 different values of the measurement distance, once the FF distance, twice the FF distance, and four times the FF distance. . . . .	141

# Abstract

This thesis proposes to characterize antennas in situ with Unmanned Aerial Vehicles (UAVs), especially within the framework of weather radar and 5<sup>th</sup> generation wireless systems (5G) antennas. Specifically, it is concerned with devising the requirements and tradeoffs of such a system. Characterizing an antenna in its operational environment is important to ensure that it meets its performance requirements, once it is installed in a larger system. Several techniques exist to carry out this task. Balloon-tethered dipoles at different heights were used to measure antennas radiation patterns in elevation as early as 1965. In 1988, helicopters replaced balloons and permitted the measurement of any antenna radiation pattern cut. In 2014, UAVs emerged to carry out this task for VHF and UHF antennas only, pointing at zenith, and with low directivity. However, measuring high-gain antennas pointing at low elevation angles presents more challenges, which this thesis takes into account.

First, requirements for weather radar systems as well as 5G base station antennas are listed, as well as general measurement requirements, including phase, amplitude, ground reflection, and link budget requirements. Then, the requirements and tradeoffs for characterizing antennas using UAVs are presented. The different scanning strategies are exposed, as well as the necessary distance for measuring antenna pattern cuts. The effect of ground reflections on the measurements is set forth. The positioning accuracy of a UAV platform, specifically of its Global Positioning System (GPS), Inertial Measurement Units (IMUs), and gimbal, is presented, with a focus on the in-house Advanced Radar Research Center (ARRC) hexacopter. The

effects of the UAV position and gimbal drifts on the measurements are formulated theoretically, and illustrated. Two radiating structures to be mounted on the UAV are studied—a  $3 \times 3$  and a  $2 \times 2$  dual-polarized patch antenna arrays, with different UAV platforms—the in-house ARRC hexacopter and octocopter as well as the DJI Phantom 3. Following is a presentation of the design process of a UAV platform, with an emphasis on the required performance factors pertaining to in situ antenna characterization. Finally, a proof of concept of this system is shown, using a commercially available UAV—DJI Phantom 3—equipped with a quarter wavelength monopole antenna that measures a custom traveling wave antenna.

# Chapter 1

## Introduction

### 1.1 Motivation

Characterizing various properties of antennas, such as gain, polarization, and radiation pattern for example, is a crucial step to determine if a given antenna meets its performance requirements before it is implemented in a larger system. It is also of utmost importance once the antenna has been integrated in its final system, to ascertain whether the performance requirements are still met. The main figure of merit for an antenna is its radiation pattern, which, like its name suggests, tells one how much energy is radiated in a given direction. Antenna ranges are the type of facilities that are used to measure radiation patterns as well as other properties. More precisely, antenna ranges are a combination of space and instrumentation, where a source excites the antenna whose radiation pattern is measured, typically called Antenna Under Test (AUT). Numerous types of antenna ranges exist, such as slant ranges, compact ranges, and anechoic chambers for example. The reader can refer to [1] for more information about antenna ranges and their design.

When an antenna is measured in an antenna range, its operational environment is not included. More precisely, the operational environment encompasses phenomena and equipment such as ground and environmental reflections, pedestal, radomes,

temperature, and backend Radio Frequency (RF) equipment for example. However, the operational environment of an antenna affects its radiation pattern and other characteristics. But, due to constraints such as size, mobility, and cost, it is not always possible to measure an antenna in its operational environment. Consequently, this brings up the need to find a method which would permit this type of measurement despite the previously evoked limiting factors. This is especially true at the Advanced Radar Research Center (ARRC), which has developed several mobile radar systems over the years, which are AIR [2], RaXPol [3], PX-1000 [4], and CP-PAR [5]. Characterizing these radars in situ is crucial in order to obtain reliable weather data.

## 1.2 Literature Review

Decades ago, researchers came up with methods to characterize antennas in situ without the aid of antenna ranges. As early as in 1965, tethered balloons measurements were implemented to measure antenna patterns in-situ. In [6], a dipole is tethered to a balloon that can float at different heights and excites the AUT which is a 16-MHz array—High Frequency (HF). The transmitting dipole is located at distances ranging between 800 and 1500 meters away from the AUT. The goal is to measure the vertical radiation pattern of the main azimuthal lobe, therefore the AUT was rotating around its axis and reading the maximum received power for different elevation angles, which are symbolized by different heights of the tethered transmitting dipole. Theodolites measurements permitted accurate elevation angle

readings within 1 degree. At angles where ground reflections did not affect the measurements, the latter agreed within 1 decibel.

Twenty-three years later, in 1988, an airborne measurement method for antenna radiation patterns emerged, in [7] and [8], using helicopters, within the framework of telecommunication antennas, at Very High Frequency (VHF) and Ultra High Frequency (UHF). The measurements of interest are the gain, Horizontal Radiation Patterns (HRP), which are azimuthal patterns at given elevation angles, and Vertical Radiation Patterns (VRP), which are elevation patterns at given azimuth angles. The derived technique consists in hanging a receiving antenna, as isotropic as possible, under a helicopter that follows different flight patterns, whose field strength—coming from the exciting AUT—is measured. A ground-based navigation system constantly determines the position of the helicopter, so that the error on the measured antenna patterns is within half a decibel, and feeds it to the helicopter where, along the field strength measurements, they are recorded for post-processing. As far as VRPs are concerned, the helicopter carries out a vertical ascent to a peak height at a given distance from the antenna, and possibly proceeds to fly horizontally at that peak height toward the antenna, if higher elevation angles are needed. Concerning HRPs, the helicopter flies in a circular pattern around the antenna at a given height. This technique allowed these telecommunication companies to determine whether their antennas were radiating in the right direction with the right gain, which are precious pieces of information to ensure compliance with regulations, cost-effectiveness, and good coverage.

The techniques mentioned so far can be costly and hard to implement. A Near Field (NF) technique to measure antennas was implemented in [9], consisting of a probe mounted on a mast exciting the AUT from above, which is a VHF/UHF antenna array pointing at zenith. The mast has to be manually moved to different positions to get different points for the NF scan. This technique, albeit tedious, is a much cheaper alternative to airborne measurements. The downside is that the Far Field (FF) is far away at these frequencies, which means that only NF measurements can be carried out manually. An algorithm transforming NF measurements to FF radiation patterns has to be used as an extra step, to obtain the antenna radiation pattern.

In the past few years, Unmanned Aerial Vehicles (UAVs) have become readily available and cheap, and are now able to perform arbitrary autonomous flights for more than 15 minutes while carrying payloads of a few pounds. Therefore, UAVs with probes and generators aboard have become a strong candidate for characterizing antennas in situ. The first published working implementation of this application can be seen in [10]. The authors' goal was to devise a UAV-based system to verify antenna patterns of a VHF/UHF array. The method set forth in the paper revolves around a UAV equipped with its own Global Positioning System (GPS) and Inertial Measurement Unit (IMU), which is therefore able to perform autonomous flights given user-defined flight paths. The UAV is also equipped with a generator/antenna (variable-length dipole) pair that excites the AUT, and retroreflectors, which enable the drone's position to be accurately measured with a motorized total station, whose accuracy is 1 centimeter for distances and 0.6 minute of arc for angles.

The modeling of the source is reported in [11]. The AUT is plugged to a Spectrum Analyzer (SA), which takes power measurements that are triggered by the UAV's GPS. Therefore, during post-processing the UAV's position can be correlated with the AUT's received power readings. The antenna patterns are then reconstructed from the Friis equation. This method boasts a maximum discrepancy of 1 decibel with simulations, on 2 different antenna single elements. More precisely, the co-polar E- and H-planes were reconstructed from rectilinear flights at a constant height above the antenna. Various measurements campaigns, at VHF/UHF, using this technique have been carried out and reported in [12], [13], [14], [15], [16], [17], and [18]. Other authors have proposed similar but less successful methods in [19] and [20]. These campaigns are summarized in table 1.1.

It can be seen, through the latest publications just set forth, that UAVs show a good potential for measuring the gain and radiation pattern of antennas in situ, while it is also worth noting that no serious attention has been brought to the cross-polar radiation pattern of antennas. However, all the work that has been shown deals with frequencies ranging from HF to the bottom end of UHF, and with antennas pointing at zenith. This means several things:

- The ground reflections are not highly detrimental to the antenna performance at angles close to zenith.
- Lower frequency involves lower directivity, which means that antennas have gently-varying patterns easier to measure, in terms of positioning accuracy for the UAV.

Table 1.1: Reported past in situ antenna characterization measurement campaigns using UAVs

Freq. (MHz)	Probe	AUT	UAV	Scanning mode	Reference	Year
50	Dipole	Vivaldi	Hexacopter	Rectilinear Flight	[13]	2016
150	Dipole	Biconical	Hexacopter	Rectilinear Flight	[10]	2014
250	Dipole	Vivaldi	Hexacopter	Hover (Gain Measurement)	[12]	2016
250	Dipole	Log-Periodic	Hexacopter	Rectilinear Flight	[14]	2015
328.5	Monopole	Dish	Octocopter	Circular Flight	[20]	2015
350	Dipole	Vivaldi	Hexacopter	Hover (Gain Measurement)	[12]	2016
350	Dipole	Log-Periodic	Hexacopter	Rectilinear Flight	[14],[15],[18]	2015, 2016, 2015
408	Dipole	Log-Periodic	Hexacopter	Rectilinear Flight	[10], [16]	2014, 2014
408	Dipole	Vivaldi	Hexacopter	Rectilinear Flight	[17]	2014
433	Monopole	Log-Periodic	Fixed-wings	Circular Flight	[19]	2014
450	Dipole	Vivaldi	Hexacopter	Hover (Gain Measurement)	[12]	2016
650	Dipole	Log-Periodic	Hexacopter	Rectilinear Flight	[18]	2015

- Lower frequency, thus larger wavelength, also signifies that the antenna pattern of the probe mounted of the UAV will be less affected if the structure is small in terms of operating wavelength.

- The path loss and the different atmospheric/weather losses are smaller at a lower frequency, which is less stringent on transmitted power and receiving sensitivity requirements.
- The FF distance for single element antennas is very low, which means that the UAV can readily measure antenna pattern cuts, and that the power requirements are easily met.

Factoring in all these considerations will render the task of in situ antenna characterization with UAV more challenging. This is part of what this thesis is concerned with.

### **1.3 Proposed System**

The system presented in [10] is a perfect reference for the purpose of this thesis. The proposed system is depicted in figure 1.1. A few aspects are different compared to that of [10]. First of all, thanks to the recent improvement in GPS systems, Real Time Kinematics (RTK) GPS systems are now available and allow for centimeter positioning accuracy. This will be presented in detail in chapter 3. Therefore the motorized total station will not be necessitated. Moreover, concerning the synchronization of measurements, computer and GPS timestamps are related which means that, during post processing, the computer logging the data will provide timestamps that can be correlated to the timestamp of the UAV's GPS, and therefore its position. Furthermore the UAV will carry a probe which is an antenna array. The antenna array offers the possibility of having several antenna patterns, according to

the number of elements. This gives the possibility of having more directive antenna patterns on the probe, to mitigate the effect of the UAV structure. This will also be discussed in detail in chapter 3. Finally, the UAV can either fly around the AUT, a), or if the AUT can rotate in azimuth or elevation like some radar systems, the UAV can hover, b).

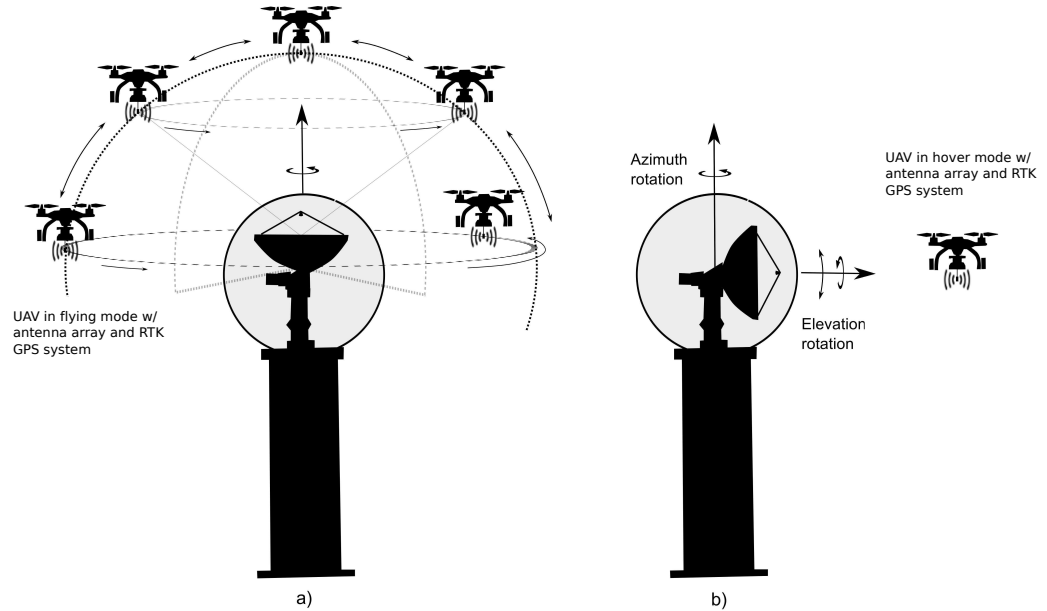


Figure 1.1: Illustration of the proposed system for in situ antenna characterization. a) The UAV flies around the radar system/antenna to carry out measurements. b) The drone hovers while the radar system/antenna rotates to carry out measurements.

## 1.4 Organization of the Thesis

The content of this thesis will follow a progressive approach. First of all chapter 2 will present the kind of systems that are the most relevant for in situ antenna characterization with UAVs at the ARRC. The requirement of these systems will be presented, which will give information about what to expect when measuring these

antennas. The later part of this chapter will then deal with general considerations about antenna measurements, regardless whether they are carried out with a UAV or not. This includes phase, amplitude, ground reflections, and link budget requirements. Then, Chapter 3 will focus more on the aspects of the measurements which pertain to the UAV. Scan types will be presented, as well as ground reflections in a more detailed manner, positioning accuracy of the UAV and the gimbal, and finally the effect of the UAV structure on the probe's antenna patterns. Chapter 4 will present and classify UAVs, show how they work, what components they comprise and what each of their roles is, and how to choose all the components to build a UAV. Finally, Chapter 5 will present the preliminary results of a proof of concept of this system, that the author has already published, in [21].

## Chapter 2

### System Requirements

This chapter will present a brief summary of frequency bands and some of their applications for antennas and radar systems. It will then zero in on the more relevant cases of weather and airport radars, within the framework of the ARRC, and on 5<sup>th</sup> generation wireless systems (5G) because of their widespread apparition in the near future. Particularly, the main figures of merit for these systems will be presented. Following this presentation, this chapter will focus on general requirements for measuring antenna or radar systems, regardless of whether UAVs are used. Amplitude, phase, ground reflection, and link budget requirements will be studied.

#### 2.1 Antenna Requirements

##### 2.1.1 Frequency Bands and Applications

There is a wide variety of systems located outdoors that use antennas, and to which UAV-based in situ antenna characterization could therefore apply. A good way to list these systems is to look at the different RF frequency bands and their associated applications. Studying all of these applications and the types of antennas they need is beyond the scope of this thesis. However, a brief overview shall be presented in this section, inspired by [22], [23] before zeroing in on the most relevant applications

with respect to the system presented in this thesis, and the ARRC. Frequency bands range from HF, as low as 3 MHz, to millimeter (mm), as high as 300 GHz.

A few concepts about radar systems will be presented first, as they are crucial to understand what follows. Radar performance can be characterized by various figures of merit, but the focus should be directed toward range, range resolution and angular resolution, which will be used repeatedly in this section, and will also give some insight for the antenna requirements of a particular system. The range of a radar is the maximum distance, from the radar, at which a target can be detected. The radar range equation describes this figure of merit, and exists in numerous forms, more or less complicated, and encompassing more or less factors and variables. One form is:

$$R = \left( \frac{P_t \tau_t G_t G_r \sigma c^2}{(4\pi)^3 k T_n D_s L f^2} \right)^{\frac{1}{4}}, \quad (2.1)$$

where  $P_t$  is the transmitted peak power,  $\tau_t$  is the transmitter pulse width,  $G_t$  is the gain of the transmitting antenna,  $G_r$  is the gain of the receiving antenna,  $\sigma$  is the scatterer cross section,  $c$  is the speed of light,  $f$  is the operating frequency,  $k$  is Boltzmann's constant,  $T_n$  is the effective noise temperature of the receiver,  $D_s$  is the signal-to-noise ratio to detect the echo, and  $L$  represents all the losses.

From this equation, there are some obvious observations such as the fact that with more transmitted power, higher gain antennas, and a target with a bigger cross section, the range of the radar will increase. A wider pulse means that more energy is transmitted, thus the range will also grow. As far as the detrimental factors to

the range are concerned, there are a higher noise temperature—which means more noise—, a desired higher signal-to-noise ratio, more losses, and a higher frequency. The latter aspect comes from antenna theory. Indeed, the directivity (proportional to the gain) of an antenna is given by:

$$D = A \frac{4\pi}{\lambda^2}, \quad (2.2)$$

where  $A$  is its aperture, and  $\lambda$  is the operating wavelength.

It is therefore evident that, for a given aperture, the gain grows as the frequency increases—or the wavelength decreases. This means that if the antenna size does not change for a radar, the radar range equation asserts that the range will increase as the frequency goes up. However, it should be kept in mind that losses increase greatly as frequency goes up, which then counterbalances the range gain.

The next figure of merit is range resolution, which is the minimum distance, along the same direction, between two identical targets that can be discriminated by the radar. For a radar with a rectangular pulse, the range resolution  $S_r$  is simply:

$$S_r = \frac{c \tau_t}{2}. \quad (2.3)$$

It can easily be seen that the pulse width, which represents the physical length of the traveling train of waves, dictates the range resolution. In other words, the wider the bandwidth—the narrower the pulse width, the finer the range resolution. For

systems using pulse compression, where pulses are modulated and more complicated than mere square shapes, the same rule holds if the notion of bandwidth is used.

Finally, the angular resolution of a radar is, for a given distance away from the radar, the minimum distance between two identical targets that can be discriminated by the radar. Typically, the angular resolution is determined in azimuth and elevation, as they are the two main angles used in the radar coordinate system. For both azimuth and elevation, the angular resolution can be expressed as:

$$S_a = 2R \sin \frac{\theta_3}{2} \quad (2.4)$$

where  $S_a$  is the angular resolution,  $R$  is the distance between the target and the radar, and  $\theta_3$  is the half-power beamwidth of the antenna along the azimuth or elevation dimension.

It is evident that the closer the distance between the radar and the target, and the narrower the antenna beamwidth, the finer the angular resolution.

The two lowest radar frequency bands are HF and VHF, which respectively range from 3 to 30 MHz, and 30 to 300 MHz. They are characterized by long wavelengths, from 1 to 100 m, which means that the antenna physical size needs to be very large for obtaining directive antennas and high resolution. The bandwidth is really narrow at these frequencies, which also impacts negatively the resolution. Most targets are in the Rayleigh regime, because they are much smaller than a wavelength, with low cross sections which makes them harder to be detected. Concerning the advantages of these frequency bands, the attenuation in the atmosphere is low, yielding

a longer range, and the electromagnetic waves refract in the atmosphere at these frequencies, yielding even longer ranges. Design of cheaper high-power and stable backend technology is easier than at higher frequencies. Applications of radars and antennas at these frequencies include aircraft detection during World War II, Over the Horizon (OTH) radars, astronomical observations, radio and television broadcasting, and very long-range marine and military communication—several hundreds of miles—, like the Russian P-18 or the American CXAM for example.

The frequency bands that follow are UHF and L-Band, which range from 300 to 1000 MHz and from 1 to 2 GHz respectively, corresponding to sub-meter wavelengths. These frequency bands are the main choice of long-range air-surveillance radars, due to low atmospheric attenuation. Moreover, antennas of realizable large sizes, as well as high power transmitters, make it possible to obtain a long range and a decent resolution to detect aircrafts far away. UHF, like VHF hosts applications such as radio and television broadcasting, both civilian and military marine, costal and airborne communication systems, Airborne Early Warning (AEW), and extraterrestrial detection such as missiles. L-Band is also used for AEW and extraterrestrial detection, like Federal Aviation Administration's (FAA) Air Route Surveillance Radars (ARSR-4) for instance, and air traffic control.

S-Band follows and ranges from 2 to 4 GHz. From this frequency range and up, narrow beamwidths, and therefore good resolutions, are no longer a challenge. With atmospheric attenuation still low but potentially significant when in presence of precipitation, S-Band radars cannot achieve long-range detection like at the lower

bands. However, it is the chosen frequency band for the national weather radar network, the Weather Surveillance Radar-1988 Doppler (WSR-88D) radar, to observe weather phenomena. Surveillance radars also exist but are mid-range, and are found in airports, like the Airport Surveillance Radars (ASR-9/11), and military bases.

Following is C-Band, ranging from 4 to 8 GHz. This frequency band is a good compromise between S-Band and X-Band, for characteristics such as range (because of atmospheric attenuation), size, and hence portability, as well as resolution. An example of radar operating within this frequency band is the portable TRML radar, that represents perfectly the applications of this frequency band: small to medium range detection of small and fast missiles or aircrafts. European weather radars also function at this frequency, as well as satellite communication systems.

Then comes X-Band that ranges from 8 to 12.5 GHz. This frequency range enables small and lightweight systems to be made, that can be handheld, such as the police speed radars, to determine how fast vehicles are going. Even though atmospheric conditions can be debilitating to radars operating at X-Band, particularly to the range, it is a great frequency range for portable and high resolution systems. Therefore, X-Band is the host of numerous radar systems: mobile weather radars at the ARRC such as AIR, RaXPol, and PX-1000—[2], [3], [4]—, and short to mid-range surveillance radars such as the BOR-A radar, that is used for ground, sea and low-level air surveillance at a few dozens of miles at most.

$K_u$ , K, and  $K_a$ -Bands respectively range from 12 to 18 GHz, 18 to 27 GHz, and 27 to 40 GHz. At these frequencies, even though resolution and data rate are high, and system sizes are small, there are some debilitating aspects. Indeed, the

RF backend technology is not as easy or cheap to conceive, it is difficult to achieve higher transmitted powers, and the range is low because it is significantly affected by atmospheric attenuation, and potentially by water absorption at frequencies around 22.5 GHz—the resonance frequency of water molecules. However some applications thrive at this frequency, in particular the Surface Movement Radars (SMR), that enable airports to detect aircrafts on their surface with high accuracy and renewing rates. Mobile wireless internet applications are also starting to make use of these frequency bands, as will be discussed in section 2.1.3.

Beyond K<sub>a</sub>-Band, the frequencies are denoted as millimeter wavelengths. Atmospheric attenuation and absorption at these frequencies becomes so detrimental, that a range of only a few meters may be achievable, on top of the fact that it is harder to conceive RF technology to meet power and sensitivity requirements. Space applications are a possibility given that attenuation is inexistent. Cloud observation is another application at these frequencies, as well as collision avoidance radars.

## **2.1.2 Weather and Surveillance Radars**

Weather and surveillance radars, more precisely aircraft surveillance radars, encompass four radars:

- The FAA's ASR-9/11 that detects and tracks aircrafts in the vicinity of airports, during departure or arrival, and that operates in S-Band. They are also found in military bases.
- The FAA's Terminal Doppler Weather Radar (TDWR), for detecting wind shears during the same phases, operating in C-Band.

- The National Weather Service's (NWS) WSR-88D, with polarimetric capabilities to measure weather phenomena such as tornadoes, storms, precipitation, etc. These radars operate in S-Band.
- The ARSR-4 for long range aircraft surveillance, and secondarily weather measurements, which serve both Homeland Security and Air Force functions.

These radars are mainly deployed on coasts and islands and operate in L-Band.

There are 629 radars altogether that perform these functions in the USA, respectively 306, 45, 156, and 122. As a side note, these radars are the object of a National Severe Storms Laboratory (NSSL) project to group them into one single multi-purpose radar: Multi-function Phased Array Radar (MPAR).

Table 2.1: Weather and surveillance radar antenna requirements

Parameters	TDWR	ASR-9/11	ARSR-4	WSR-88D
Frequency (GHz)	5.5 to 5.65	2.7 to 2.9	1.2 to 1.4	2.7 to 3.0
Peak Power (MW)	0.250	1.1	6.4	0.475
2-way beamwidth ( $^{\circ}$ )	0.55	1.4 ( $\phi$ ) 5 ( $\theta$ )	1.4 ( $\phi$ ) 2 ( $\theta$ )	0.93 $\lambda = 11cm$ 0.85 $\lambda = 10cm$ 45.36
Gain (dBi)	50	34	35 (Tx) 40 (Rx)	$\lambda = 11cm$ 46.32 $\lambda = 10cm$
Polarization	Linear (H)	Circular Linear (V)	Circular Linear (V)	Dual Linear (H and V)
On-axis cross polarization	NA	NA	> 17	> 45
2-way sidelobe levels (dB)	< -54; 1 <sup>st</sup> < -80; $\theta > 5$	< -48	< -60 for $\theta$ < -70 for $\phi$	< -64; 1 <sup>st</sup> < -100; $\theta > 10$

Within the MPAR framework, it is important to determine the requirements of every single radar system, to derive one single set of requirements for MPAR. This has been done in numerous publications and reports, [24], [25], [26], [27]. From [24] and [25] in particular, the requirements pertaining to the antennas of each system specifically have been extracted, and are reported in table 2.1.

Note that 2-way beamwidth and sidelobe level means that the values are considered on transmit and receive as a whole. The 2-way beamwidth is different than the actual antenna beamwidth because of dwell time and the fact that the antenna rotates. Similarly, the 2-way sidelobe level is the addition of the sidelobe level on transmit and receive.

### **2.1.3 Communication Systems**

Communication systems encompass subsystems such as television, radio, and cell phones. These are widespread and comprise numerous transmitting stations. Internet Mobile Technologies (IMT) are evolving fast to meet the demands of growing traffic and data rate, with the fifth generation (5G) to make its first commercial appearance in a few big US cities this year, before going global within 2020. 5G systems will use frequencies above 6 GHz, particularly millimeter wave (mmWave) frequencies, because the newly allocated bandwidths at these frequencies will allow the users to benefit from data rates of the order of Gbps (Gigabits per second). This new generation of systems has brought about more stringent requirements on the antennas, as will be explored and explained in the subsequent paragraphs of this section.

A transmitting station, or base station, will have a certain area coverage depending on several factors. The main ones comprise the environment (e.g urban and dense, clear and flat, mountainous), the propagation losses (highly dependent upon frequency), the transmitted power, the receiving sensitivity, and the transmitting and receiving antenna gains. One of the main challenges of operating at mmWave frequencies is the propagation losses, over which one has no control. According to the International Telecommunication Union's (ITU) 2015 report [28], path losses increase by 22.9 dB between 2 and 28 GHz, and by 30.9 dB between 2 and 70 GHz. Gas attenuation is not a contributing factor for the aimed coverage radius of 200 m, while heavy rain attenuation is less than 2 dB at 60 GHz. Propagation losses at these frequencies are also extensively studied in [29] and [30]. These losses will need to be counterbalanced to get the desired coverage. Since increasing transmitted power is financially unattractive and that the receiving antenna characteristics have reached their limits because of the form factor, the transmitting antenna gain remains the only variable that can compensate for these losses.

Considering the propagation losses just evoked, as well as the base station coverage radius of 200 m, it turns out that having an Equivalent Isotropic Radiated Power (EIRP) of 50 to 65 dB along the main beam, coupled with a standard receiving antenna with a gain of around 15 dBi, will fulfill this requirement, [28], [31]. The EIRP is merely the sum between the antenna gain and the transmitted power, in dB. Given that the transmitted power is about 20 dBW, [28], [31], this means that the transmitting antenna gain has to be in the range of around 20 to 35 dBi. This is obviously not achievable by single elements, so phased array antennas will

have to be used. The array size will depend on the desired total gain and the single element gain, but even for large arrays comprising dozens or hundreds of elements, the size will remain small due to the high frequency. A thorough review of existing candidate antennas is presented in [32]. Finally, there are two techniques to get the desired coverage in azimuth, as outlined in [28] and [33]. One is to have fixed-beam phased array antennas that are arranged in panels of approximately 8 arrays, with one panel per  $60^\circ$  sector. The other solution is to have one single array per sector that has beam-steering capabilities.

In summary, the performance requirements for the 5G base station antennas can be summed up by the gain requirement of around 20 to 35 dBi. No particular requirements are placed upon the antenna pattern, the sidelobe level, or the cross polarization.

## 2.2 Measurement Requirements

Now that the systems of interest have been presented, alongside their antenna requirements, we shall focus on how to measure their performances. Measuring the main features of an antenna is accomplished by measuring its radiation pattern. This is further divided into two vastly different categories: Near Field (NF) and FF, where NF corresponds to a distance between the probe and the AUT that is of the order of a few wavelengths and where the radiated power is mostly reactive, and FF corresponds to the distances farther than NF where the ratio of the radiated wave's in-phase electric field  $E$  and magnetic field  $H$  is equal to  $Z_0$ , the free space

impedance, approximately equal to  $377 \Omega$ . It also corresponds to a certain phase criterion as will be discussed shortly. Measurement techniques vary widely between NF and FF. Moreover, it is the FF radiation pattern that is of interest. Therefore, only FF measurements will be dealt with in the following paragraphs. Nevertheless it is possible to calculate the FF radiation pattern from NF measurements, using spatial Fourier analysis, [34].

The knowledge of an antenna radiation pattern also yields the beamwidth, the different sidelobe levels, and the cross polarization level. Since measuring the full three-dimensional radiation pattern is a lengthy and tedious task, and its knowledge is not necessary, it is generally measured in three principal planes: the E-Plane, where the electric field lies, the H-Plane, orthogonal to the E-Plane, and the D-Plane—less common—, in between the latter two. When using standard techniques, namely antenna ranges, measuring the antenna patterns is most commonly accomplished by illuminating the AUT with a probe, and rotating it in azimuth or elevation for different elevation or azimuth orientations respectively. This is accomplished by the use of Elevation-over-Azimuth or Azimuth-over-Elevation positioners. Each rotation over a range of azimuth or elevation angles, for a fixed elevation or azimuth angle respectively, will give an antenna pattern cut. In this section the most important factors pertaining to antenna measurements will be discussed, and their influence will be illustrated. When discussing each of these factors, it will be assumed that proper alignment is established between the probe and the AUT.

### 2.2.1 Phase

The most important rules to carry out such measurements will be set forth in the upcoming paragraphs. They are succinctly described in [35], but will be thoroughly described and illustrated here. The first rule is concerned with the FF distance and its implications. One of these has already been mentioned briefly, in the FF the radiated power on an antenna is real. Indeed, the electric field radiated by an antenna comprises a real term—responsible for the active power— inversely proportional to the distance, and imaginary terms—responsible for the reactive power— inversely proportional to the power squared, cubed, etc. In the FF only the first term is predominant, and is therefore of interest. The other implication is more subtle, it is the phase distribution over the AUT's aperture. Since an antenna, and therefore the illuminating probe, radiates spherical waves, the phase of the probe's illuminating wavefront over the AUT's aperture will not be uniform. This affects the field distribution over the aperture, and consequently the antenna pattern. Ideally, we wish that the AUT would be excited by a plane wave to avoid this problem, but this is an ideal case that is not realizable in practice. Obviously as the distance between the AUT and the probe increases, the exciting wavefront will be planer, and the phase over the AUT's aperture more uniform. But what should be the minimum distance to obtain reliable measurements ?

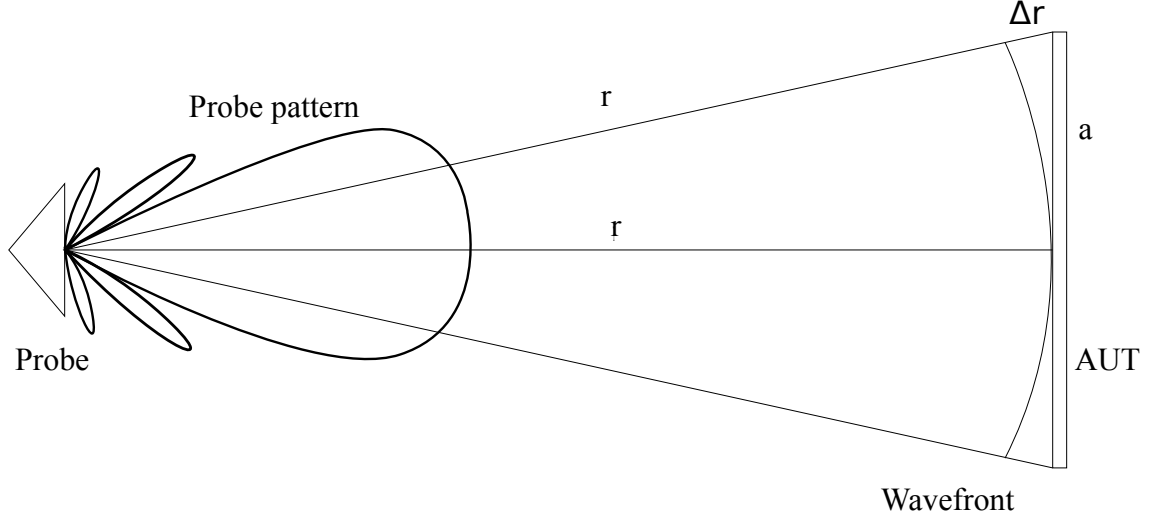


Figure 2.1: Illustration of the FF measurement configuration.

In figure 2.1, we can see that the distance between the probe and the center of the aperture is equal to  $r$ . But this distance is not  $r$  over the whole aperture, it varies to reach a maximum at its edge, which is equal to  $r + \Delta r$ . In the right triangle formed by these two segments and half of the aperture, we can write that  $r^2 + \frac{a^2}{4} = (r + \Delta r)^2$ . Neglecting  $\Delta r^2$ , we arrive at  $\Delta r = \frac{a^2}{8r}$ . This path length difference is what gives a phase difference over the aperture. It is widely accepted that the latter should not exceed  $\frac{\pi}{8}$ , or  $\frac{\lambda}{16}$ , as to keep the measurement errors down without growing the distance to impractical extents. This translates to  $\Delta r \leq \frac{\lambda}{16}$ , which means that:

$$r \geq \frac{2a^2}{\lambda}. \quad (2.5)$$

This FF criterion is widely accepted and used for antenna measurements. If more precision is wanted on the measurements, in the case of very low sidelobe levels for

instance, it is easy to generalize the FF criterion for an arbitrary phase error  $\Delta\phi$ .

It can be simply expressed as:

$$r \geq \frac{\pi a^2}{4\lambda\Delta\phi}. \quad (2.6)$$

It is now interesting to illustrate this FF distance with respect to frequency, for a given antenna, and for different phase requirements. This is done in figure 2.2 where the FF distance is plotted for S-Band rectangular uniform aperture antennas with beamwidths of 2, 10 and 100°, for phase error requirements of 5.625, 11.25, and 22.5°. It can be seen that the FF distance decreases rapidly with frequency, and that it increases dramatically if stringent phase requirements are imposed.

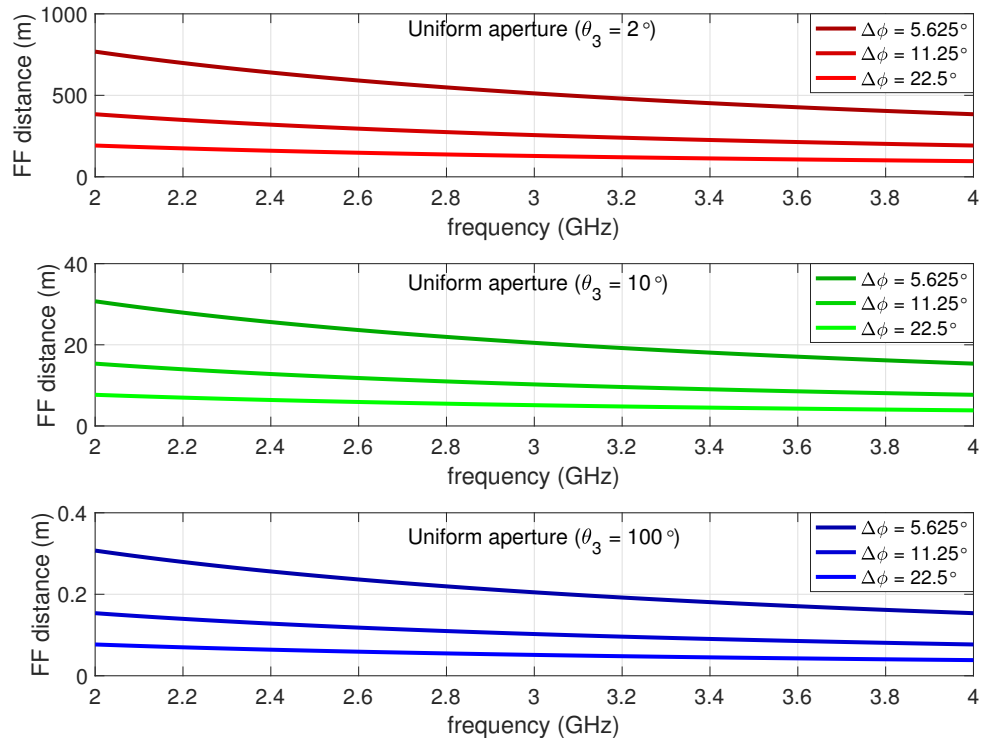


Figure 2.2: FF distance versus frequency for 3 given uniform square aperture antennas ( $\theta_3 = 2, 10$  and  $100^\circ$ ), and for 3 different phase error requirements ( $\Delta\phi = 5.625, 11.25$  and  $22.5^\circ$ ).

It is also interesting to see the effect of this phase error on the antenna patterns. It becomes pronounced on highly-directive antennas with low sidelobe levels. This point is illustrated by figures 2.3 and 2.4. Figure 2.3 shows the phase taper that an aperture experiences for phase errors of 5.625, 11.25, and 22.5°. It is a quadratic function of the aperture position as demonstrated by equation 2.6, with no error in the middle of the aperture and the maximum error at the edges of the aperture. This phase taper effectively modifies the field distribution over the AUT's aperture, therefore changing the actual antenna pattern. Consider an aperture in the x-y plane where the field distribution can be written as  $A(x, y)e^{j\phi(x, y)}$ , the phase taper modifies this distribution to be  $A(x, y)e^{j(\phi(x, y) + \Delta\phi(x, y))}$ , which in terms modifies the antenna pattern and other characteristics. On figure 2.4, these 3 different tapers are applied for an  $40 \times 40 \lambda$  aperture with a Taylor distribution that yields a 40-dB sidelobe level. It can be observed that it is the first sidelobe that is affected, only 5.625° of phase error yields a good measurement of the first sidelobe.

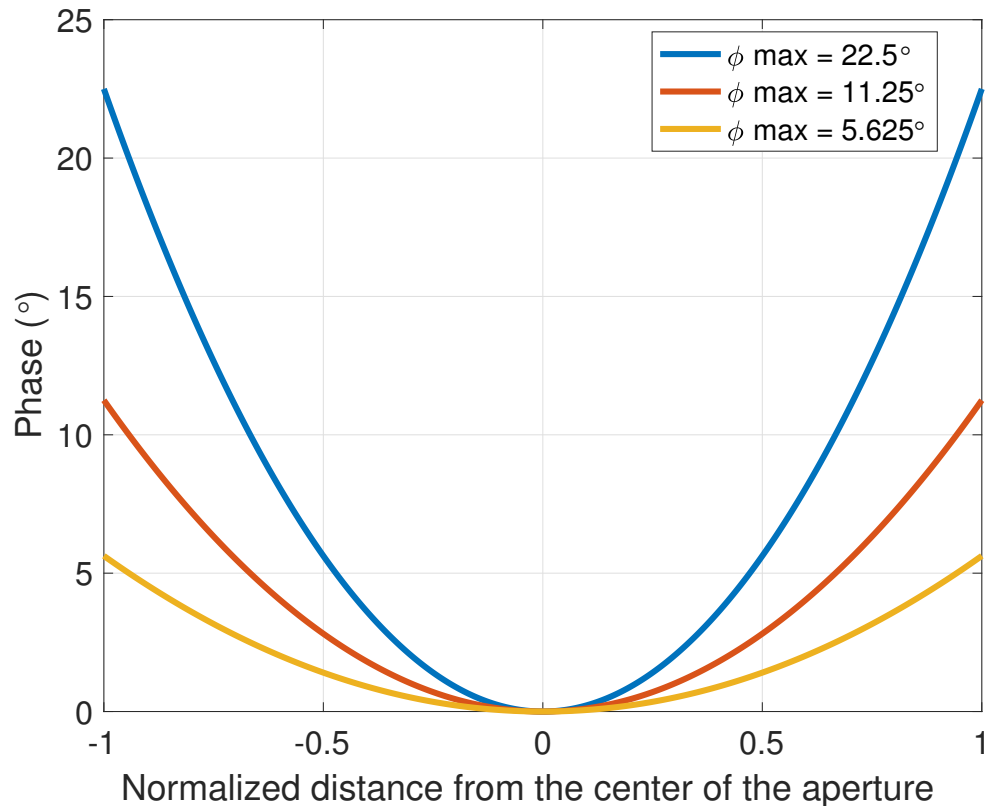


Figure 2.3: Aperture phase taper versus normalized aperture coordinates for a uniform square aperture, and 3 different FF phase error requirements ( $\Delta\phi = 5.625$ , 11.25 and  $22.5^\circ$ ).

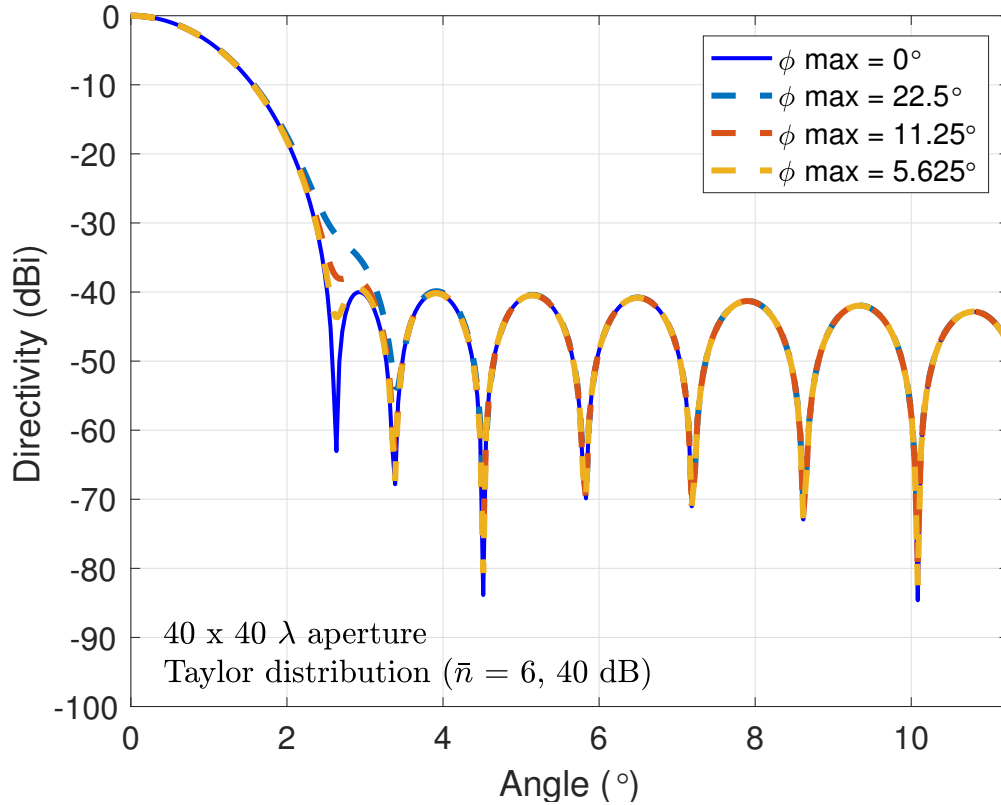


Figure 2.4: Effect of 3 different FF phase error requirements ( $\Delta\phi = 5.625, 11.25$  and  $22.5^\circ$ ) on the principal plane antenna pattern of a  $40 \times 40 \lambda$  uniform square aperture with a Taylor  $\bar{n} = 6, -40$  dB distribution.

## 2.2.2 Amplitude

We will now look at the effect of the amplitude of the illuminating wavefront on the measurements. Ideally, to prevent amplitude-related errors on the measurements, the wavefront that illuminates the AUT should be uniform in amplitude as to not modify the field distribution and therefore the antenna pattern, similarly to what has been shown for the phase. However, this is not the case in practice, as is shown on figure 2.5. We can see an angle subtended by the AUT's aperture from the probe, depending on the aperture size and the distance. This angle that we will call the

projected beamwidth determines what portion of the probe's antenna pattern will illuminate the AUT's aperture, and therefore what the amplitude taper over the aperture is. If the amplitude taper over the aperture is known, normalized to the maximum electric field amplitude over the aperture, and expressed as  $A_{tap}(x, y)$ , then the field distribution will be  $A_{tap}(x, y)A(x, y)e^{j(\phi(x, y) + \Delta\phi(x, y))}$ . The antenna pattern and other figures of merit will be modified.

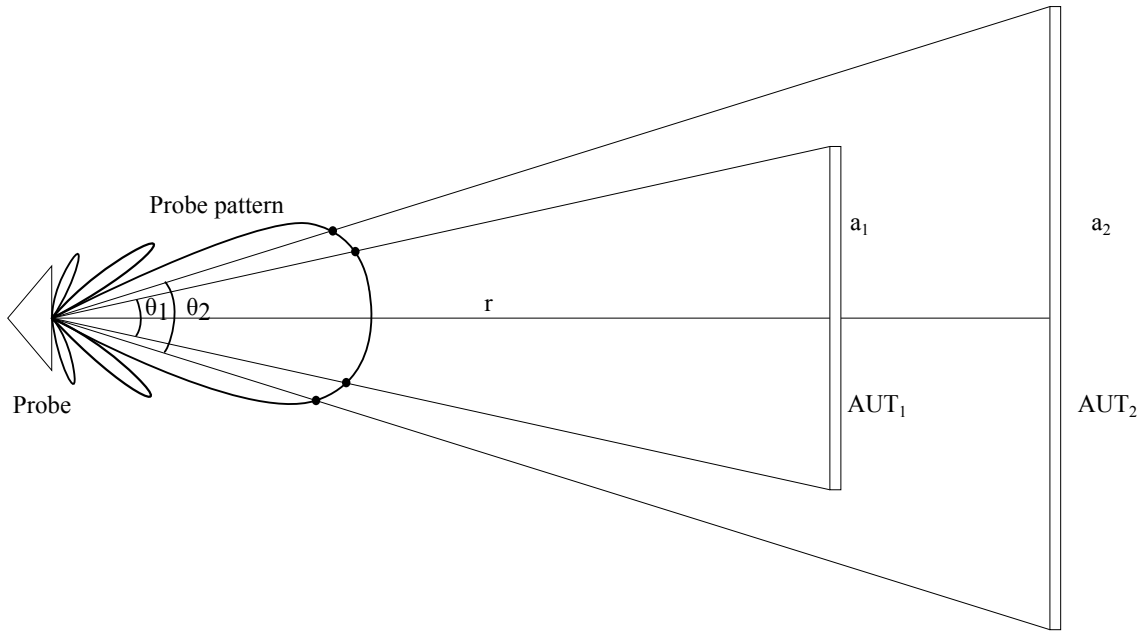


Figure 2.5: Illustration of the probe's antenna pattern projection onto the AUT's aperture.

This projected beamwidth, referring to figure 2.5, can be expressed as:

$$\theta_{pr} = 2 \arctan \frac{a}{2r} . \quad (2.7)$$

Note that if we replace  $r$  in equation 2.7 by its standard expression from equation 2.5, it follows that  $\theta_{pr} = 2 \arctan \frac{\lambda}{4a}$ , which means that the projected beamwidth

gets smaller with the aperture size for a given FF distance criterion. For a uniform square aperture the 3-dB beamwidth is expressed as  $\theta_3 = 50.6 \frac{\lambda}{a}$ , so we can also write  $\theta_{pr} = 2 \arctan \frac{\theta_3}{202.4}$ . Therefore the projected beamwidth will decrease as the AUT's aperture beamwidth decreases, for a given FF distance criterion. From equation 2.7 it is also true that the projected beamwidth gets smaller if the distance is increased, for a given aperture. Then, if the probe's antenna pattern is known in the range of the projected beamwidth, the amplitude taper on the AUT's aperture can be determined. A good compromise between the probe's directivity and the projected beamwidth—aperture size and FF distance—needs to be reached so that this taper does not affect the measurements adversely. Obviously, a single element antenna with very low directivity could give a quasi-uniform amplitude over the aperture, but other problems can arise with such a choice. Indeed, ground reflections can become detrimental to the measurements if they are too strong, and since the probe is mounted on a UAV, the structure of the UAV can potentially degrade the performance of the probe, which in terms could potentially yield poor quality measurements. These two points will be studied in later sections. This means that both directive and non directive antennas should be considered in this section. In figure 2.6, the projected beamwidth is shown versus the beamwidth of a uniform square aperture, for the standard FF criterion, in blue. In light of this paragraph's discussion, it can be seen that the projected beamwidth becomes very high for large beamwidths. It should be kept in mind, however, that for large beamwidths the FF distances are so small that the distance can be increased substantially to decrease the projected beamwidth. In red, the probe's normalized electric field at the

beamwidth’s corresponding aperture edge is shown for a regular microstrip patch antenna [34]—solid—as a probe, and for a 3x3 uniform square array with a half-wavelength separation—dashed—as a probe, both for the E-Plane which is the most directive. As said previously, the array is seen to apply a steeper amplitude taper.

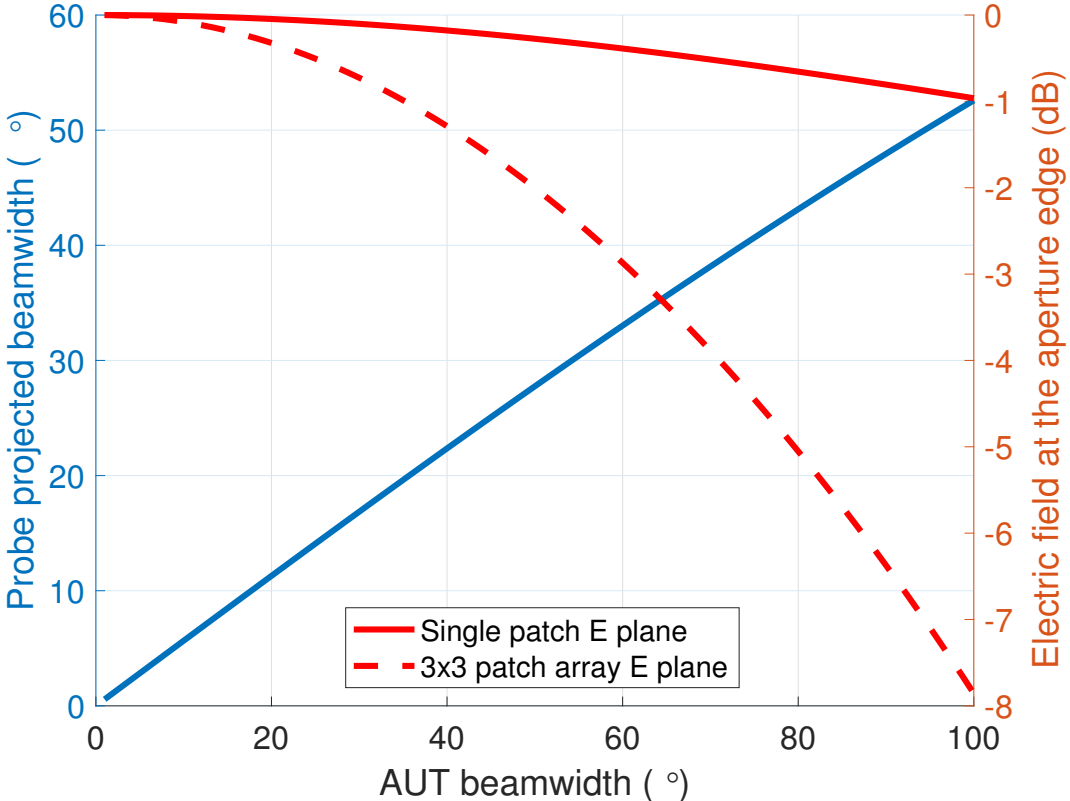


Figure 2.6: Projected beamwidth onto a uniform square aperture and electric field of a single patch antenna and a 3x3 uniform array of patch antennas ( $\frac{\lambda}{2}$  spacing) at its edge, versus its beamwidth.

In the UAV-based characterization system, the measurement distance will be of the order of several meters at the minimum, even for non directive antennas. Moreover, the payload size and weight limitation indicate that the array not be very directive, unless . With these facts in mind, the amplitude taper over the AUT’s aperture will not have any detrimental effect on the measurements. On figure 2.7, the minimum

distance criterion just evoked is applied, and is equal to 10 m. It can be observed that in this case, the maximum electric field at the aperture edge is a few tenths of dB, which corroborates the fact that it will have no influence on the measurements.

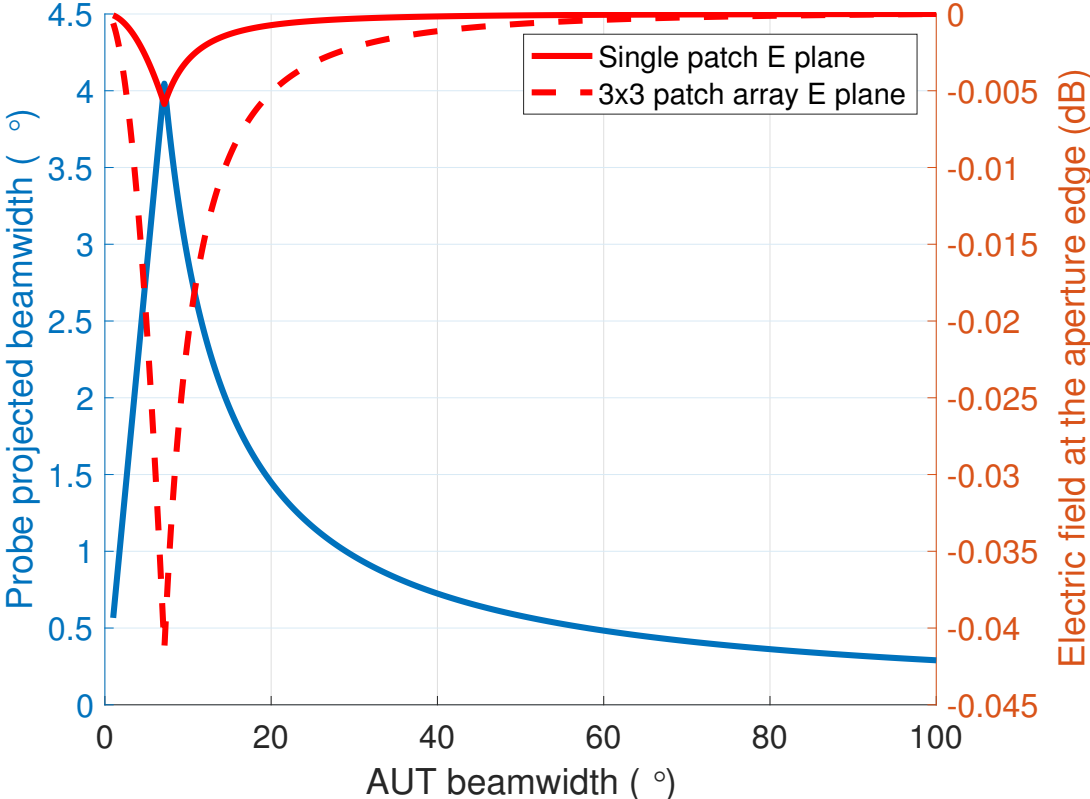


Figure 2.7: Projected beamwidth onto a uniform square aperture and electric field of a single patch antenna and a 3x3 uniform array of patch antennas ( $\frac{\lambda}{2}$  spacing) at its edge, versus its beamwidth. A minimum of 10 m for the FF distance was used.

### 2.2.3 Ground Reflections

Up until now, when considering a probe illuminating an AUT, only a single wave path has been taken into account, the direct and shortest path between both antennas. However, outdoors there are other rays that reflect off of different locations. While predicting a model that account for all these paths is a task far beyond the

scope of this thesis, it is possible to use a simple model that yields satisfactory insight and results. On figure 2.8, we see this propagation model that consists of the direct ray and of a ray that reflects off of the ground, obeying Snell’s law, that is  $\theta_i = \theta_r$ .

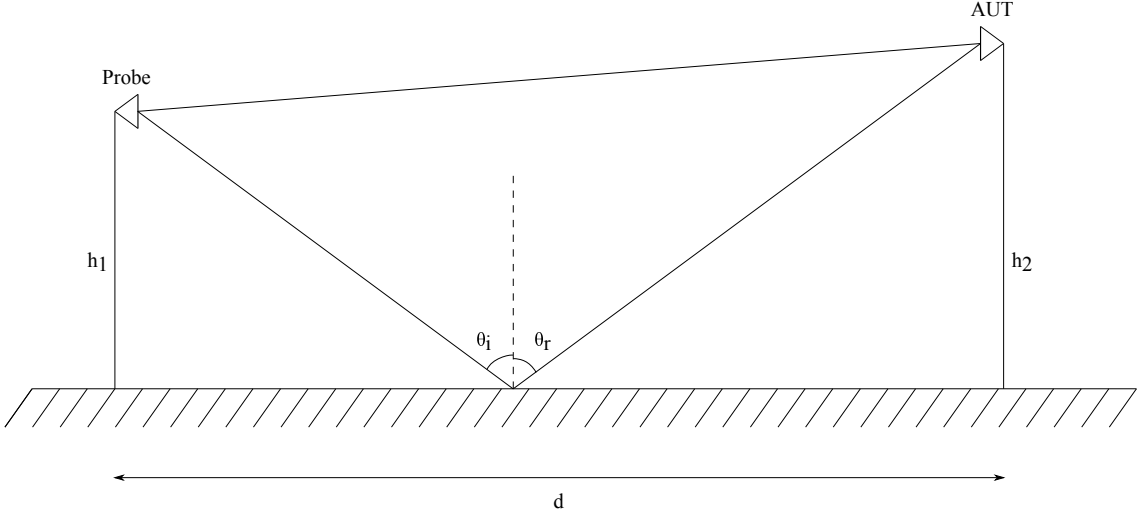


Figure 2.8: Propagation model between the probe and the AUT for FF measurements.

While the detailed analysis of ground reflections and their influence on the antenna pattern measurements will be carried out in a subsequent section, we shall study a simple case here to look at the effect of ground reflections. The path length of the direct ray can be expressed as  $\sqrt{d^2 + (h_2 - h_1)^2}$ , and that of the reflected ray as  $\sqrt{d^2 + (h_1 + h_2)^2}$ . Now if we use the Maclaurin series to simplify both expressions, we have respectively  $d + \frac{h_1 h_2}{d}$  and  $d - \frac{h_1 h_2}{d}$ . The path length difference can then be expressed as  $2\frac{h_1 h_2}{d}$ , which translates to a phase difference of  $2\frac{h_1 h_2}{d} \frac{2\pi}{\lambda}$ . Then, if we assume that the distance is very large—several hundred meters, which is the case for radars and directive antennas, or if the measurements are carried out far away—, it follows that:

- The ground may be considered as a perfect conductor, which gives +1 reflection coefficient for vertical electric fields and -1 for horizontal ones.
- The field radiated along both paths have the same magnitude.
- The path loss along both paths is the same.

These considerations enable us to write the field amplitude variation at the AUT.

Given an incident field of amplitude  $E$ , the field at the AUT is given by  $E(1 - e^{j2\frac{h_1 h_2}{d} \frac{2\pi}{\lambda}})$  for the horizontal case, and by  $E(1 + e^{j2\frac{h_1 h_2}{d} \frac{2\pi}{\lambda}})$  for the vertical case. This gives:

$$|E_h| = \left| 2E \sin \frac{h_1 h_2}{d} \frac{2\pi}{\lambda} \right| \quad (2.8)$$

for horizontal polarization;

$$|E_v| = \left| 2E \cos \frac{h_1 h_2}{d} \frac{2\pi}{\lambda} \right| \quad (2.9)$$

for vertical polarization.

Equations 2.8 and 2.9 are important results telling us that the magnitude of the electric field at the AUT varies between 0 and twice the incident electric field magnitude, in a sinusoidal fashion. This means that the distance and the heights, generally the probe height only since the AUT might be fixed, have to be carefully chosen as to avoid 'blind' or very low-power regions. The illustration of these points is shown on figures 2.9 and 2.10.

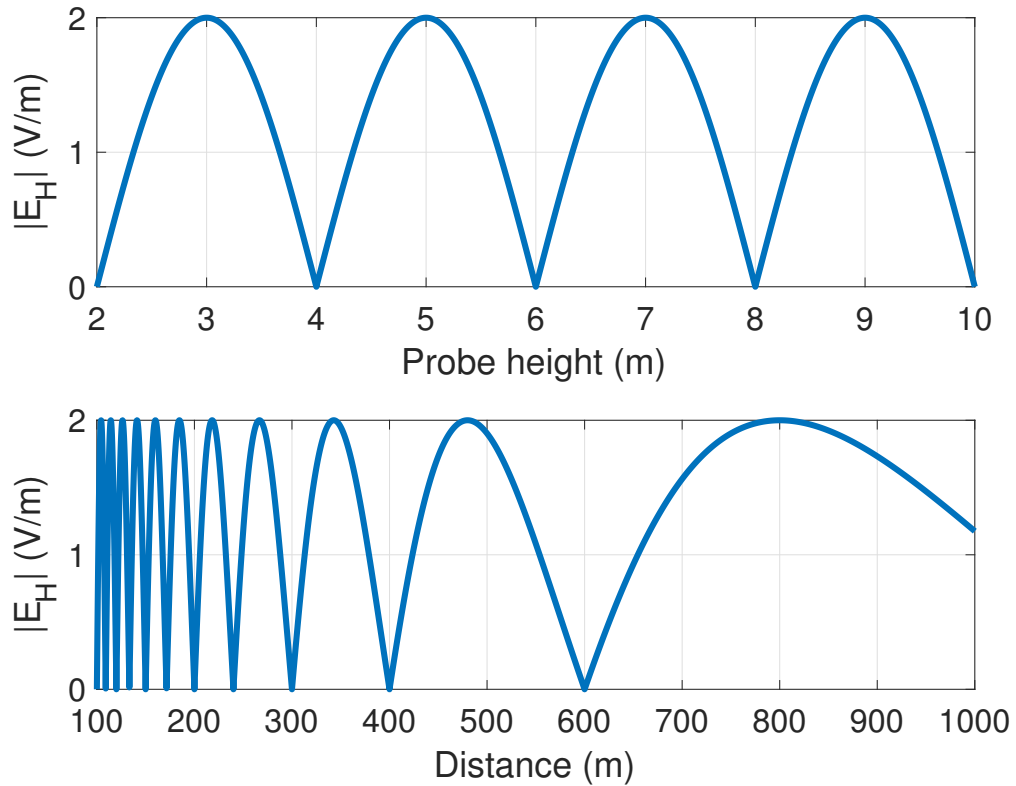


Figure 2.9: Normalized horizontal electric field magnitude at the AUT versus probe height (distance of 400 m and AUT height of 10 m) and distance (probe height of 6 m and AUT height of 10 m), in the presence of ground reflections.

Assuming that the AUT has a fixed height as was just said, which is often the case outdoors, the electric field magnitude was plotted versus both probe height and distance. It can be seen that this is a normal absolute cosine function versus probe height, but not versus the distance since the period is inversely proportional to it. As a result, it spreads out as the distance increases. More specifically the distance was chosen to be 400 m when the probe height varies, and the probe height was chosen to be 6 m when the distance varies. In all cases the AUT is at a height of 10 m. In [35], the use of a diffraction fence is suggested to filter out the ground

reflections, if the user wishes to be freed from being tied to distance and height requirements.

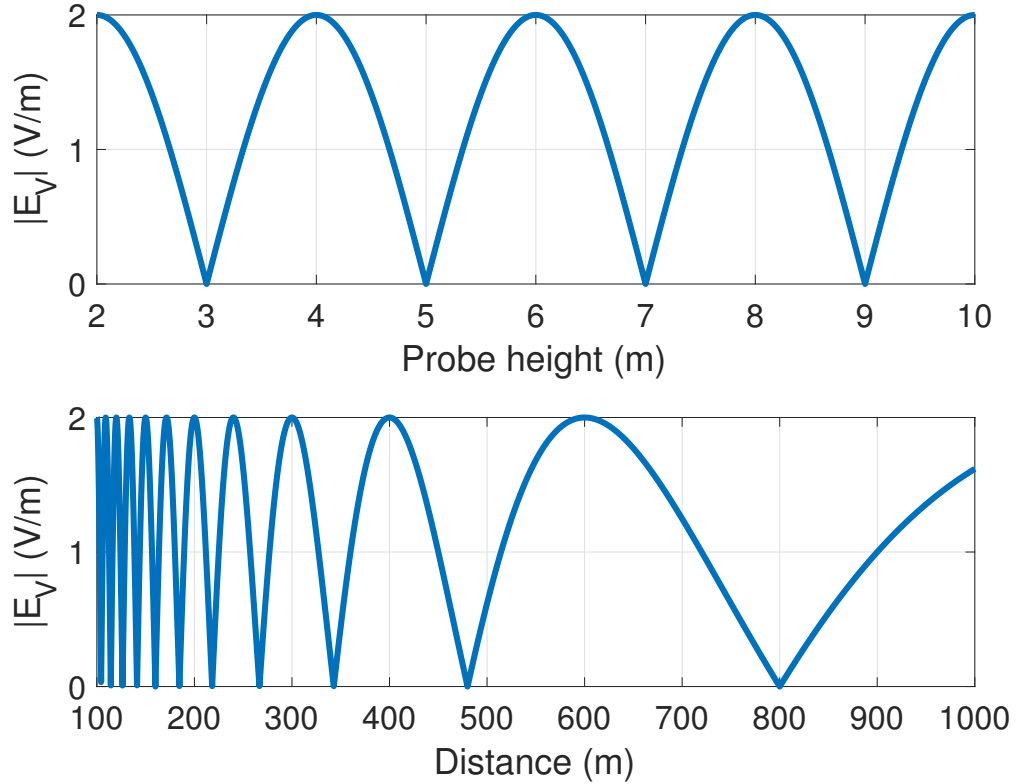


Figure 2.10: Normalized vertical electric field magnitude at the AUT versus probe height (distance of 400 m and AUT height of 10 m) and distance (probe height of 6 m and AUT height of 10 m), in the presence of ground reflections.

## 2.2.4 Link Budget

Lastly, some attention should be devoted to link budget when measuring two antennas. The Friis equation is an accurate model for this purpose:

$$P_r = P_t(1 - \Gamma_t)(1 - \Gamma_r)\left(\frac{\lambda}{4\pi R}\right)^2 G_t G_r |\rho_t \cdot \rho_r|^2, \quad (2.10)$$

where  $P$  is the power,  $\Gamma$  is the reflection coefficient,  $R$  the distance between antennas,  $G$  the antenna gain,  $\rho$  the polarization vector, and the subscript  $t$  and  $r$  stand for transmission and reception respectively. If we assume that the antennas are matched to their generators and that there is no polarization mismatch, then 2.10 reduces to:

$$P_r = P_t \left( \frac{\lambda}{4\pi R} \right)^2 G_t G_r. \quad (2.11)$$

In practice, a signal can be detected only if its power density is greater than that of noise. Therefore equation 2.11 can give some insight if we introduce  $P_n$ , the noise power level, and the Signal-to-Noise Ratio (SNR) defined as  $\frac{P_r}{P_n}$ . For more simplicity, we can also call  $\left( \frac{\lambda}{4\pi R} \right)^2 PL$ —Path Loss— and write in dBW:

$$SNR_{dBW} = P_{t_{dBW}} + PL_{dBW} + G_{t_{dB_i}} + G_{r_{dB_i}} - P_{n_{dBW}}. \quad (2.12)$$

If equation 2.12 is larger than the SNR threshold, then  $P_r$  is detected. It should be kept in mind that  $P_t$  is affected by the ground reflections and can be doubled or nullified, as described in section 2.2.3. A simple illustration of this point can be made with three antennas/radar systems that represent relevant cases:

- The S-Band WSR-88D.
- The X-Band RaXPol.
- A 28-GHz 5G base station 64×64 antenna array.

For both radars, parameters in chapter 2.1.2 as well as in [3] were used, for the frequency, antenna size, antenna gain, and maximum transmitted power. As for the 5G antenna and the information provided in 2.1.3 , a 64×64 array at 28 GHz

will be retained, with a gain of 30 dBi and a maximum transmitted power of 20 dBm by the base station. All these parameters are summed up in table 2.2. The FF distance was chosen to be  $8\frac{a^2}{\lambda}$  for the weather radars, which symbolizes precise sidelobe measurements. Concerning the 5G antenna, the FF distance is very small due to the high frequency, so the measurement distance was picked to be 100 m, which is within the coverage of a 5G base station. The probe on the UAV was chosen to be a  $3\times 3$  patch antenna array, with a gain of 12 dBi. Finally, the noise floor was picked to be -80 dBW. The SNR was plotted versus the AUT gain. More precisely a gain range of 60 dB from the maximum gain for the weather radars was chosen, while a gain range of 30 dB from the maximum gain of the 5G antenna was used. This represents low sidelobe level measurements. Figure 2.11 presents the results for all three antennas. It is seen that the SNR is sufficient to carry out the measurements in all cases for this setup. If amplifiers are used, their gain can be added to the right-hand side of equation 2.12. If other losses have to be included, they can be subtracted from the right-hand side of equation 2.12.

Table 2.2: Antenna and radar systems parameters for the link budget study

Parameters	WSR-88D	RaXPol	5G Antenna
Frequency (GHz)	3	9.73	28
Gain (dBi)	46.32	44.5	30
Antenna Size (m)	8.54	2.4	0.48
Peak power (dBW)	56.77	43.01	20.00

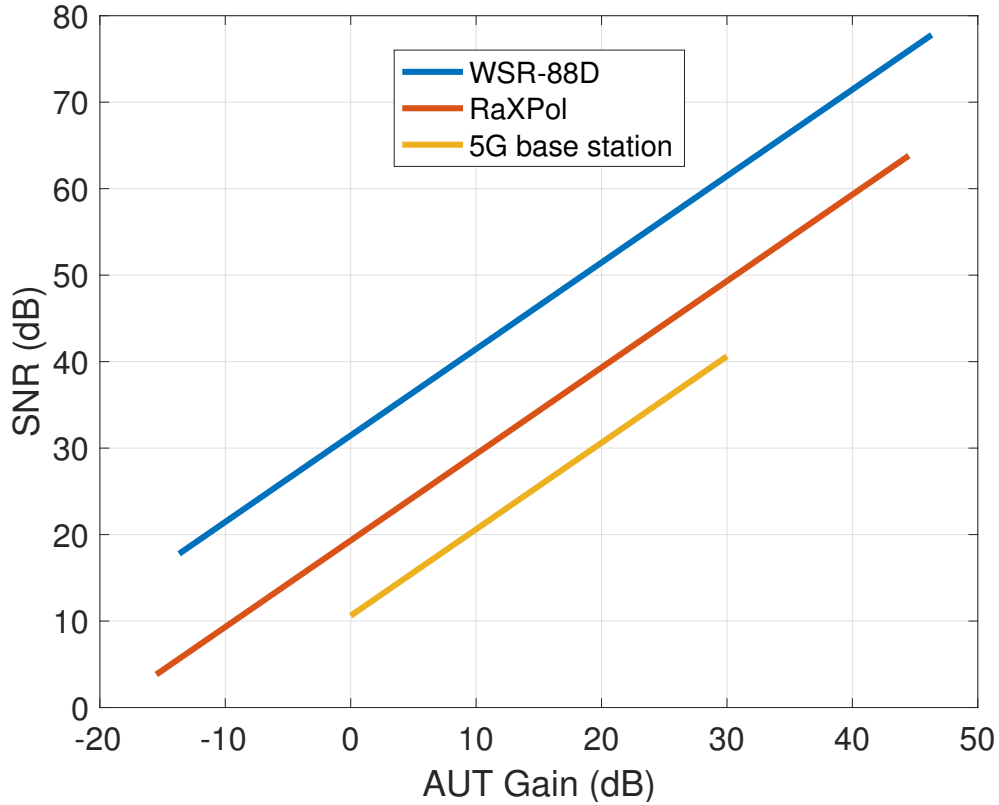


Figure 2.11: Link budget (SNR) for the WSR-88D versus its antenna gain—blue, RaXPoI versus its antenna gain—red, and 5G 30-dBi gain antenna versus its gain—yellow. Parameters for these antennas are summed up in table 2.2. The FF distances were chosen according to the  $8\frac{a^2}{\lambda}$  criterion for accurate sidelobe level measurements. Concerning the 5G antenna, a distance of 100 m was used, which is within the coverage of a 5G base station. A 12-dBi  $3\times 3$  patch antenna array was used, and the noise floor is -80 dBW.

## 2.3 Summary

Important system requirements for weather and airport surveillance radars, as well as 5G antennas, were presented in the first part of this chapter. These requirements set the measurement expectations for the system presented in this thesis. General measurement requirements were presented as well. It was discovered that for very

directive antennas, such as weather radars, the measurement distance–FF distance– has to be carefully chosen to be able to measure the first sidelobe accurately. This is because of the phase taper over the AUT aperture. It was seen that the amplitude taper over the AUT aperture has no effect on the measurements even if a  $3 \times 3$  patch antenna array is used as a probe. Then, it was shown that ground reflections can make the electric field at the AUT aperture vary between zero and twice the incident value, for large distances between the probe and the AUT. This is a very important result since it demonstrates that proper care needs to be brought to the distance between the probe and the AUT, as well as their heights relative to each other. Finally, link budget analysis was carried out for the WSR-88D, the RaXPoL, and a typical 5G base station antenna. It could be seen that measuring the antenna patterns is easily achievable in the FF, with a  $3 \times 3$  patch antenna array on the UAV.

## Chapter 3

### Design Considerations and Tradeoffs

This chapter presents the measurement aspects directly pertaining to the use of UAVs. Different scanning strategies will be presented first, with the emphasis on the necessary flight distance to measure a cut within a range of angles. Then, a more thorough study on ground reflections will be presented, whose effect will be studied for three cases: weather radar—WSR-88D and RaXPoI—and 5G base station antennas. The positioning accuracy of UAV platforms and their components will be studied. More specifically, standard and RTK GPS will be reviewed for the position accuracy of the UAV itself. IMUs will also be treated for the precision of the gimbal. The effect of the position errors on the measurements will also be formulated and illustrated. Finally, the focus will be shifted towards the effect of the UAV structure on the mounted probe. Several platforms will be studied, focusing on the in-house ARRC hexacopter platform with a  $3 \times 3$  single layer patch antenna array.

#### 3.1 Scan Types

For this UAV-based system it is important to determine the flight pattern of the UAV with respect to the AUT, which in terms dictates what part of the antenna pattern is measured. This is referred to as a mission. Of course there is a trivial

case where the UAV hovers in place and the AUT rotates, which is identical to the standard measurement techniques. For all other missions where the UAV does not hover, the most common options are illustrated in figure 3.1, according to the standard scanning techniques. Planar scans are the simplest to implement as merely rectilinear flights, which are easy references to generate and follow for a flight controller. For case (a) the scan is a grid in front of the antenna, in the  $x$ - $z$  plane, assuming the AUT points at the horizon along  $y$ . This respectively yields azimuth and elevation measurements, but not over the whole sphere. If the AUT is pointing at zenith, case (a) reduces to a grid in the  $x$ - $y$  plane. This is highly preferable to mitigate the influence of ground and environmental reflections. However, not all radar or antenna systems are capable of doing this. For instance, the WSR-88D is not capable of achieving such a feat, it is only able to scan at low-elevation angles. Case (b) represents another easy way to make elevation measurements at higher angles without flying at high altitudes, by flying in the  $x$ - $y$  plane above the AUT which points at low elevation angles or along the horizon. Cylindrical measurements consist either of equal-radius concentric circles centered around the antenna at different altitudes in the  $x$ - $y$  plane—azimuthal cuts at fixed elevation angles, or of planar scans along  $z$  at a distance equal to the radius of these circles—elevation cuts at fixed azimuth angles. Spherical measurements consist of concentric circles around the antenna at the same distance from the antenna either in the  $x$ - $y$  plane or in any plane orthogonal to it. In the latter case, it is worth pointing the AUT at zenith

because ground and environmental reflections will have less impact on the measurements. As far as the circular paths are concerned, flight controllers can achieve them by using enough waypoints and proper trajectory interpolation between them.

For each scan just presented, the necessary distance to measure a cut will be derived. If the flight speed is considered constant, this knowledge then yields the flight time needed to measure these various cuts. For planar scans, there are 3 different geometries corresponding to flights along 3 different axis. For scans along  $x$ , the measured cut is at  $\theta = \arctan \frac{r}{h}$  where  $r$  denotes the FF horizontal distance between the probe and the AUT (along  $y$ ), and  $h$  the height difference between them. It should be kept in mind that this angle is not constant across the trajectory of the scan because  $r$  changes, unless  $h = 0$ . The range of azimuth angles that is covered is  $R_\phi = 2 \arctan \frac{d_{pl_x}}{2r}$  where  $d_{pl_x}$  is the distance covered for the scan. Therefore the distance covered by the scan is expressed as:

$$d_{pl_x} = 2r \tan \frac{R_\phi}{2}. \quad (3.1)$$

As far as the planar scans along  $z$  are concerned, the measured cut is at  $\phi = \arctan \frac{r_x}{r}$  where  $r_x$  is the distance between the probe and the AUT along  $x$ . The range of elevation angles that is covered is  $R_\theta = \arctan \frac{d_{pl_z}}{\sqrt{r^2 + r_x^2}}$ . This is equivalent to a covered distance of:

$$d_{pl_z} = \sqrt{r^2 + r_x^2} \tan R_\theta. \quad (3.2)$$

Concerning the scans above the antenna, they can cover any azimuth angle and a given range of elevation angles. In this case,  $r$  will represent the FF distance along

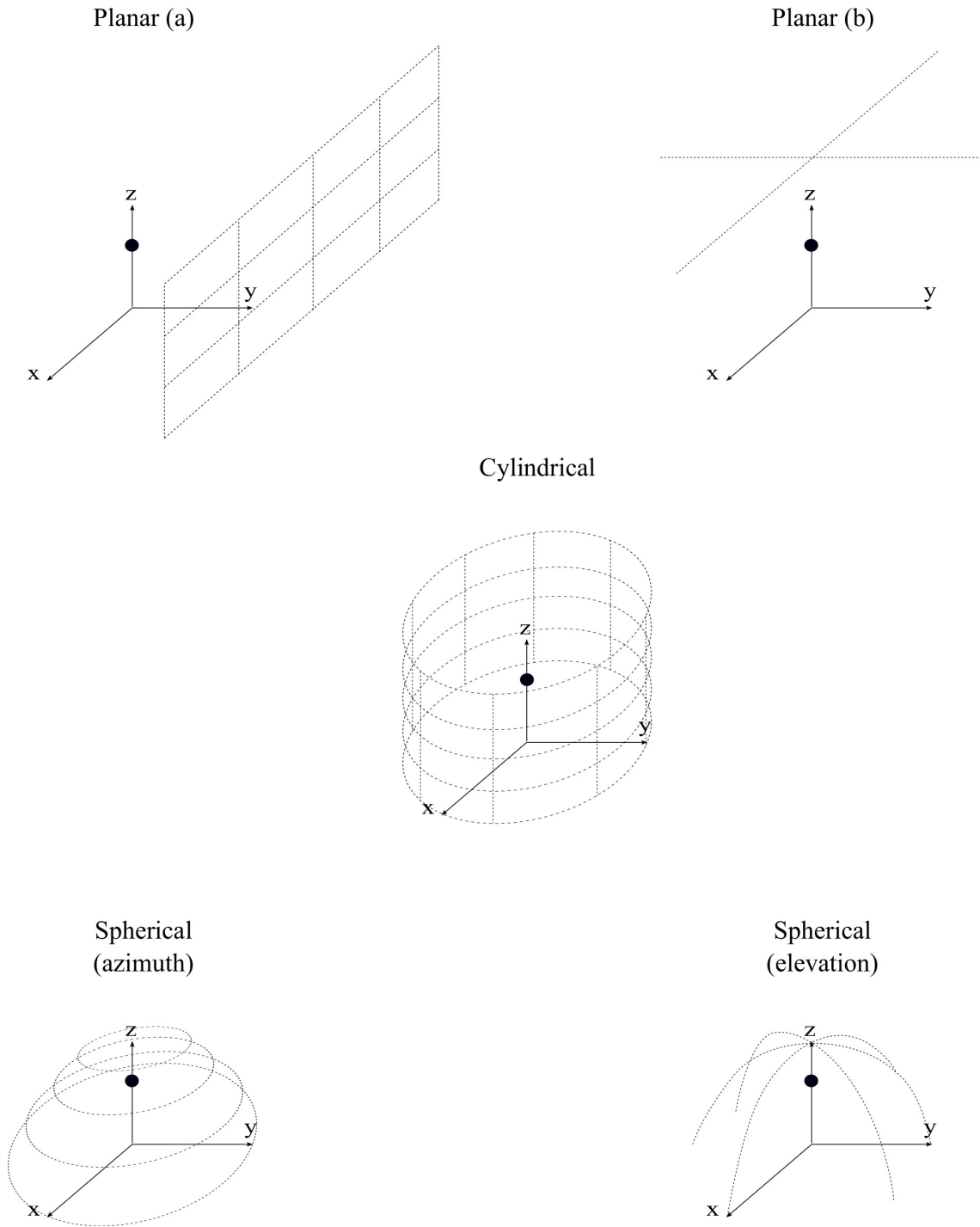


Figure 3.1: Illustration of the possible and common scan types with the UAV-based system. The first row illustrates planar scans, along  $x$  and  $z$  (a), and above the antenna in the  $x$ - $y$  plane (b); the second cylindrical scans and the third spherical scans in both azimuth and elevation.

the  $z$ -axis. The range of elevation angles can then be expressed as  $R_\theta = 2 \arctan \frac{d_{ply}}{2r}$ .

This finally yields the covered distance:

$$d_{ply} = 2r \tan \frac{R_\theta}{2}. \quad (3.3)$$

For all of these scans it is worth noting that the path loss will not be constant.

Thus, it must be corrected in post-processing.

When scanning spherically in azimuth, the measured cut at  $\theta$  corresponds to a distance from the probe to the AUT in the  $x$ - $y$  plane of  $r \sin \theta$ , and to a height of  $r \cos \theta$ . The distance covered, for a range of azimuth angles, is simply expressed as:

$$d_{sph_{az}} = \frac{\pi}{180} R_\phi r \sin \theta. \quad (3.4)$$

When scanning in elevation, for covering a range of elevation angles the distance is simply expressed as:

$$d_{sph_{el}} = \frac{\pi}{180} R_\theta r. \quad (3.5)$$

There are several things worth noting at this point. The path loss is constant for a spherical scan. This means that the spherical scan is the shortest scan to cover a given angle range at a constant distance away from the antenna. Finally, the cylindrical scan is the same as equation 3.4 in azimuth with  $\theta = 90$ —this also describes any spherical elevation scan—, and the same as equation 3.2 in  $z$  with  $r_y = 0$ .

These expression shall be illustrated using the three systems outlined in table

2.2:

- The FF distance for the WSR-88D is  $r = 2\frac{a^2}{\lambda} = 1,459$  m.
- The FF distance for RaXPol is  $r = 2\frac{a^2}{\lambda} = 374$  m.
- The FF distance for the 5G base station antenna was chosen to be 100 m.

Figures 3.2 through 3.4 show, for each scanning strategy—a), b), and c)—, the covered distance versus the range of angles in the measured cut. Since all of these distances are proportional to the FF measurement distance, a scaling factor can be applied if a different measurement distance is used. Moreover, these figures show the time needed for different flight speeds versus the distance covered during the mission.

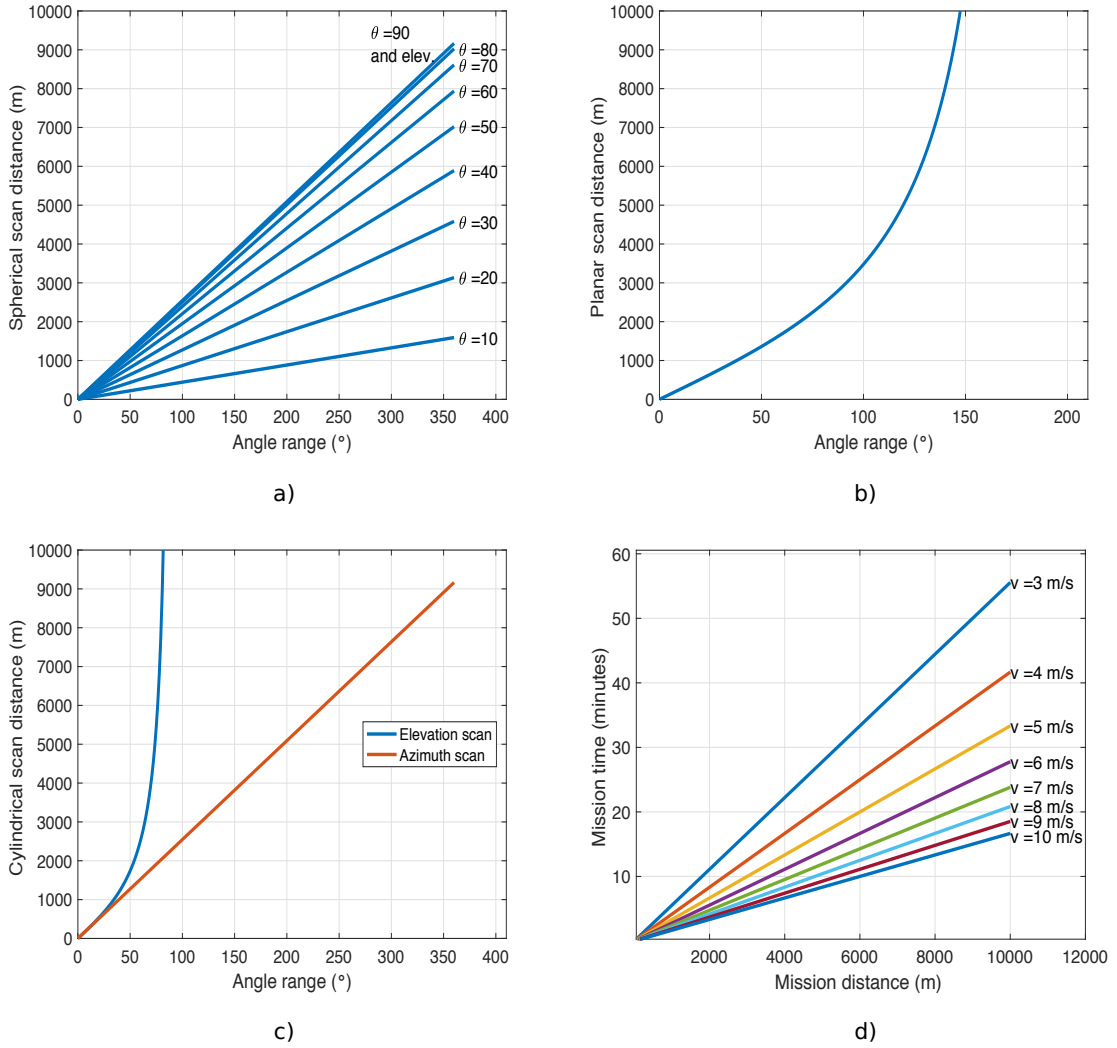


Figure 3.2: The different scanning strategies illustrated with the WSR-88D at a FF distance of 1459 m. The distance to be covered is shown versus the range of angles covered for the measured cut. The time needed to cover a certain distance with the UAV is shown, for different flight speeds. a) shows the spherical scan at different elevation angles in azimuth, while the elevation scans are represented by the azimuth scan at  $\theta = 90^\circ$ . b) shows the planar scan in the  $x - y$  plane above the antenna. c) shows the cylindrical scan both in azimuth in elevation. d) shows the time needed for the UAV to complete a mission of a given distance, for different speeds.

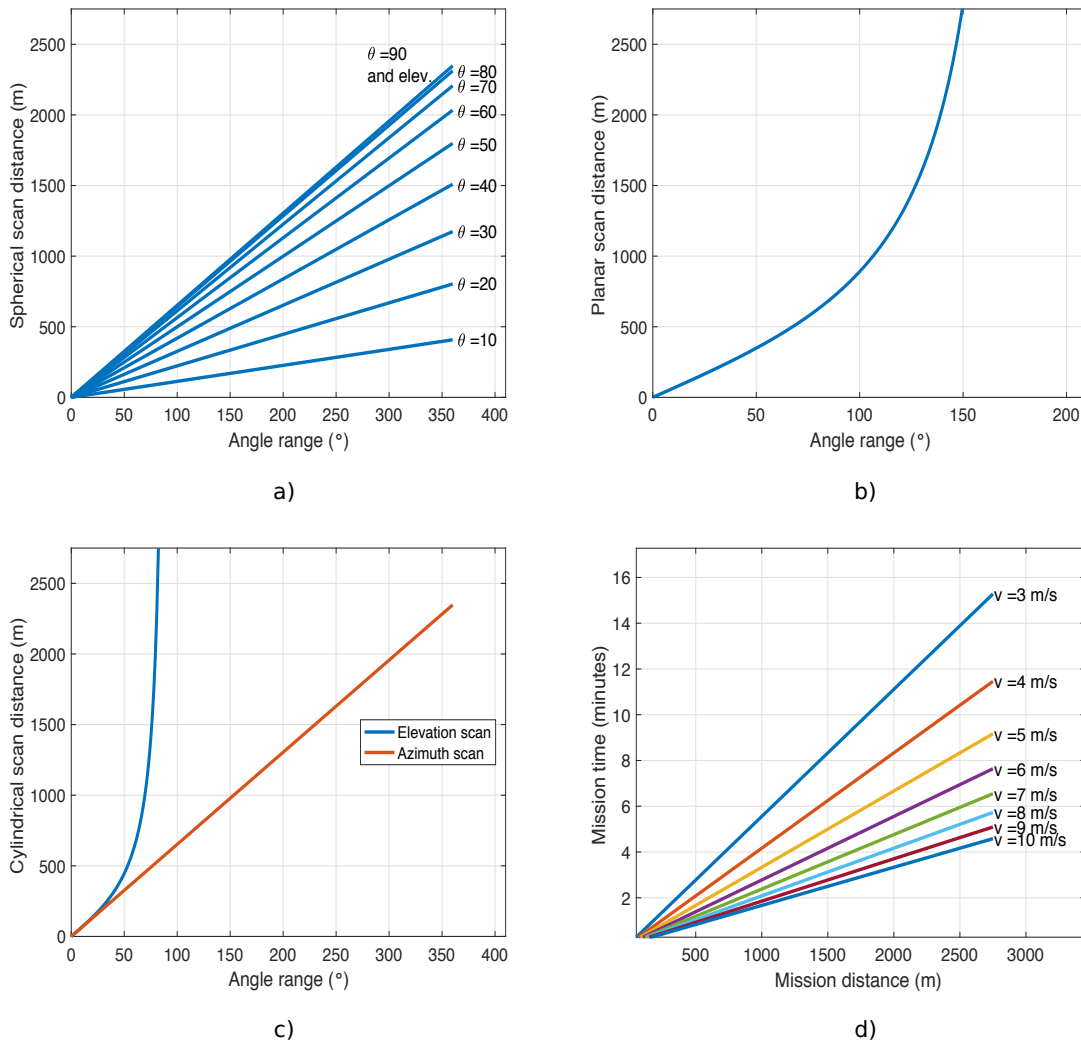


Figure 3.3: The different scanning strategies illustrated with the RaXPoL at a FF distance of 374 m. The distance to be covered is shown versus the range of angles covered for the measured cut. The time needed to cover a certain distance with the UAV is shown, for different flight speeds. a) shows the spherical scan at different elevation angles in azimuth, while the elevation scans are represented by the azimuth scan at  $\theta = 90^\circ$ . b) shows the planar scan in the  $x - y$  plane above the antenna. c) shows the cylindrical scan both in azimuth in elevation. d) shows the time needed for the UAV to complete a mission of a given distance, for different speeds.

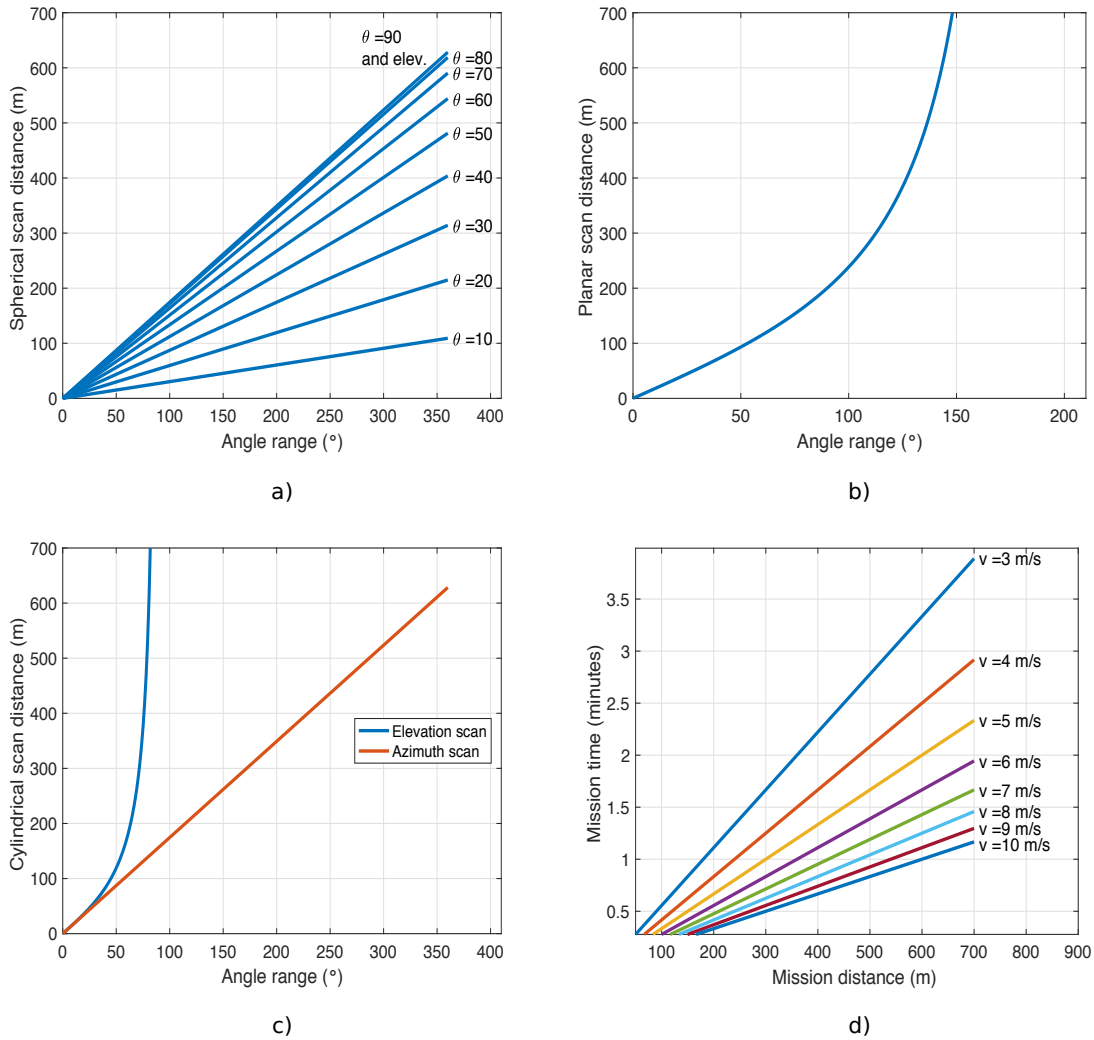


Figure 3.4: The different scanning strategies illustrated with the 5G base station antenna at a FF distance of 100 m. The distance to be covered is shown versus the range of angles covered for the measured cut. The time needed to cover a certain distance with the UAV is shown, for different flight speeds. a) shows the spherical scan at different elevation angles in azimuth, while the elevation scans are represented by the azimuth scan at  $\theta = 90^\circ$ . b) shows the planar scan in the  $x - y$  plane above the antenna. c) shows the cylindrical scan both in azimuth in elevation. d) shows the time needed for the UAV to complete a mission of a given distance, for different speeds.

To use this plot, the user must first determine what kind of scan is desired. If a spherical scan is desired, the plot a) should be used, if a planar scan is desired, the plot b) should be used, and if a cylindrical scan is used, the plot c) should be used.

Once the range of angles to be covered for a single cut has been chosen by the user ( $x$ -axis), it corresponds to the given covered distance ( $y$ -axis). Once the distance to cover a scan is known, the needed flight time can easily be determined from plot d). Indeed, if it is assumed that the flight speed is constant throughout the whole mission, the flight time is simply  $\frac{d}{v}$ , where  $d$  is the covered distance, and  $v$  the flight speed. Therefore, the user can take the distance from the previous step— $x$ -axis of plot d)—, choose a mission speed, and determine how long it will take to complete it— $y$ -axis of plot d).

## 3.2 Ground Reflections

A brief treatment of ground reflections was presented in section 2.2.3. The derived expressions only apply when the distance between the probe and the AUT is such that the angle between the reflected ray and the ground is almost 0. The general case shall be studied in this section. Still referring to figure 2.8, it is seen that the total field at the AUT is the result of two rays, the incident one which corresponds to the shortest distance between the probe and the AUT, and the reflected one which reflects off of the ground at an angle equal to the incident one (Snell's law:  $\theta_i = \theta_r$ ). Therefore, the total electric field at the receiving antenna is:

$$E = \frac{E_i}{r_i} e^{j\phi_i} D_{1_i} D_{2_i} + \Gamma D_{1_r} D_{2_r} \frac{E_i}{r_r} e^{j\phi_r}, \quad (3.6)$$

where the subscripts  $i$  and  $r$  correspond to incident and reflected respectively,  $r$  is the distance traveled by the ray equal to  $\sqrt{d^2 + (h_2 - h_1)^2}$  for the incident ray and

to  $\sqrt{d^2 + (h_2 + h_1)^2}$  for the reflected ray,  $\phi$  is the phase of the field corresponding to  $\frac{2\pi}{\lambda}r$ ,  $\Gamma$  is the ground reflection coefficient, and  $D_1$  and  $D_2$  are the directivities of the transmitting and receiving antennas in the incident direction for the subscript  $i$ , and in the reflected direction for the subscript  $r$ . More precisely, the reflection coefficient,  $\Gamma$ , depends on the polarization and is expressed as, [34]:

$$\Gamma_H = \frac{\eta_1 \cos \theta_i - \eta_0 \cos \theta_t}{\eta_1 \cos \theta_i + \eta_0 \cos \theta_t}; \quad (3.7)$$

$$\Gamma_V = \frac{-\eta_0 \cos \theta_i + \eta_1 \cos \theta_t}{\eta_0 \cos \theta_i + \eta_1 \cos \theta_t}, \quad (3.8)$$

where the subscript  $H$  and  $V$  correspond to horizontal and vertical polarization respectively,  $\eta$  is the medium impedance with 0 being air, and 1 being the ground, and  $\theta_t$  is the transmitted angle of the field into the ground equal to:

$$\arcsin \frac{\beta_0}{\beta_1} \sin \theta_i, \quad (3.9)$$

where  $\beta$  is the propagation constant of the medium, and the incident angle  $\theta_i$  is expressed as:

$$\theta_i = \arctan \frac{d}{h_1 + h_2}. \quad (3.10)$$

Equation 3.6 can be simplified with a few considerations:

- $D_{1r}$  and  $D_{2r}$  are respectively normalized with  $D_{1i}$  and  $D_{2i}$ .
- $E_i$  is taken to be 1.
- We look at the maximum constructive interference only— $\phi_i = \phi_r = 0$ .

- We consider  $r_i = r_r$  to have the same path loss for both rays and simplify the analysis.

Equation 3.6 then reduces to:

$$E = 1 + \Gamma \frac{D_{1r} D_{2r}}{D_{1i} D_{2i}}. \quad (3.11)$$

The only approximation this time is the path loss difference between both rays. This makes the reflected ray's influence more important on the total field, making equation 3.11 more conservative. Finally, for a given value of  $E$  in equation 3.11, the electric field will be somewhere between  $E - 1$  and  $E$  due to  $\phi_i$  and  $\phi_r$ .

When considering the case in section 2.2.3, the magnitude of equation 3.6 reduces to equations 2.8 and 2.9 because  $\Gamma$ ,  $D_1$ , and  $D_2$  are equal to 1—or -1 for  $\Gamma$  depending on the polarization—and the distances of both rays are practically identical and can be simplified with Maclaurin series. Equation 3.6 asserts that the total field at the AUT can vary between 0 and twice the incident field, which translates between no power and 4 times the incident power—about 6 dB. It will depend on  $r$ ,  $\phi$ ,  $\Gamma$ ,  $D_1$ , and  $D_2$ . Among their dependencies, the physical configuration of the measurement setup is what the user has power over. Therefore, particular attention should be brought to the height of both the probe and the AUT, as well as the distance that separates them.

The influence of ground reflections will now be illustrated through some relevant cases. As was just seen, other than the measurement setup, the reflection coefficient,  $\Gamma$ , is dependent upon the constitutive parameters of the ground. The ground can be

composed of elements such as asphalt, some type of soil, vegetation, and can also be dry, damp, or wet. Moreover, the soil has different characteristics according to the geographical location. Consequently, it is impossible to find a unique model which would yield a unique reflection coefficient. Permittivity measurements for loam, clay, and sand for different water contents at frequencies ranging from 1.3 to 10 GHz are presented in [36]. These three types of soil have widely different characteristics, and that the water content makes the permittivity augment drastically—both the real and imaginary parts. Three representative permittivity values were chosen—low, medium, and high— from [36], to show the behavior of the reflection coefficient. These are:

$$\epsilon_l = 3 - j0$$

$$\epsilon_m = 10 - j2$$

$$\epsilon_h = 25 - j6$$

Figure 3.5 shows the corresponding reflection coefficients, for both polarizations, versus the incident angle. It clearly shows that the reflection coefficient increases when the real part of the permittivity increases, and that the reflection coefficient is close to 1 when the incident angle is close to 90°. For V-Polarization, the Brewster angle which represents total transmission into the soil, that is  $\Gamma = 0$ , can be seen.

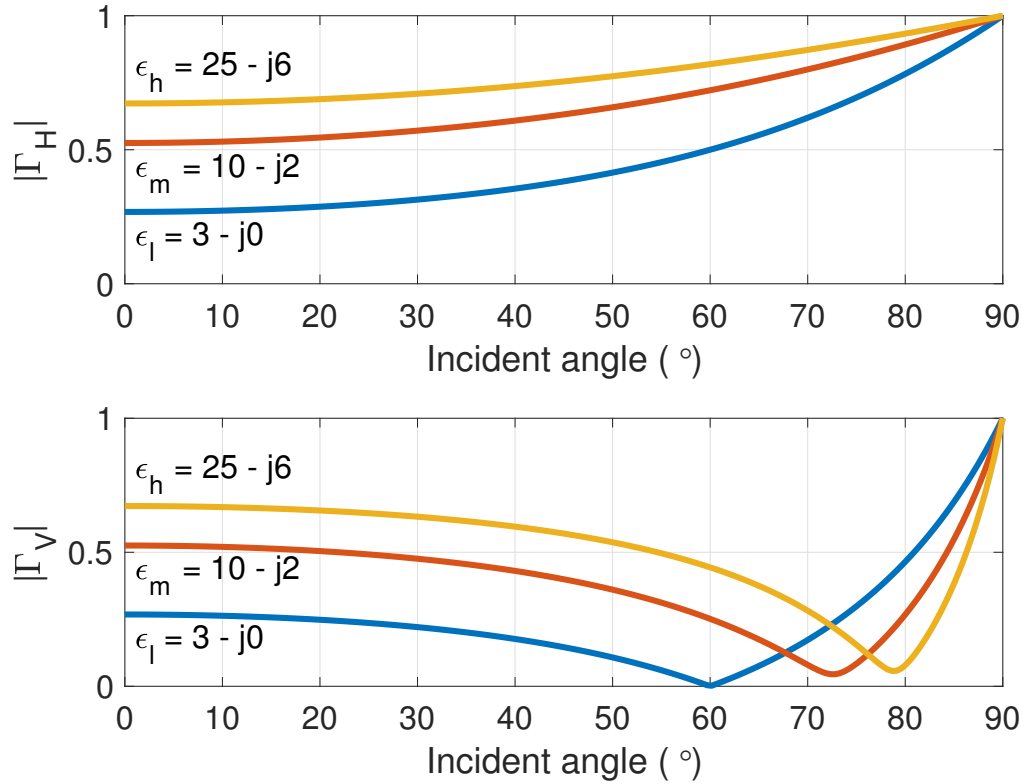


Figure 3.5: Reflection coefficient versus incident angle for 3 different permittivities, representative of soil properties,  $3 - j0$ ,  $10 - j2$ , and  $25 - j6$ .

As far as the directivities  $D_1$  and  $D_2$  are concerned, they are antenna-dependent. As before for the link budget and scanning strategy studies, the cases of weather radar systems—WSR-88D at S-Band and RaXPol at X-Band—and a 5G base station antenna will be used. It is assumed that the RaXPol and WSR-88D have similar antenna patterns so that one case suffices to illustrate the ground reflections. Their pattern is assumed to have a one-degree beamwidth and 30 dB sidelobe level one-way—to worsen the effect of the reflections in a conservative way. This was simulated by a  $60 \times 60 \lambda$  uniform aperture with a Taylor distribution ( $\bar{n} = 6$ ). As for the 5G antenna with a gain of 30 dB at 28 GHz, its pattern was simulated by

a  $32 \times 32$  microstrip patch array with a half-wavelength spacing. For RaXPol at X-Band, the dish is 2.4 m, and for the WSR-88D at S-Band it is 8.54 m. It gives respectively FF distances of 374 m and 1,459 m minimum, for the standard FF criterion. As before, the FF measurement distance for the 5G antenna is taken to be 100 m. The consideration that the maximum UAV altitude is 100 m and that the maximum antenna height is 30 m will be made. Since the incident angle  $\theta_i$  is a dependence for every term in equation 3.11, it is represented on figure 3.6 for the 3 cases, versus  $d$  and  $h_1 + h_2$ , given the aforementioned considerations. From the plots, the the incident angle increases with an increase of  $d$  but decrease with an increase of  $h_1 + h_2$ . A range of incident angles between 40 and 90° captures all the measurement arrangements just described.

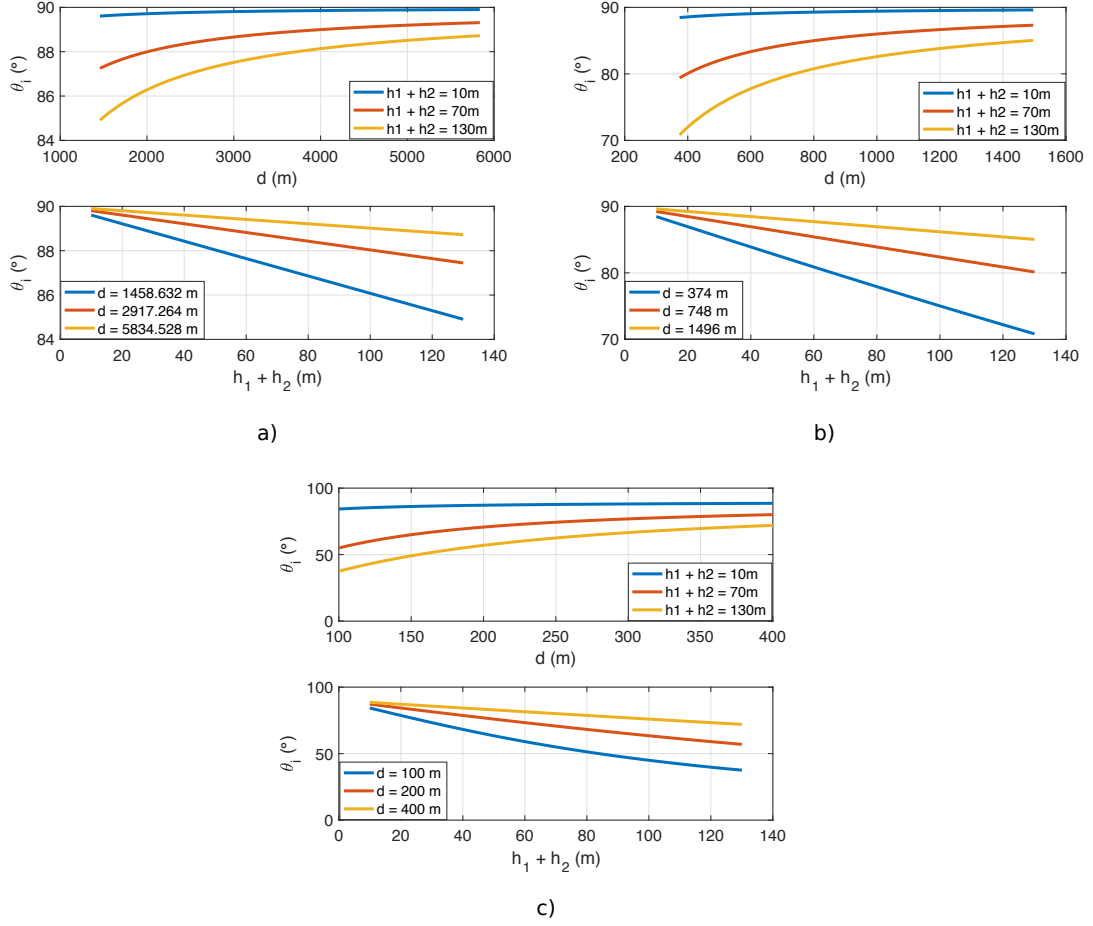


Figure 3.6: Incident angle  $\theta_i$  for the WSR88-D, a), RaXPoI, b), and a 5G base station antenna, c). The top plot shows  $\theta_i$  versus distance for 3 different values of  $h_1 + h_2$ , representing low, medium, and maximum. The bottom plot shows  $\theta_i$  versus  $h_1 + h_2$  for the 3 different values of the measurement distance, once the FF distance, twice the FF distance, and four times the FF distance.

The probe was chosen to be a  $3 \times 3$  microstrip uniform patch array with a half-wavelength spacing, and the permittivity of the ground was conservatively chosen to be the worst,  $25 - j6$ . Finally it is assumed that the radar and the probe are aligned along the horizon. For the weather radars,  $\Gamma$ ,  $D_1$ , and  $D_2$  as well as the total field at the radar, according to equation 3.11, are plotted in figures 3.7 and 3.8 respectively. For the 5G antennas the same plots are shown on figures 3.9 and 3.10. It is worth noting that only angles of incidence superior to  $80^\circ$  are plotted for the

weather radars, because below this value, the total electric field is practically equal to 1. Similarly, a value of  $60^\circ$  was used for the 5G antenna.

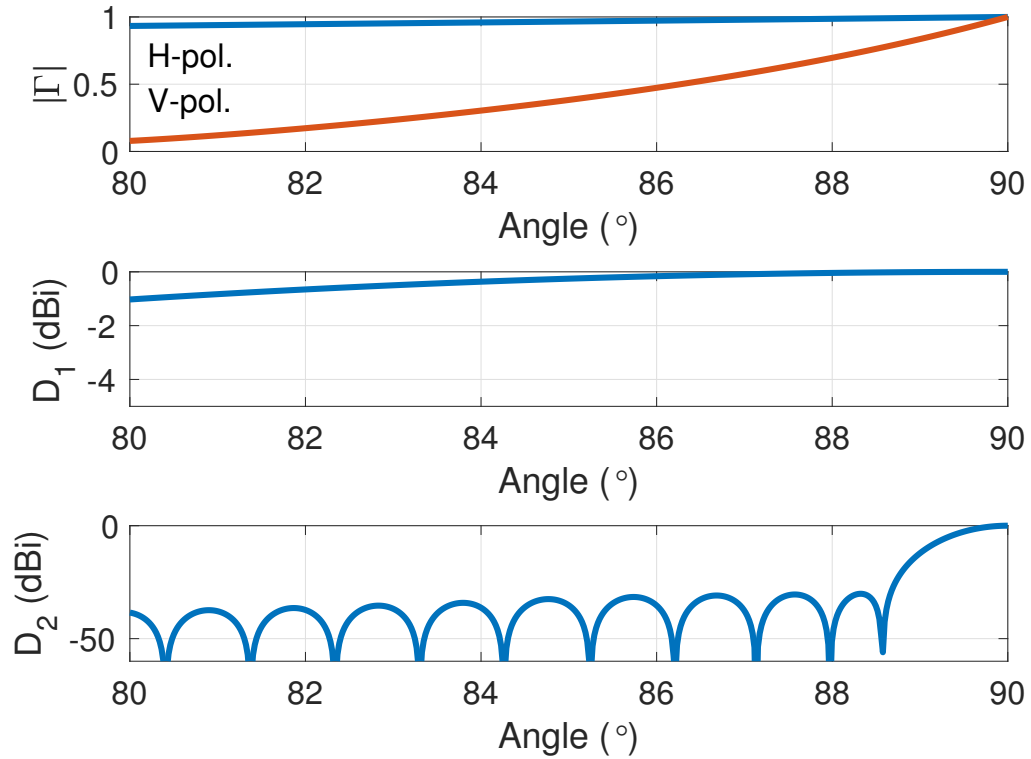


Figure 3.7: Parameters that influence the ground reflections for a  $1^\circ$  3 dB beamwidth and 30 dB sidelobe-level weather radar versus a representative range of incident angles. The top plot is the reflection coefficient for H- and V-polarizations, the middle plot is the probe directivity, and the bottom plot is the radar directivity.

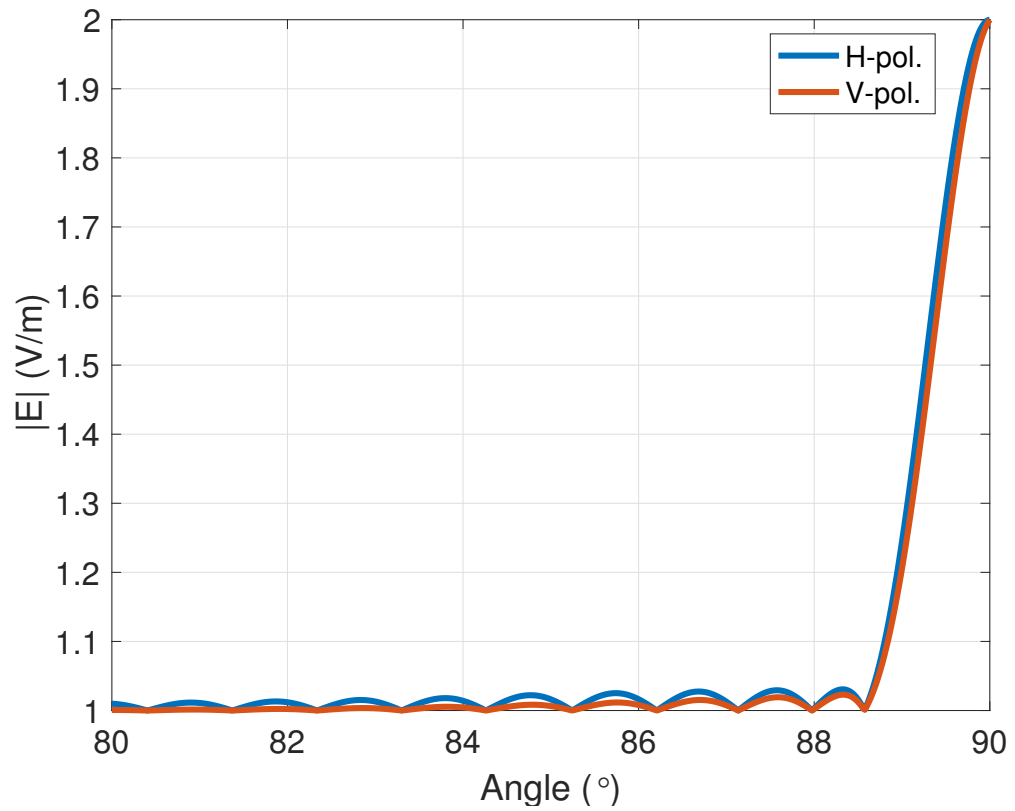


Figure 3.8: Maximum amplitude of the total electric field received at the radar versus a representative range of incident angles, for both H- and V-polarizations.

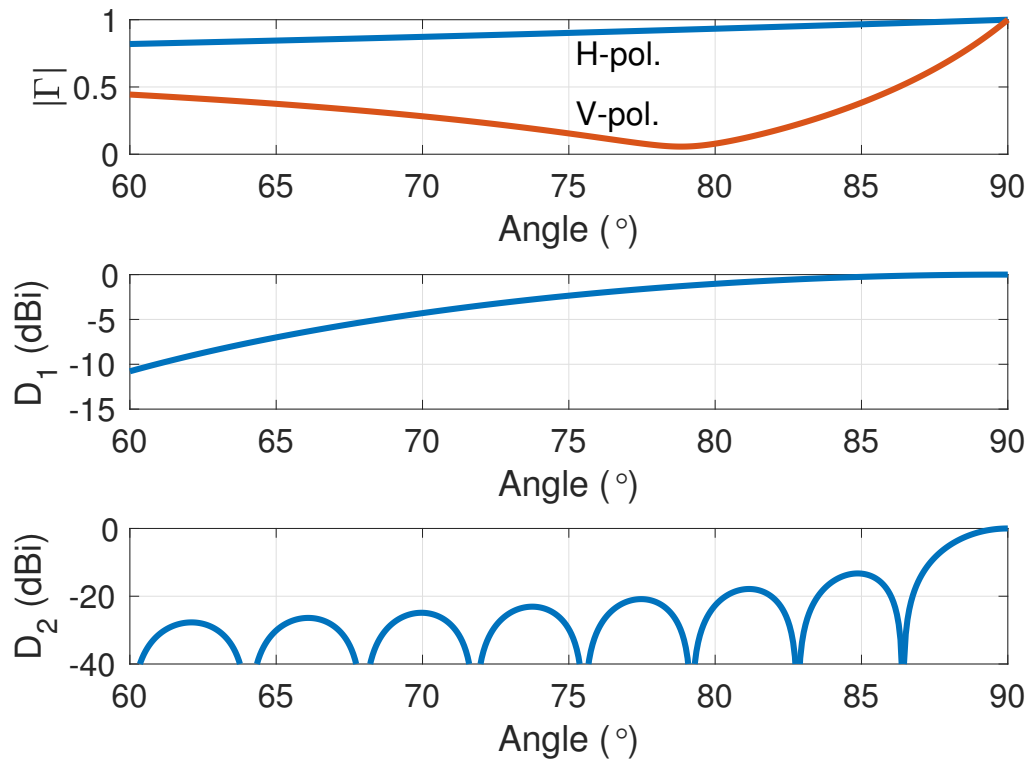


Figure 3.9: Parameters that influence the ground reflections for a 30 dB 5G antenna. The top plot is the reflection coefficient for H- and V-polarizations, the middle plot is the probe directivity, and the bottom plot is the radar directivity.

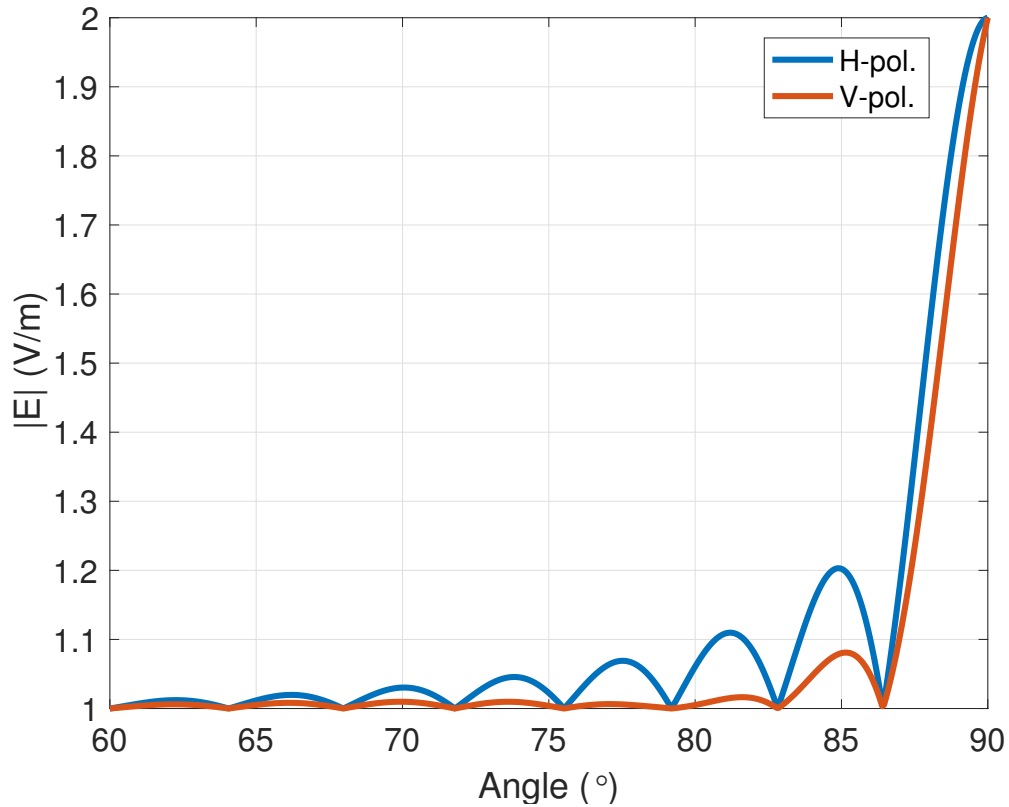


Figure 3.10: Maximum amplitude of the total electric field received at the 5G antenna versus a representative range of incident angles, for both H- and V-polarizations.

Concerning the weather radars, when  $\theta_i$  tends to  $90^\circ$ , the electric field at the AUT is twice the incident field as chapter 2.2.3 suggested. The same observation can be made for the 5G antenna. Then since the patterns of weather radars are very directive with low sidelobes, the influence of ground reflections becomes negligible if  $\theta_i$  is less than the angle where the first null is—about  $88.5^\circ$ . This is seen with values of the electric field of about 1.02. The pattern of the electric fields follows from the AUT pattern. Finally, since the reflection coefficient is higher for H-polarization, the ground reflections have more influence on this polarization. For the 5G antenna, the same observations can be made with the exception that, since

its pattern is not as directive as that of the weather radars, ground reflections have an influence up until an angle  $\theta_i$  of about  $72^\circ$ .

### **3.3 Positioning Accuracy**

Unlike standard measurement techniques where the position of both the probe and the AUT is either fixed or known (and accounted for in post-processing), and the ground reflections are either controlled or cancelled, the situation is different with the proposed measurement technique. There is a position drift between the desired position of the UAV, and its actual position, due to instrumental inaccuracies—GPS, IMU, barometer, gimbal—, environmental conditions such as wind, and the flight controller control technique. The position drift, if known accurately, can be accounted for on the measurements. It creates the requirement of knowing the position in synchronization with the measurements, that is the position drift at a given instant  $t$  must be correlated with the measurement at the same instant  $t$ . In the next paragraphs, standard GPS and RTK GPS systems, as well as IMUs, will be studied, so that the positioning accuracy of the UAV can be modeled and understood. Then the focus will be shifted on gimbal systems, to also evaluate their positioning accuracy.

#### **3.3.1 Inertial Measurement Unit**

An IMU is a device that measures angular and translational acceleration around/along each of the 3 axis of the UAV. This is respectively achieved by a 3-axis gyroscope

and a 3-axis accelerometer. These are the 2 main sensors in an IMU. Then the data is sampled through Analog Digital Converters (ADCs) and processed, and is typically available through a SPI, Serial or I<sup>2</sup>C interface, [37]. Since gyroscopes and accelerometers measure acceleration—angular or translational—, the IMU integrates these values to extract the velocity and the position.

IMUs have their own intrinsic errors, that will affect the acceleration measurements. Moreover, during the integration steps to obtain either the velocity or the position, the errors will grow and also affect these values. The error sources are, [37]:

- The bias error composed of the short-term deterministic offset, which is the value output by the gyroscope or accelerometer when there is actually no acceleration, and of the bias instability which describes how much the short-term deterministic varies over time.
- The scale factor error. A gyroscope or an accelerometer has a linear response of its output with respect to its input. The slope of this response is the scale factor, and is generally obtained through a least squares fit. Since this is not the exact response of the sensor, for a given output point the slope might be different. Therefore, the scale factor error, for a given output, is the ratio of that slope with the slope obtained through the least squares fit.
- Electronic noise, depending on the noise density of the IMU and the bandwidth.

There are a variety of IMUs on the market, perfectly suitable for UAVs. A few different IMUs will be listed alongside their main characteristics, to get a better

grasp of the performance of the systems currently on the market. Three IMUs have been retained here:

- The Invensense MPU-6050 used as the primary IMU in the Pixhawk flight controller.
- The ST Micro LSM303D accelerometer alongside the ST Micro L3GD20H gyroscope as the second IMU for the Pixhawk flight controller.
- The Adafruit LSM9DS0 used in Arduino-based flight controllers.

Table 3.1 sums up the main characteristics of each of these IMUs.

Table 3.1: Summary of UAV IMU characteristics

IMU	Invensense MPU-6050	ST-Micro LSM303D— ST-Micro L3GD20H	Adafruit LSM9DS0
Acc. range ( $g$ )—Gyro. range ( $\frac{\circ}{s}$ )	2 to 16—250 to 2000	2 to 16—245 to 2000	2 to 16—245 to 2000
Bits	16	16—14	16
Short-term bias ( $mg$ — $\frac{\circ}{s}$ )	50—20	60—25	60—25
Bias instability ( $\frac{mg}{\circ C}$ — $\frac{\circ}{\circ C}$ )	0.5—0.16	0.5—0.04	0.5—0.05
Scale factor error (%)	2	2	2
Noise ( $\frac{\mu g}{\sqrt{Hz}}$ — $\frac{m^{\circ}}{\sqrt{Hz}}$ )	400—0.005	150—0.011	Not available

It is seen that these typical IMUs for UAV applications have very similar characteristics, sometimes even identical. The ranges, both for the accelerometer and gyroscope, are sufficient for the UAV, so are the number of bits and therefore the sensitivity. Finally, the errors and the noise are very low.

### 3.3.2 Standard Global Positioning System

GPS is the first Global Navigation Satellite System (GNSS), developed by the Department of Defense (DoD) in the seventies. The access was expanded to civilians in the eighties. A GNSS has satellites orbiting the Earth constantly, which transmit the time of their accurate atomic clock onboard, along side a unique PseudoRandom Noise (PRN) so that they can be uniquely identified by the receiver. When the receiver gets 3 different signals, it can measure the time of arrival of each of them and therefore determine the distance to each satellite thanks to its own clock—by taking the time difference. Consequently, this tells how far the 3 satellites are, and enables the receiver to solve for its own position. A fourth satellite is needed to correct for the GPS receiver clock error, [38]. This is why a GNSS needs to have enough satellites in space, so that from any location in the world, there are at least 4 visible satellites. The last aspect of a GNSS is its ground control stations, which monitor the system of satellites in space and upload any corrections to the satellites, if deviations in time or their trajectories occur. Even though GNSS are referred to as GPS, there are other satellite constellations:

- Global Navigation Satellite System (GLONASS) (Russian).
- BeiDou (Chinese).
- Galileo (European).

The main sources of error in a GPS are, [38]:

- The satellite clock error: even though the atomic clocks are very accurate, they drift between 8.64 to 17.28 ns a day. In terms of range, when multiplied

by the speed of light, it gives a position drift of 2.59 to 5.18 m. This is the standard accuracy of GPS systems.

- The satellite position drift.
- Noise in the receiver.
- Ionospheric and tropospheric effects on the signal propagation—which slow it down.
- RF interference with other devices close by.
- Multipath, which occurs when the receiver gets the signal from the same satellite, from different paths due to reflections off of the ground and nearby objects and structures.

The rest of this section aims at finding a simple model of the position drift of a UAV system with a standard GPS system. The approach that was chosen to this end was to define a flight pattern for the UAV, carry out the corresponding mission, and pull the flight logs from the UAV and analyze the position data. More precisely, the position data comes along 3 axis: North, East, and Down (toward the center of the Earth), which correspond to the standard three-dimensional cartesian coordinate system. The flight mission is recorded as a set of waypoints in the flight controller, from which the latter derives a desired position for the UAV versus time. The actual position of the UAV is estimated from the GPS, the IMUs, the barometer, and a Kalman filter implemented in the flight controller. The position drift is computed to be the difference of these two values. The distribution of the position drift can then be determined, and finally a model can be obtained by data fitting if enough samples were obtained during the flight mission.

According to this procedure, the in-house ARRC hexacopter was used to attempt to model the position drift. It was hovered for half an hour, which gave 16331 position samples. After plotting the position drift, it was noticed that it had a Gaussian pattern for all 3 axis. Therefore, a Gaussian fit was applied. Figure 3.11 shows both the actual position drift, and its Gaussian-fitted counterpart. It is seen that they both fit really closely for all 3 axis. Respectively for each axis, the standard deviations are 24.53, 17.26, and 59.89 cm. In the horizontal plane, the drift magnitude is equal to about a meter, while it is around 3 m in altitude. Consequently, the combination of GPS, IMUs, and barometer with a Kalman filter allow the UAV to increase the positioning accuracy, especially in the horizontal plane, with respect to the standard GPS accuracy.

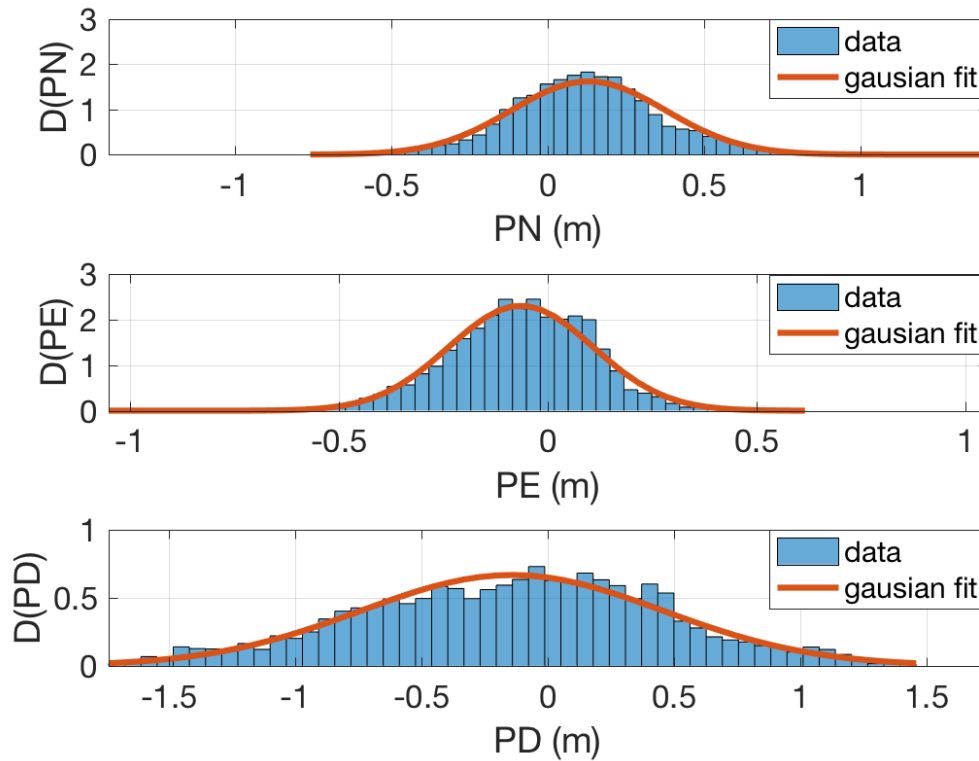


Figure 3.11: Position distributions during hover mode for the in-house ARRC hex-copter. The top plot shows the position along the North, the middle plot the position along the East, and the bottom plot the position along the axis pointing toward the center of the Earth. The blue histogram represents the actual data while the red plot is the gaussian fit applied to it.

### 3.3.3 Real Time Kinematics Global Positioning System

RTK GPS works the same as standard GPS, but with added features to ensure accuracy within a few centimeters. Two GPS receivers are used, the base at an accurate known position on the ground, and the rover located on the vehicle. Using the phase of the satellite signals as well as its own accurate position, the base can use the RTK algorithm to remove the main GPS errors. The base then transmits its corrections to the rover to achieve same level of accuracy. Sometimes, due to

atmospheric conditions or nearby obstructions it is not possible to obtain a RTK fix. However, by using the data from the closest RTK satellite base station—which is released the next day—alongside the standard GPS rover data, it is possible to obtain the RTK positioning accuracy thanks to Post Processing Kinematics (PPK). PPK does the same thing as RTK but not in real time.

At the ARRC, RTK GPS systems are not integrated with UAVs yet. However, they are available and therefore their positioning accuracy can be determined. The one available at the ARRC is the Emlid Reach. A simple test was made in an effort to carry out this task. First, one of the GPS receivers was used by itself outside the ARRC and collected data for 10 minutes without moving, in standard GPS mode. Then, the whole system was used in the same test conditions, that is both receivers as base and rover with the RTK correction running. This process was repeated twice to get 2 datasets. The results are shown on figure 3.12, for the  $x - y$  plane and the  $x - z$  plane.

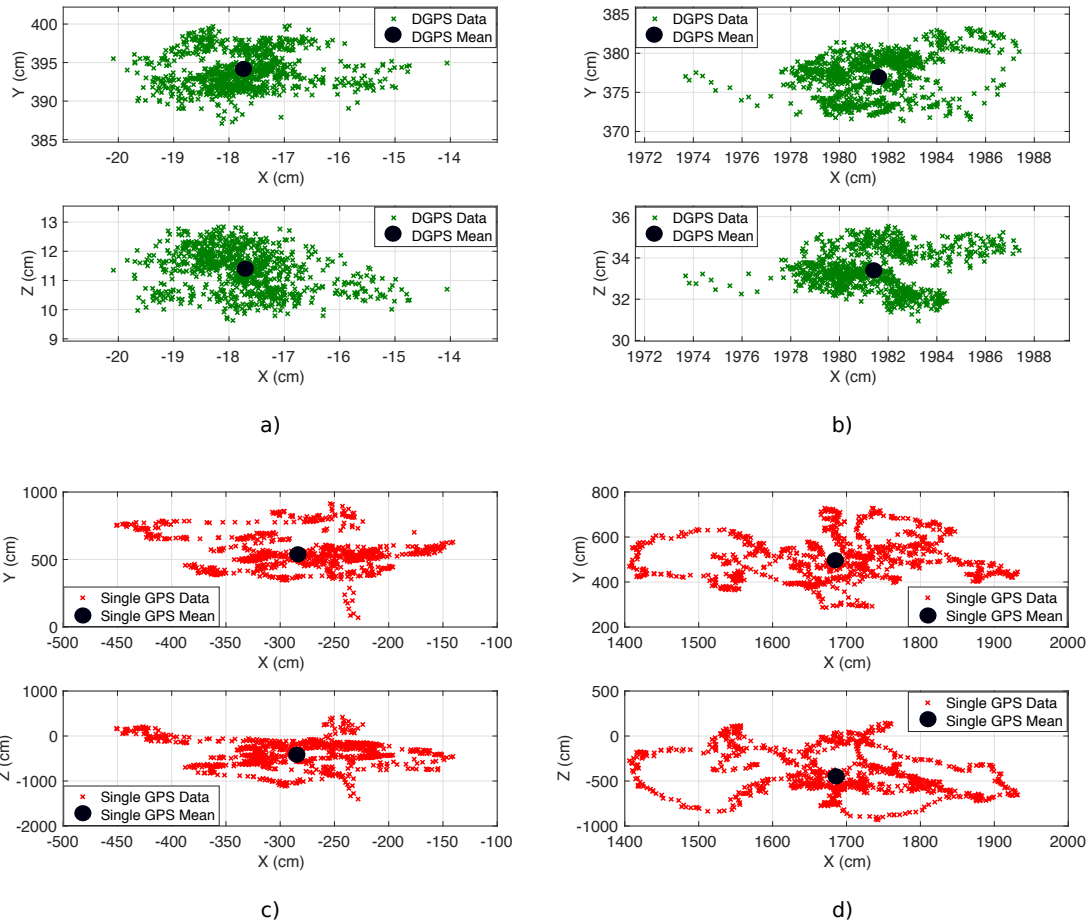


Figure 3.12: Comparison between RTK GPS position data and standard GPS position data for the Emlid Reach, for 2 datasets in static configuration. The top plot shows the  $x - y$  plane while the bottom plot shows the  $x - z$  plane. a) shows the RTK GPS dataset 1, b) shows the RTK GPS dataset 2, c) shows the GPS dataset 1, and d) shows the GPS dataset 2.

It can be seen that for the RTK datasets, the positioning accuracy is better than 15 cm on all axis, while for the standard GPS it is worse than 5 m on all axis. Table 3.2 lists the standard deviations for all datasets as well as the dataset from section 3.3.2, and on each axis. It is interesting to note that the positioning accuracy of the hexacopter with a standard GPS, aided by IMUs, is significantly better than a standard GPS system alone, but not as performant as a RTK GPS system.

Table 3.2: Standard deviation—in cm—for all datasets of the Emlid Reach in GPS and RTK GPS modes as well as the hexacopter with a standard GPS, along each axis.

Mode—Dataset	$x$ axis	$y$ axis	$z$ axis
Hexacopter	24.53	17.26	59.89
GPS—1	64.37	130.38	295.8
GPS—2	117.7632	94.5333	244.5441
RTK GPS—1	0.9064	2.4115	0.7077
RTK GPS—2	2.0611	2.7161	0.9741

### 3.3.4 Gimbal

Another component contributing to the positioning accuracy of the UAV is the gimbal. A gimbal is a 2 or 3-axis system which carries the UAV’s payload and has 2 or 3 degrees of freedom. If it is 3 axis, it has 3 degrees of freedom around each of the attitude angle of the UAV: roll, pitch, and yaw. If it is 2 axis, yaw is generally fixed and there are only 2 degrees of freedom. There are two modes of operation with the gimbal, aided by its own IMUs as well as the GPS:

- Fixed mode, where the gimbal points toward the same orientation at any given time, regardless of the UAV’s orientation.
- Follow mode, where the gimbal keeps the same orientation with respect to the UAV, regardless of its orientation.

In the case of antenna measurements when the UAV is flying around the AUT, the first mode, fixed mode, is required, so that the probe mounted on the UAV and the AUT maintain the same alignment throughout the measurements.

In order to characterize the accuracy of a gimbal system, the following test was carried out: one of the ARRC's in-house UAVs was placed on a pedestal in a FF anechoic chamber. On the other pedestal, a MVG-SH2000 horn was mounted. Both the antenna placed on the UAV gimbal—a  $3 \times 3$  S-Band single layer FR4 microstrip array—and the horn were aligned along their broadside direction. The array central embedded element was excited by a RF signal generator at 3 GHz, while the received power on the receiving horn was read by a handheld power spectrum analyzer. This experiment was carried out when the gimbal had its 3 axis mechanically blocked, and when the gimbal was controlled by the flight controller and its own controller in fixed mode. Data was recorded for around 10 minutes with a running average over every 10 samples. The result of these measurements are presented in figures 3.13 and 3.14.

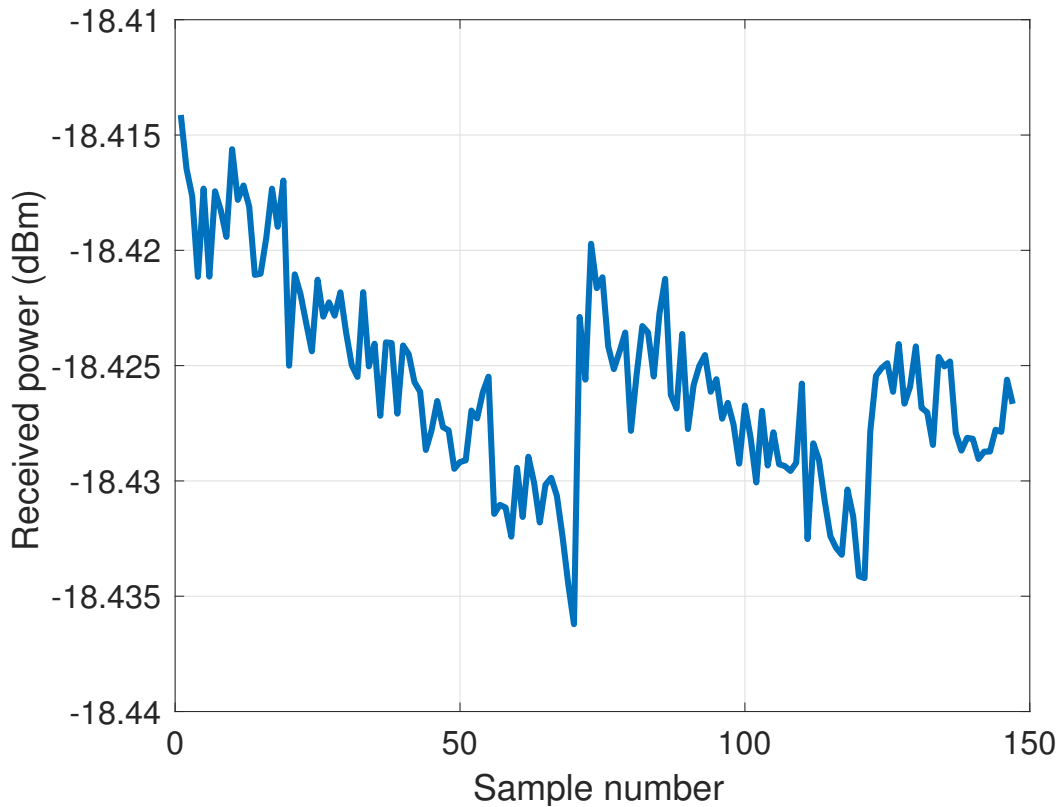


Figure 3.13: Received power at the MVG SH-2000 antenna terminals, when excited by the central embedded element of a S-Band single layer FR4 microstrip array at 3 GHz, mounted on the UAV’s gimbal. The gimbal’s motors were mechanically blocked and both antennas were aligned along their broadside directions.

It is seen that the received power has a maximum magnitude oscillation of two tenths of a dB—half a percent, which makes it almost constant. This value can be attributed to measurement uncertainty, itself due to factors such as noise and equipment uncertainty. The standard deviation of this dataset is 0.0043 dB, which further asserts that the power is quasi constant.

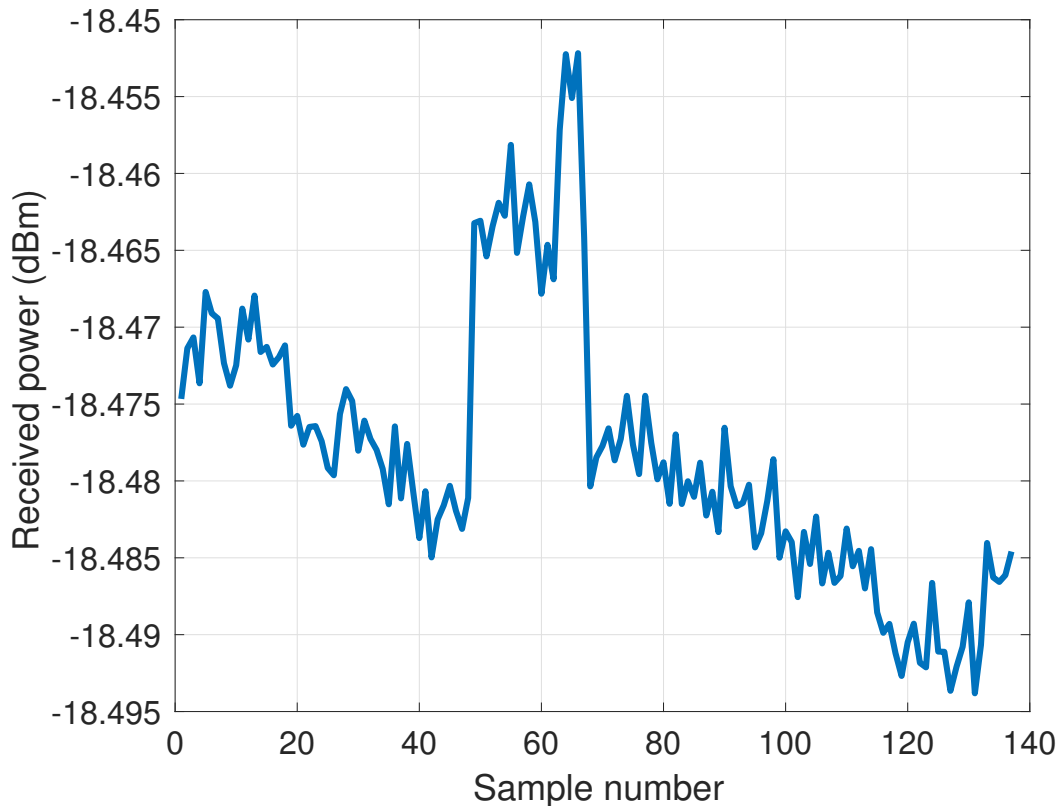


Figure 3.14: Received power at the MVG SH-2000 antenna terminals, when excited by the central embedded element of a S-Band single layer FR4 microstrip array at 3 GHz, mounted on the UAV’s gimbal. The gimbal was controlled by the flight controller and its own controller (using feedback from its own IMUs and the GPS) and both antennas were aligned along their broadside directions.

When the gimbal is on, it can be seen that the magnitude oscillation is about 4 tenths of a dB—0.92 percent. With a standard deviation of 0.0090 dB, this oscillation can be attributed to measurement uncertainty. No significant gimbal drift can be observed for this measurement.

### 3.3.5 Effect on the measurements

The UAV position and gimbal drifts cause antenna pattern measurement errors. Precisely, the position drift of the UAV causes the measurement of a different antenna pattern angle, and the gimbal drift causes the probe mounted on the antenna to excite the AUT—or receive the AUT signal—at a different angle. Moreover, the UAV position drift modifies the path loss. According to the standard antenna coordinate system, these effects can be divided into azimuth and elevation angle variations. This is illustrated in figures 3.15 and 3.16.

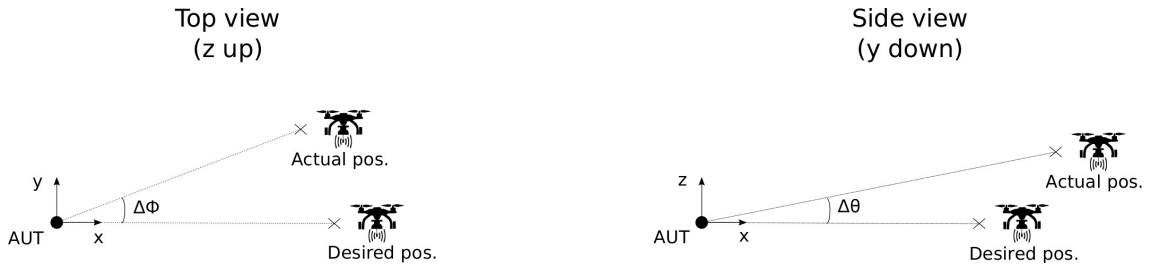


Figure 3.15: Illustration of the position drift effect on the antenna pattern measurements. The UAV measures the AUT radiation pattern at different angles in azimuth and elevation.  $\Delta\Phi$  and  $\Delta\theta$  correspond to these errors respectively.



Figure 3.16: Illustration of the gimbal drift effect on the antenna pattern measurements. The probe mounted on the UAV excites the AUT—or receive its signal—at different angles in azimuth and elevation.  $\Delta\Phi$  and  $\Delta\theta$  correspond to these errors respectively.

As far as the UAV position drift is concerned, let  $x$ ,  $y$ , and  $z$  denote the desired position of the UAV in the cartesian coordinate system whose origin is the AUT—as

in figure 3.15, and  $\Delta x$ ,  $\Delta y$ , and  $\Delta z$  the position drift such that  $x + \Delta x$ ,  $y + \Delta y$ , and  $z + \Delta z$  denote the actual position of the UAV. This leads to:

$$\Delta\theta = \left| \arccos \frac{z}{r_{des}} - \arccos \frac{z + \Delta z}{r_{act}} \right|, \quad (3.12)$$

where  $r_{des} = \sqrt{x^2 + y^2 + z^2}$  and  $r_{act} = \sqrt{(x + \Delta x)^2 + (y + \Delta y)^2 + (z + \Delta z)^2}$

and

$$\Delta\Phi = \left| \arctan \frac{y}{x} - \arctan \frac{y + \Delta y}{x + \Delta x} \right|. \quad (3.13)$$

The path loss difference, in dB, is expressed as:

$$\Delta PL = \left| 10 \log \left( \frac{\lambda}{4\pi r_{des}} \right)^2 - 10 \log \left( \frac{\lambda}{4\pi r_{act}} \right)^2 \right|. \quad (3.14)$$

As far as the UAV gimbal drift is concerned, let us assume the gimbal drifts from its desired pointing direction  $(\Phi, \theta) = (0, 0)$ —which means it is along the most directive direction of the probe—by  $\Delta\Phi$  and  $\Delta\theta$ . This signifies that the probe now excites the AUT—or receives its signal—in the direction  $(\Delta\Phi, \Delta\theta)$ . If  $D_p$  denotes the directivity of the probe in dBi, the error corresponding to the gimbal drift will be:

$$\Delta D_p = D_p(0, 0) - D_p(\Delta\Phi, \Delta\theta). \quad (3.15)$$

This error can be extracted directly from the antenna pattern of the probe mounted on the UAV. The more directive the probe, the higher this error is.

An illustration of the error stemming from the UAV position drift shall be presented. The WSR-88D, RaXPol, and the 5G base station antenna will be used, with their respective FF distances of 1,459, 374, and 100 m. Referring to section 3.3.2, the maxima of  $\Delta x$  and  $\Delta y$  are chosen to be 1 m while the maximum of  $\Delta z$  is chosen to be 1.5 m. According to equations 3.12 through 3.14, the maxima of  $\Delta\Phi$ ,  $\Delta\theta$ , and  $\Delta PL$  are reported in table B.1.

Table 3.3: Effect of the UAV position drift on  $\Delta\Phi$ ,  $\Delta\theta$ , and  $\Delta PL$  for the WSR-88D, RaXPol, and the 5G base station antenna

	$\Delta\Phi_{max}(\text{°})$	$\Delta\theta_{max}(\text{°})$	$\Delta PL_{max}(dB)$
WSR-88D	0.039	0.059	0.0060
RaXPol	0.15	0.23	0.023
5G	0.58	0.87	0.088

It is observed that the angular errors for RaXPol and the 5G base station antenna can be significant since the antenna patterns are directive. For WSR-88D however, these errors are negligible. For all systems, the path loss difference can also be neglected. It should be kept in mind that with RTK or PPK, these errors can be accounted for in post-processing.

The UAV gimbal drift shall now be illustrated, according to equation 3.15. The probe pattern is chosen to be that of a single patch antenna, a  $3 \times 3$  patch antenna array, and a  $8 \times 8$  patch antenna array. Only the E-Plane is considered as it is more directive than the H-Plane, and it is assumed to be in the  $\Phi$  direction. The gimbal

drift is considered to be 0.1, 1, and 5° respectively, in the  $\Phi$  direction. Table 3.4 sums up the results.

Table 3.4: Effect of the UAV gimbal drift on  $\Delta D_p$  for a single patch antenna, a 3×3 patch antenna array, and 8×8 patch antenna array

Gimbal drift (°)	0.1	1	5
$\Delta D_p$ for single patch (dB)	0	0.0014	0.036
$\Delta D_p$ for 3×3 array (dB)	0	0.010	0.25
$\Delta D_p$ for 8×8 array (dB)	0	0.07	1.82

It is observed that the single patch enables the gimbal drift to be neglected due to its broad antenna pattern. Concerning the 3×3 and 8×8 arrays, only the gimbal drift of 5° gives significant errors. This value of the drift, however, is extreme and will most likely not occur. It can be concluded that if the gimbal drift is less than 1°, the measurements will not be affected, even with a directive probe.

### 3.4 Structural Effects on the Probe’s

#### RF Performance

On a UAV system carrying a probe, the UAV components—frame, motors, propellers, gimbal for instance—are in the vicinity of the antenna. Therefore, when the probe radiates power, some of it will inevitably be intercepted by the structure. This will translate into surface currents onto the different components of the structure, that will in terms reradiate some power. This phenomenon will affect the probe

FF antenna patterns. It will mainly depend on the structure electrical size, shape, constitutive parameters, electrical distance from the antenna, relative position with respect to the antenna, and the probe's intrinsic RF characteristics.

The probe's antenna pattern could be significantly affected, under the form of ripples and dips, and altered sidelobe level and overall shape. To avoid this and preserve the intrinsic characteristics of the probe as much as possible, an electrically small structure whose different components have permittivities close to that of air would be preferable. Moreover, if the probe has directive properties, it will radiate low amounts of power toward the structure, which will further limit this phenomenon. The notion of relative position of the probe with respect to the UAV structure is intertwined with that of the probe's intrinsic characteristics, because if the UAV structure is placed in region where the probe radiates little power, this phenomenon will be limited for the same reasons. Unfortunately, because it is easier and financially more advantageous to design a UAV system with off-the-shelf components, it becomes impossible to act on the majority of these factors. However, it is still possible to choose a probe with proper intrinsic characteristics, and to use RF absorbing material on the areas of the UAV structure that are the most critical in terms of current density. The probe must not be chosen to be too directive, because the position drift of the UAV system, which causes some misalignment between the probe and the AUT, could be such that the probe's directivity fluctuates too much throughout the measurements, making them unusable.

The theoretical formulation of the effects of such a phenomenon on the probe's antenna patterns is a formidable task, the best resort is to use an electromagnetic

modeler/solver capable of simulating such a system. Wipl-D is a solver based on the Method of Moments (MoM) that can simulate antenna systems on arbitrary metallic and dielectric structures, quickly and accurately, [39]. Therefore, Wipl-D was used to model two of the ARRC's in-house UAVs—one hexacopter and one octocopter—and one commercial UAV—DJI Phantom 3. Concerning the antenna, two solutions were studied: a  $2 \times 2$  and a  $3 \times 3$  dual-polarized S-Band single layer FR4 microstrip arrays. These configurations were chosen because of their sizes that are compatible with the gimbal mounted on the UAV systems, as well as the availability of different antenna patterns, more or less directive. All simulations were carried out at 3 GHz. The 3 aforementioned platforms were first simulated with the  $3 \times 3$  array, in a single central embedded element configuration—both polarizations—, to see how each platform affects the antenna patterns. Following, the focus was shifted toward the hexacopter, which is currently the prime platform at the ARRC, with the following configurations:

- All elements, both polarizations.
- Central row, both polarizations.
- Central column, both polarizations.

Finally, the same hexacopter was used but with the  $2 \times 2$  array, with all the elements excited.

### **3.4.1 Platform Comparison with $3 \times 3$ Array**

In this section, the effects of the 3 different structures on the antenna patterns will be compared on the central embedded element configuration of the  $3 \times 3$  array. Because

the DJI Phantom 3 cannot accommodate such a big antenna, the single cell was used. Results are presented in figures 3.17 and 3.18 for the DJI Phantom 3, figures 3.19 and 3.20 for the hexacopter, and figures 3.21 and 3.22 for the octocopter. Each figure shows the current densities on the platform and the antenna, alongside the antenna patterns in the 3 principal planes, with and without the UAV.

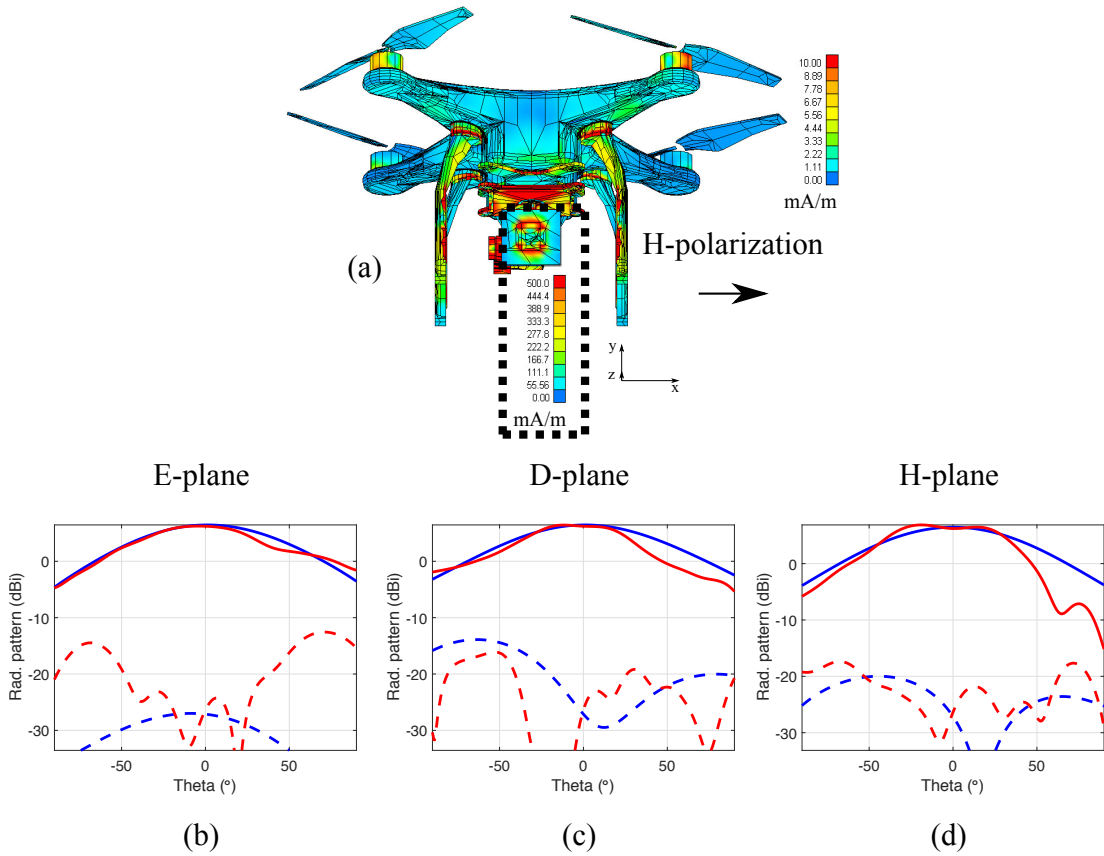


Figure 3.17: Effect of the DJI Phantom 3 structure on the antenna pattern: single cell of a single layer FR4 microstrip array, horizontally polarized. (a) Current density on the probe and the UAV structure. (b) E-Plane antenna patterns with and without the UAV (red and blue respectively). (c) D-Plane antenna patterns with and without the UAV (red and blue respectively). (d) H-Plane antenna patterns with and without the UAV (red and blue respectively).

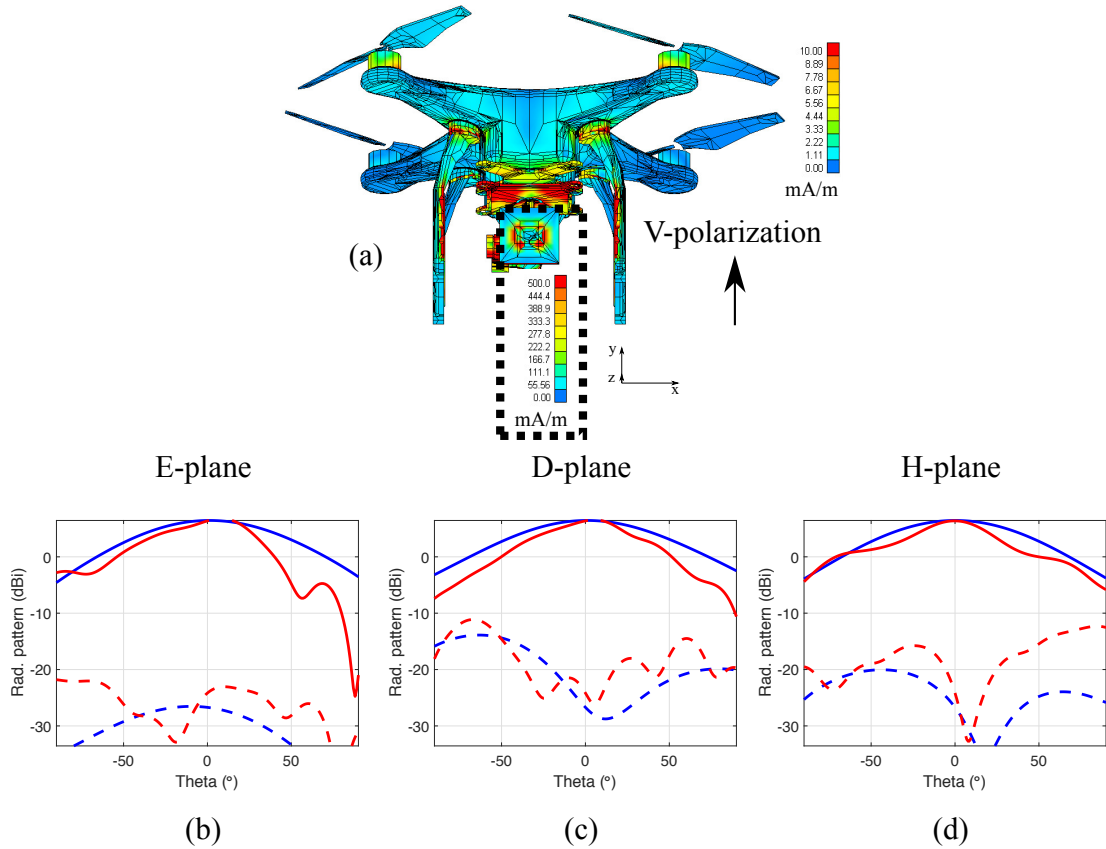


Figure 3.18: Effect of the DJI Phantom 3 UAV structure on the antenna pattern: single cell of a single layer FR4 microstrip array, vertically polarized. (a) Current density on the probe and the UAV structure. (b) E-Plane antenna patterns with and without the UAV (red and blue respectively). (c) D-Plane antenna patterns with and without the UAV (red and blue respectively). (d) H-Plane antenna patterns with and without the UAV (red and blue respectively).

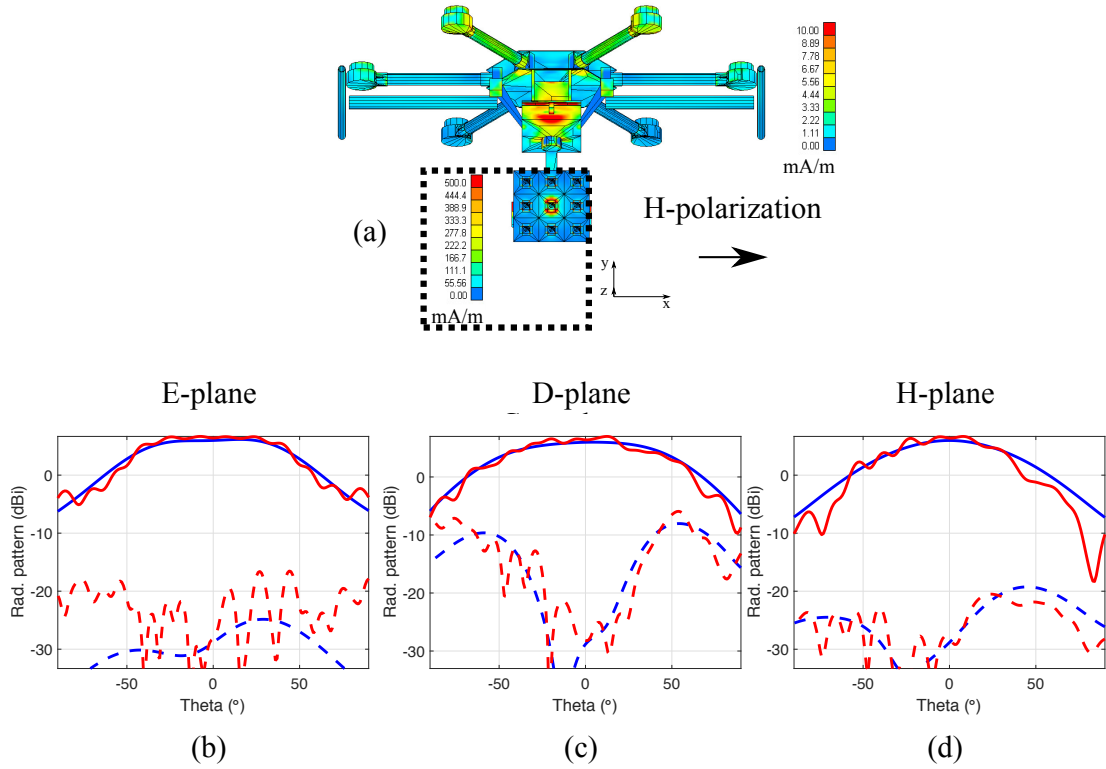


Figure 3.19: Effect of the hexacopter UAV structure on the antenna pattern: central embedded element of a  $3 \times 3$  S-Band single layer FR4 microstrip array, horizontally polarized. (a) Current density on the probe and the UAV structure. (b) E-Plane antenna patterns with and without the UAV (red and blue respectively). (c) D-Plane antenna patterns with and without the UAV (red and blue respectively). (d) H-Plane antenna patterns with and without the UAV (red and blue respectively).

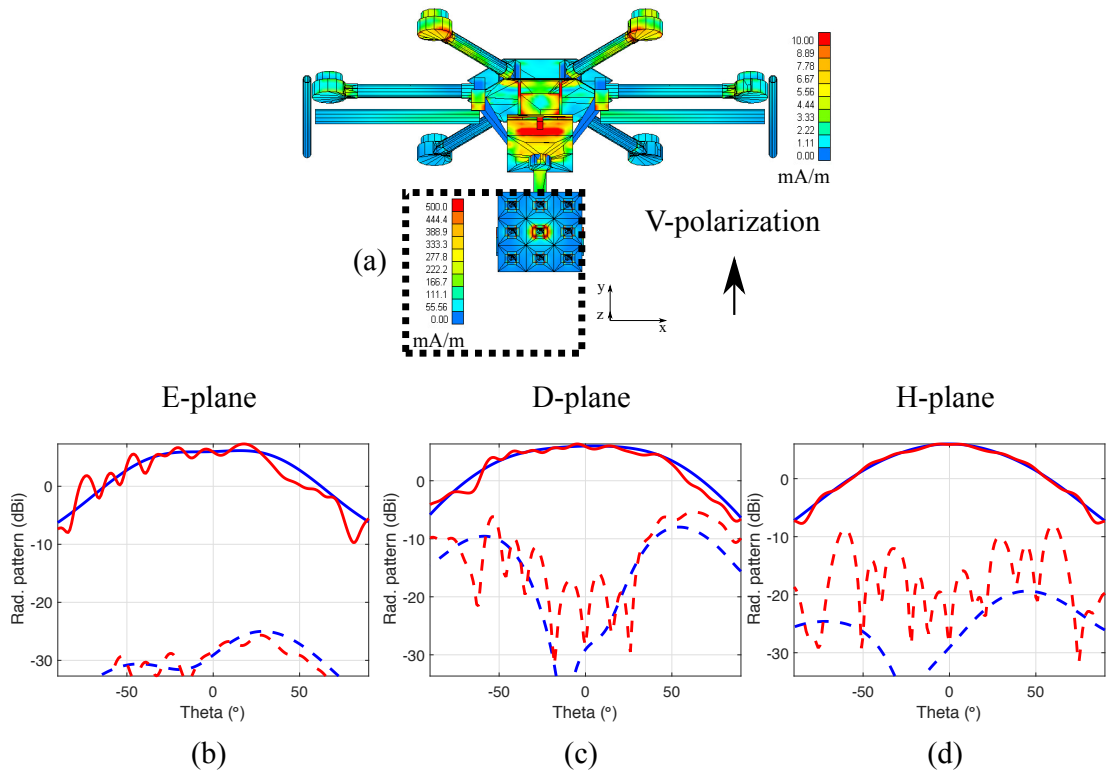


Figure 3.20: Effect of the hexacopter UAV structure on the antenna pattern: central embedded element of a  $3 \times 3$  S-Band single layer FR4 microstrip array, vertically polarized. (a) Current density on the probe and the UAV structure. (b) E-Plane antenna patterns with and without the UAV (red and blue respectively). (c) D-Plane antenna patterns with and without the UAV (red and blue respectively). (d) H-Plane antenna patterns with and without the UAV (red and blue respectively).

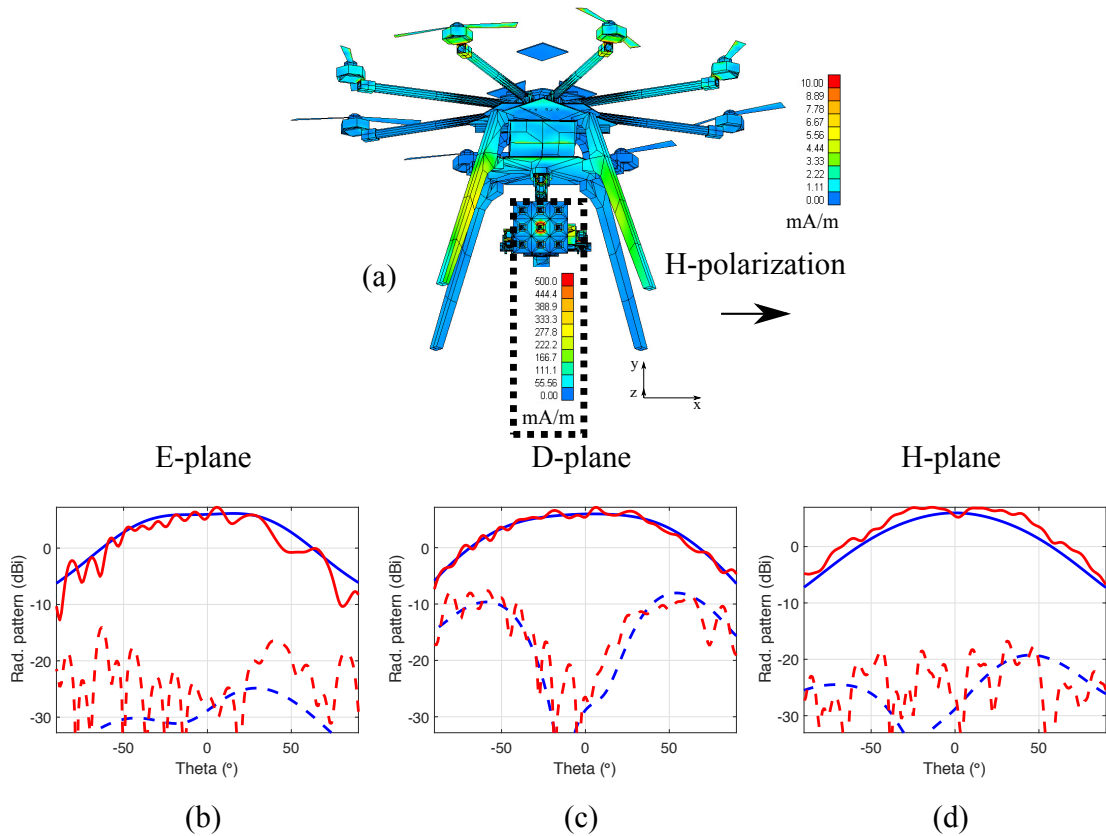


Figure 3.21: Effect of the octocopter UAV structure on the antenna pattern: central embedded element of a  $3 \times 3$  S-Band single layer FR4 microstrip array, horizontally polarized. (a) Current density on the probe and the UAV structure. (b) E-Plane antenna patterns with and without the UAV (red and blue respectively). (c) D-Plane antenna patterns with and without the UAV (red and blue respectively). (d) H-Plane antenna patterns with and without the UAV (red and blue respectively).

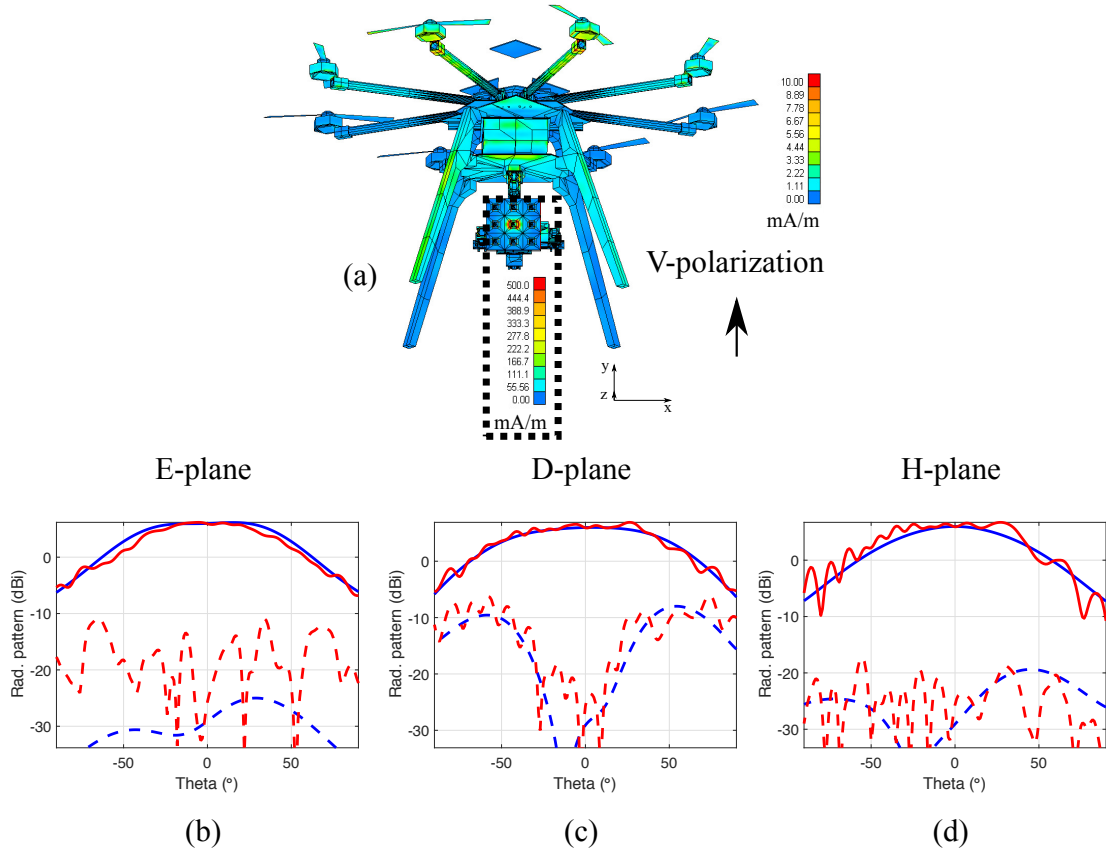


Figure 3.22: Effect of the octocopter UAV structure on the antenna pattern: central embedded element of a  $3 \times 3$  S-Band single layer FR4 microstrip array, vertically polarized. (a) Current density on the probe and the UAV structure. (b) E-Plane antenna patterns with and without the UAV (red and blue respectively). (c) D-Plane antenna patterns with and without the UAV (red and blue respectively). (d) H-Plane antenna patterns with and without the UAV (red and blue respectively).

Some general observations, regardless of the array configuration, can be made. It is observed that the effect of the UAV is to add ripples and dips on the antenna patterns, as well as modify their shape. Moreover, the cross-polarization levels tend to be affected only slightly and not adversely, but rise, in a few cases, by 10/15 dB over the intrinsic level. Given the 3D orientation of the model, it is seen that the H-plane for H-polarization and the E-plane for the V-polarization are the most affected ones, because this is where the UAV lies. Obviously, the cross-polarization

in the E-plane for H-polarization and H-plane for V-polarization is the most affected, according to the same reason. Even though the current densities seem to be higher for V-polarization, the effect on the antenna patterns remains similar between both polarizations. The current densities are the strongest on the gimbal, the plate directly above the antenna, as well as on the 2 motors and arms directly above the antenna. In the case of the octocopter and the Phantom 3, the legs are also a location where current densities are strong. Therefore, these are the areas that should be covered with absorbers to limit the effect of the UAV structure on the antenna patterns. Table 3.5 sums up the ripple level on the antenna patterns for each case that was just presented. It can be seen that, for the DJI Phantom 3, the antenna patterns are modified but do not have any fast-changing ripple. The patterns are modified with a steeper rolloff at the angles where the drone lies. As far as the hexacopter and the octocopter are concerned, ripples are present with amplitudes from 0.3 to 3.3 dB. It can be concluded that larger structures will introduce larger oscillations in the antenna patterns, which corroborates the affirmation that an electrically small structure should be chosen.

Table 3.5: Maximum oscillation level (dB), from  $-45$  to  $45^\circ$  for the antenna patterns of the  $3 \times 3$  S-Band single layer FR4 microstrip array mounted on the DJI Phantom 3, hexacopter, and octocopter

Drone Excitation— Polarization	E-Plane	D-Plane	H-Plane
DJI Phantom 3 Single—H	0	0	0
DJI Phantom 3 Single—V	0	0	0
Hexacopter Single—H	0.3	0.7	1
Hexacopter Single—V	3.3	0.9	0
Octocopter Single—H	2.9	1.4	1.8
Octocopter Single—V	0.3	1	1

### 3.4.2 Hexacopter with $3 \times 3$ Array

The three other excitations described earlier were simulated for the hexacopter. The results are presented below, in figures 3.23 through 3.28. For each of the 6 cases, the current density on the UAV structure and the antenna are plotted, as well as the antenna pattern comparison—with and without the drone—for the 3 principal planes.

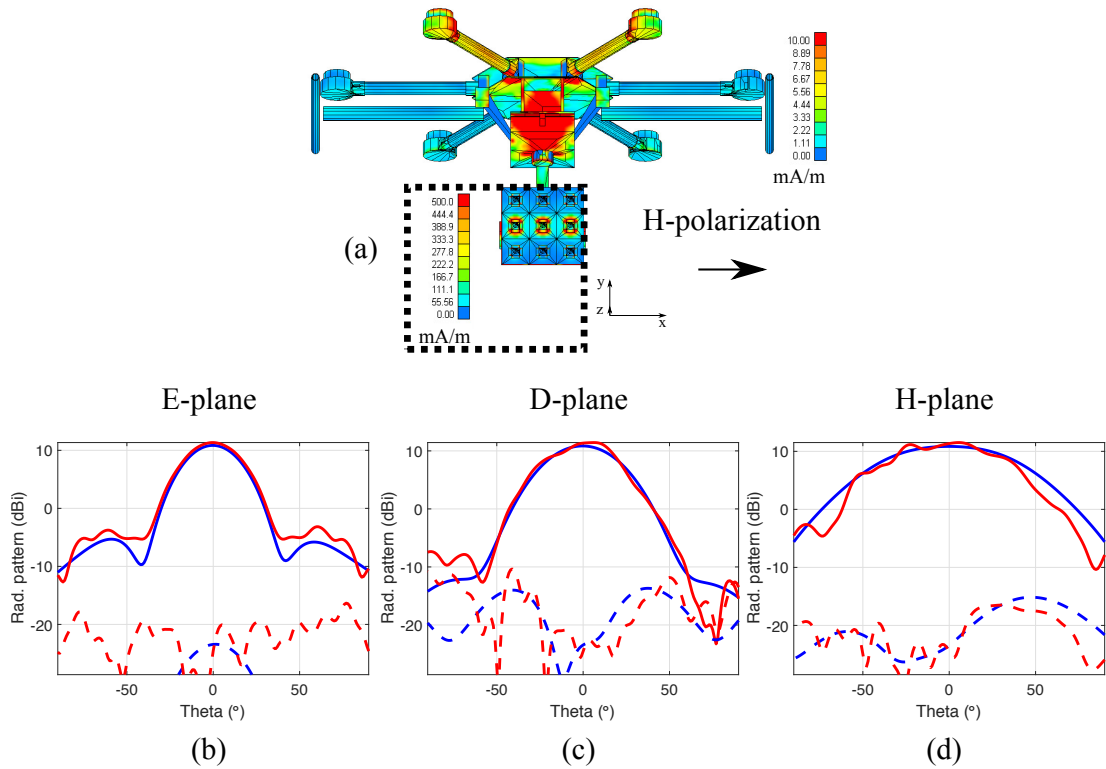


Figure 3.23: Effect of the UAV structure on the antenna pattern: central row of a  $3 \times 3$  S-Band single layer FR4 microstrip array, horizontally polarized. (a) Current density on the probe and the UAV structure. (b) E-Plane antenna patterns with and without the UAV (red and blue respectively). (c) D-Plane antenna patterns with and without the UAV (red and blue respectively). (d) H-Plane antenna patterns with and without the UAV (red and blue respectively).

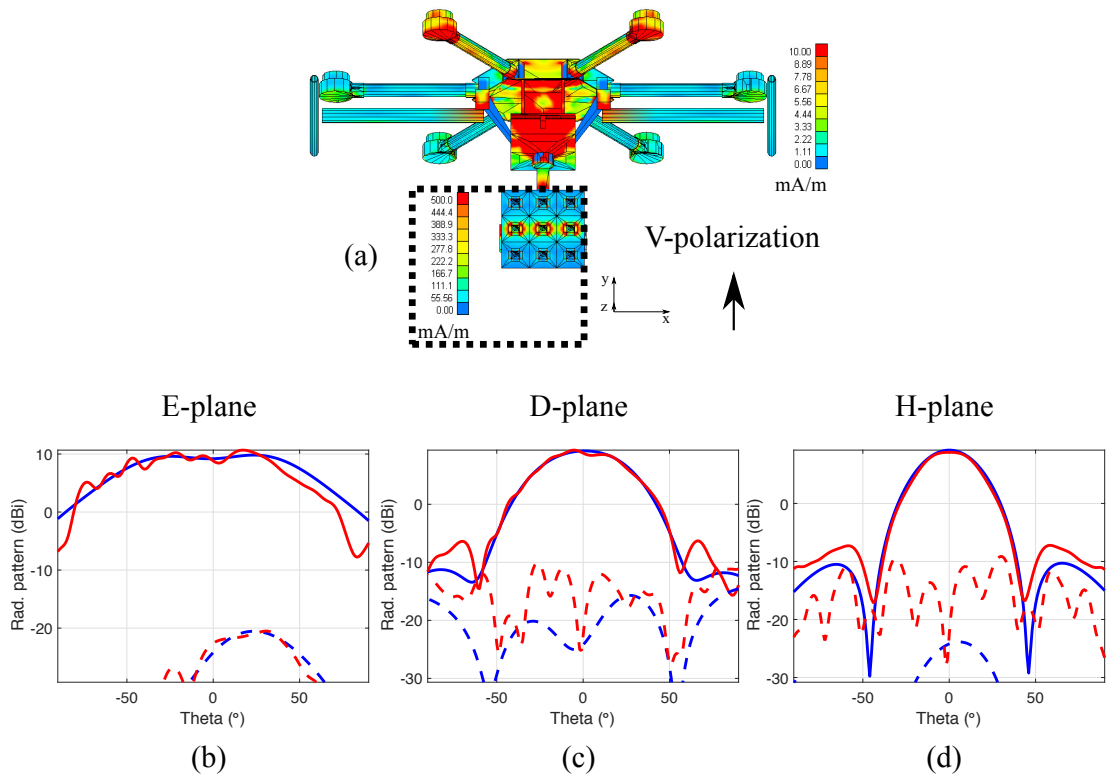


Figure 3.24: Effect of the UAV structure on the antenna pattern: central row of a  $3 \times 3$  S-Band single layer FR4 microstrip array, vertically polarized. (a) Current density on the probe and the UAV structure. (b) E-Plane antenna patterns with and without the UAV (red and blue respectively). (c) D-Plane antenna patterns with and without the UAV (red and blue respectively). (d) H-Plane antenna patterns with and without the UAV (red and blue respectively).

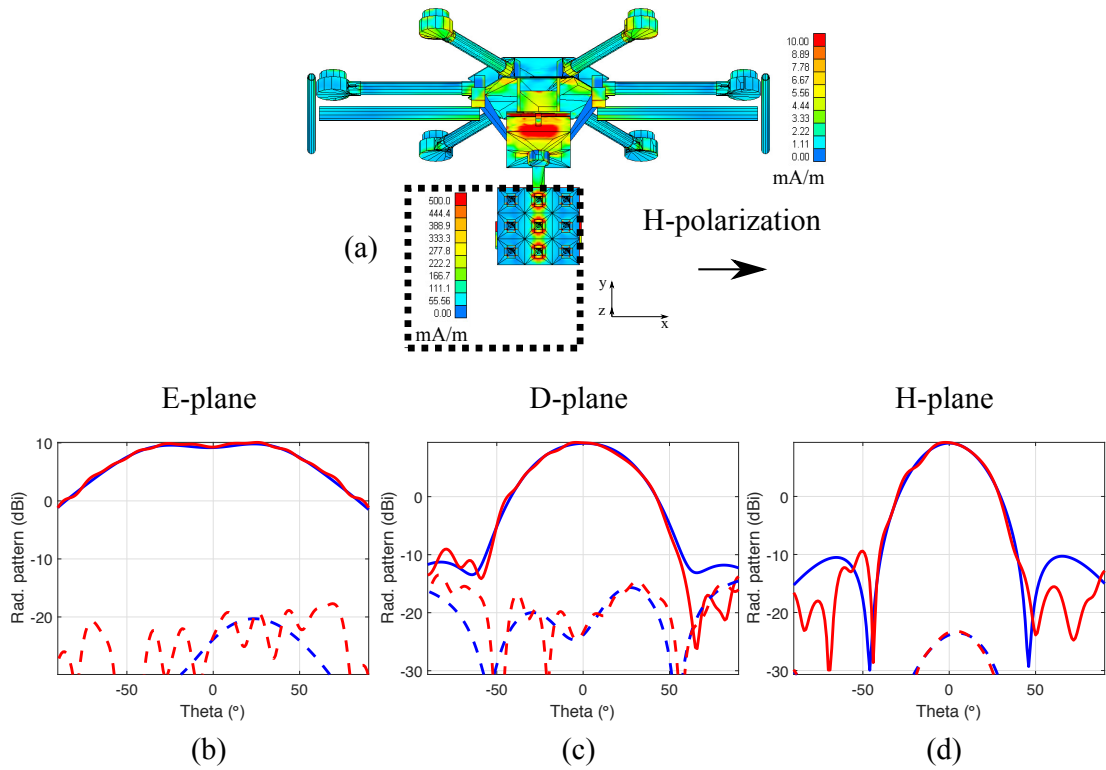


Figure 3.25: Effect of the UAV structure on the antenna pattern: central column of a  $3 \times 3$  S-Band single layer FR4 microstrip array, horizontally polarized. (a) Current density on the probe and the UAV structure. (b) E-Plane antenna patterns with and without the UAV (red and blue respectively). (c) D-Plane antenna patterns with and without the UAV (red and blue respectively). (d) H-Plane antenna patterns with and without the UAV (red and blue respectively).

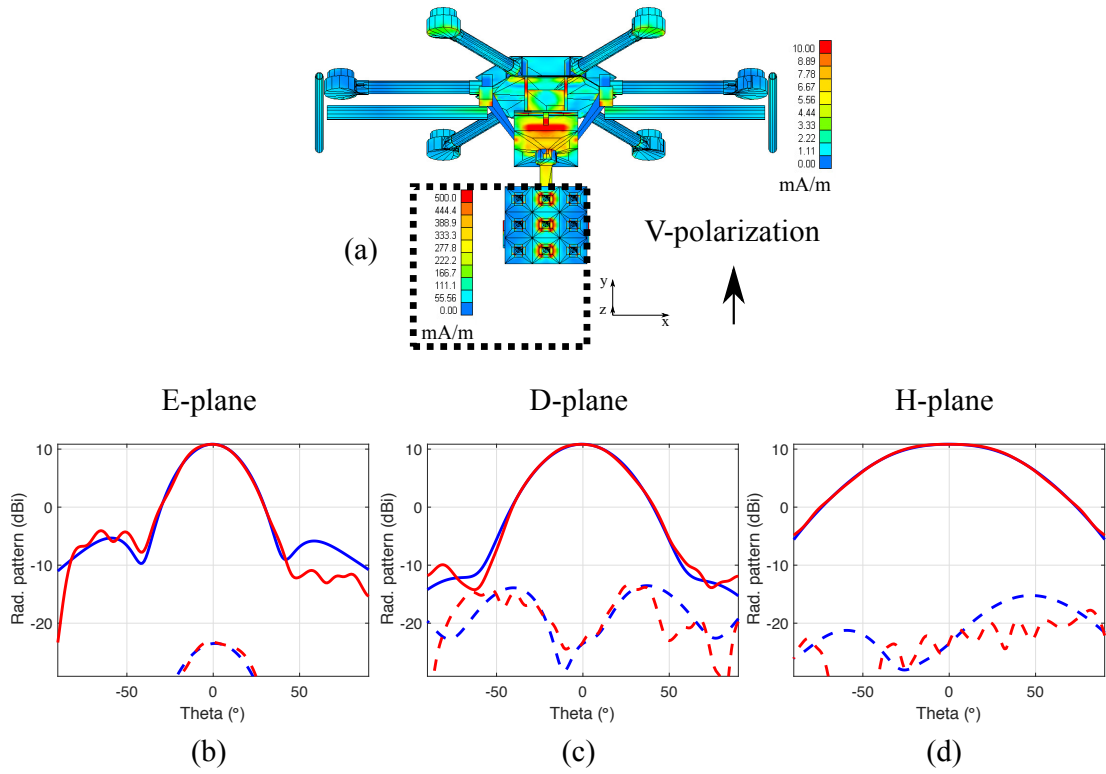


Figure 3.26: Effect of the UAV structure on the antenna pattern: central column of a  $3 \times 3$  S-Band single layer FR4 microstrip array, vertically polarized. (a) Current density on the probe and the UAV structure. (b) E-Plane antenna patterns with and without the UAV (red and blue respectively). (c) D-Plane antenna patterns with and without the UAV (red and blue respectively). (d) H-Plane antenna patterns with and without the UAV (red and blue respectively).

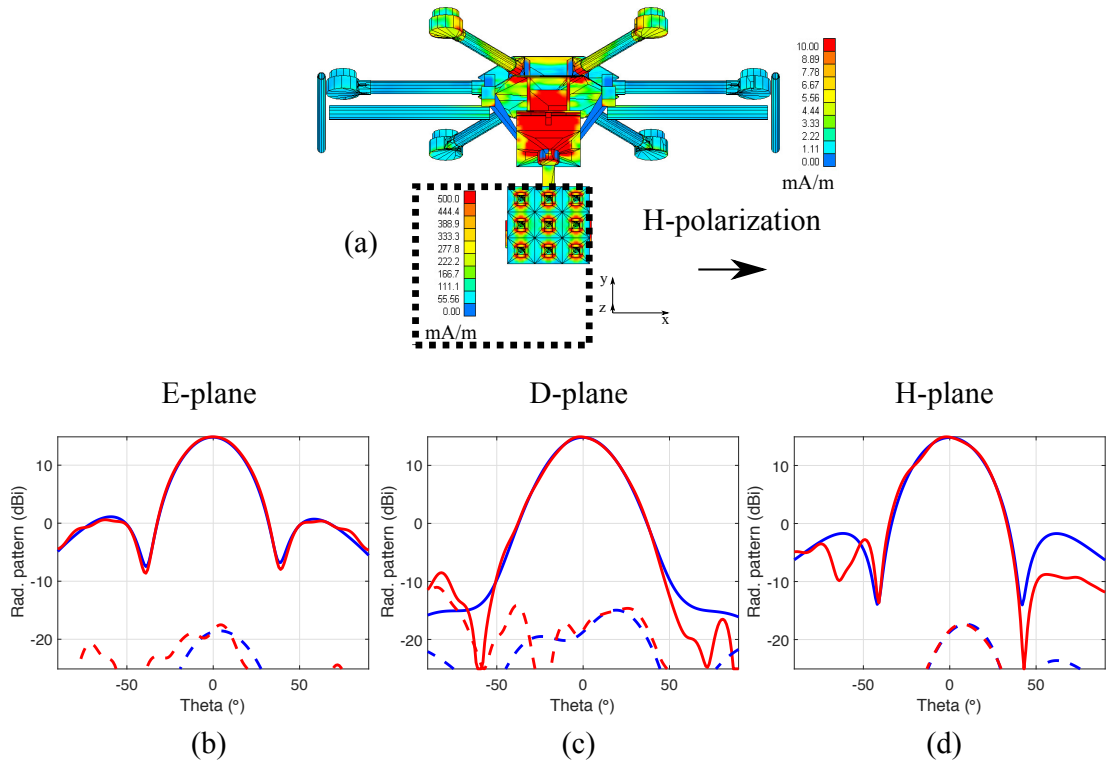


Figure 3.27: Effect of the UAV structure on the antenna pattern: all elements of a  $3 \times 3$  S-Band single layer FR4 microstrip array, horizontally polarized. (a) Current density on the probe and the UAV structure. (b) E-Plane antenna patterns with and without the UAV (red and blue respectively). (c) D-Plane antenna patterns with and without the UAV (red and blue respectively). (d) H-Plane antenna patterns with and without the UAV (red and blue respectively).

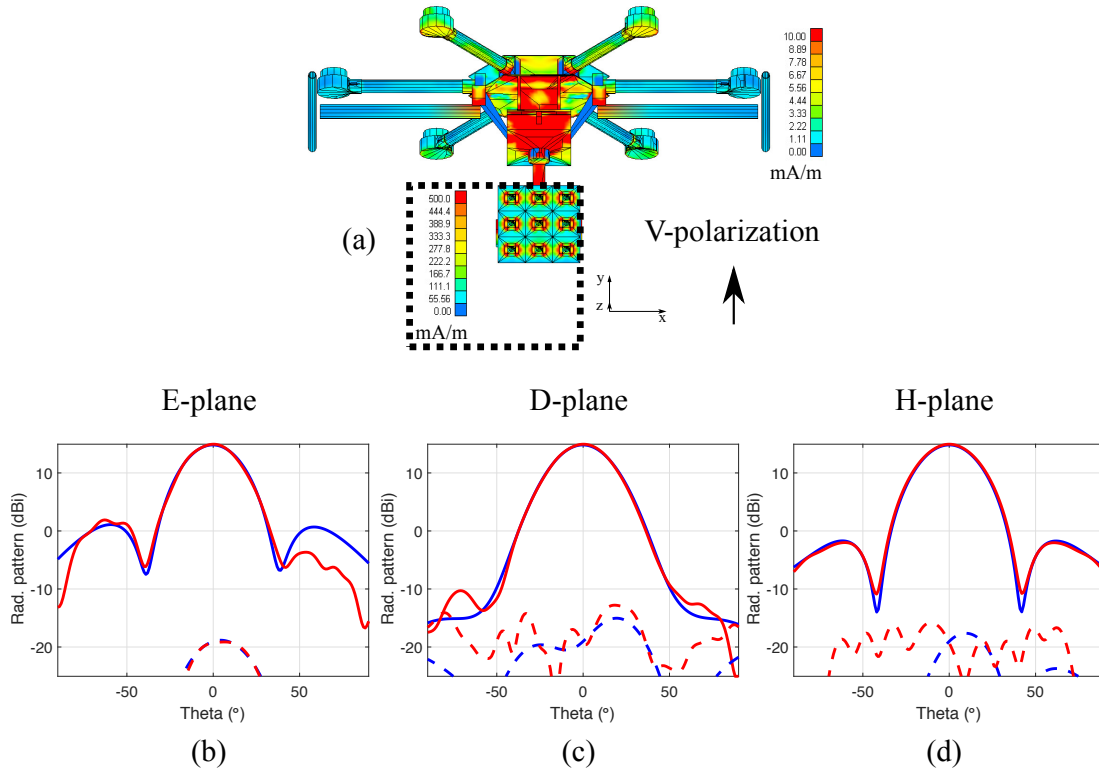


Figure 3.28: Effect of the UAV structure on the antenna pattern: all elements of a  $3 \times 3$  S-Band single layer FR4 microstrip array, vertically polarized. (a) Current density on the probe and the UAV structure. (b) E-Plane antenna patterns with and without the UAV (red and blue respectively). (c) D-Plane antenna patterns with and without the UAV (red and blue respectively). (d) H-Plane antenna patterns with and without the UAV (red and blue respectively).

The same general comments as in section 3.4.1 can be made. The row configuration results are shown on figures 3.23 and 3.24. The only adverse effects manifest through ripples in the H-plane for H-polarization and E-plane for V-polarization, obviously because these are the planes where the patterns are element patterns. The analogous column configuration results are shown in figure 3.25 and 3.26. Since, this time, the antenna is directive in the H-plane for H-polarization and E-plane for V-polarization, the effect on the antenna patterns is minimal. Lastly, when all elements are excited, in figures 3.27 and 3.28, the antenna is directive in all planes

and its pattern is minimally affected in all planes as a result. Table 3.6 sums up the ripple level for all the cases just presented.

In summary, the best configurations for this  $3 \times 3$  array are definitely the column and all the elements. The column even has an advantage over its counterpart, which is a broader pattern in the E-plane for H-polarization and H-plane for V-polarization, which gives more leniency to the positioning accuracy requirements. The problem for these configuration however, is to devise a performant power divider/combiner with low losses. This brings up the study of the  $2 \times 2$  array, as making a low-loss and balanced power divider/combiner to excite all elements is much easier in that case.

Table 3.6: Maximum oscillation level (dB), from  $-45$  to  $45^\circ$  for the antenna patterns of the  $3 \times 3$  S-Band single layer FR4 microstrip array mounted on the hexacooper

Excitation— Polarization	E-Plane	D-Plane	H-Plane
Central row—H	0	0	0.8
Central row—V	2.4	0.9	0
Central column—H	0	0	0
Central column—V	0	0	0
All elements—H	0	0	0
All elements—V	0	0	0

### 3.4.3 $2 \times 2$ Array

The  $2 \times 2$  configuration presents only one case for its analysis: all the elements excited. This is shown in 3.29 and 3.30.

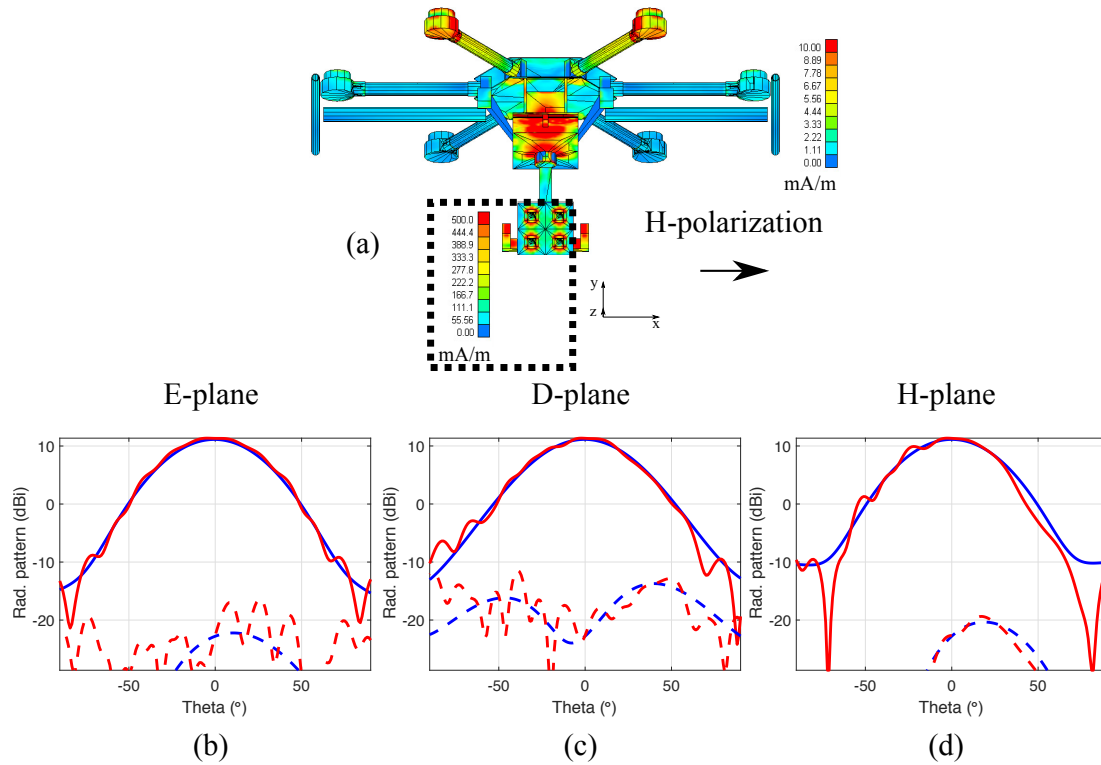


Figure 3.29: Effect of the UAV structure on the antenna pattern: all elements of a  $2 \times 2$  S-Band single layer FR4 microstrip array, horizontally polarized. (a) Current density on the probe and the UAV structure. (b) E-Plane antenna patterns with and without the UAV (red and blue respectively). (c) D-Plane antenna patterns with and without the UAV (red and blue respectively). (d) H-Plane antenna patterns with and without the UAV (red and blue respectively).

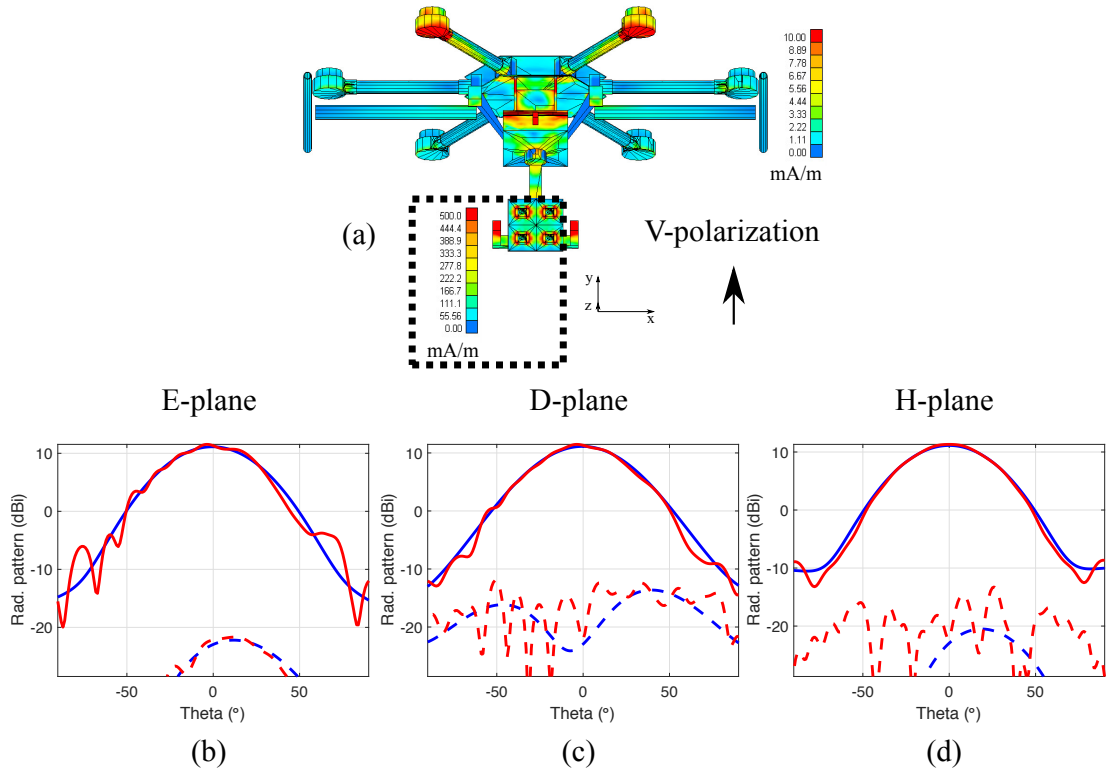


Figure 3.30: Effect of the UAV structure on the antenna pattern: all elements of a  $2 \times 2$  S-Band single layer FR4 microstrip array, vertically polarized. (a) Current density on the probe and the UAV structure. (b) E-Plane antenna patterns with and without the UAV (red and blue respectively). (c) D-Plane antenna patterns with and without the UAV (red and blue respectively). (d) H-Plane antenna patterns with and without the UAV (red and blue respectively).

A similar conclusion can be drawn as in section 3.4.1. Less directive than a  $3 \times 3$  configuration, the antenna patterns experience minor ripples, still more pronounced in the H-plane for H-polarization and E-plane for V-polarization. The cross-polarization levels have not risen to detrimental levels. Therefore this configuration seems to be the good balance between minor effects on the antenna patterns and directivity. The use of absorbing material on the sensitive areas of the UAV

structure could further limit its effect on the antenna patterns, making this configuration the most desirable. Table 3.7 sums up the ripple level on the antenna patterns for all cases.

Table 3.7: Maximum oscillation level (dB), from  $-45$  to  $45^\circ$  for the antenna patterns of the  $2 \times 2$  S-Band single layer FR4 microstrip array mounted on the hexacopter

Excitation— Polarization	E-Plane	D-Plane	H-Plane
All elements—H	0	0	0.3
All elements—V	0.8	0	0

### 3.5 Summary

In this section, scanning strategies for in situ antenna characterization with UAVs was presented. For each of these, equations were derived for the distance to be covered to measure a cut. They were illustrated for three relevant cases: WSR-88D, RaXPOL, and a 5G base station antenna. Unsurprisingly, the spherical scan is the most efficient in terms of mission distance, and therefore time. Then the emphasis was put on a thorough analysis of ground reflections, avoiding any approximation save for the path loss of both the incident and reflected paths. Considering the same 3 relevant cases, their effect on antenna pattern measurements was shown. It is seen that if the reflected ray is captured in the sidelobes of the AUT, the effect of ground reflections is greatly mitigated. Then, a thorough analysis was carried out about the effect on the UAV structure on the antenna patterns of the probe. Three platforms,

an in-house octocopter and hexcopter, as well as commercial DJI Phantom 3, were studied with the central embedded element of a dual-polarized  $3 \times 3$  array. Then the positioning accuracy of the critical components UAV was studied: for standard GPS, RTK GPS, IMUs, and gimbals. Particularly, the real advantage of the RTK GPS over the standard GPS was set forth, with an improvement of 2 orders of magnitude on the positioning accuracy. The effects of the UAV position and gimbal drifts on the measurements were formulated theoretically. The position drift effect was illustrated through the three relevant cases, and found to be significant for RaXPol and the 5G base station antenna. RTK or PPK can correct these errors in post-processing. The gimbal drift effect was found to be insignificant, if under  $1^\circ$ , regardless of the probe directivity. Finally, the focus was placed on the hexacopter with 3 more excitations of the same array: central row, central column, and all elements. Finally a study with the same hexacopter but with a  $2 \times 2$  version of the array, with all elements excited, was presented. It was found that the more directive the probe, the less its patterns are affected. Similarly the smaller the UAV structure, the less the patterns are affected.

# Chapter 4

## UAV Design

This chapter will start by looking at UAVs from a broad perspective, before narrowing down to the most suited type of platform for in situ antenna characterization. It will then look at the mechanical flying principles of the chosen UAV platform type, before looking at what components make up a UAV, and what each of their role is. Finally, the emphasis will be put on the design flow of such a UAV platform, what factors drive the choice of the different components, and in what order.

### 4.1 Classification

UAVs exist in different categories, each with their own set of advantages and disadvantages over the others. This section aims at listing each category briefly, and determining which one is best suited for the system studied in this thesis. The two main categories are lighter-than-air and heavier-than-air UAVs. What these names truly reflect is the density of the aircraft with respect to that of air, i.e. if the overall density of the aircraft is less than that of air, it is a lighter-than-air aircraft, otherwise it is a heavier-than-air aircraft. Then each of these two categories can further be divided up into two more self-explanatory categories: motorized and non-motorized aircrafts. The most common UAVs found in each category are summed up in 4.1.

Table 4.1: UAV classification

	Motorized	Non motorized
Lighter than air	Blimp	Balloon
Heavier than air	Airplane and rotorcraft	Glider

Balloons come in two forms: hot air balloons as well as gas balloons. The former relies on inflating the balloons with hot air, which has a lower density than the surrounding air, while the latter relies on the use of gases that have lower densities than air. Hot air balloons are the most common as they do not require the use of expensive gases, such as helium. Balloons can only act on their altitude, by inflating or deflating the balloon. They are carried by the winds to fly in different directions. Blimps are very similar in the way they operate: they carry a big balloon where a gas less dense than air resides, this balloon is fixed on top of a gondola carrying motors that enable the aircraft to control its course on top of its altitude. Even though the mechanism that allows blimps and balloons to fly is relatively simple, it means that they are slow and hard to control.

Airplanes get the necessary lift to fly from one or several jet engines or propellers, that are on the wings or at the front end of the fuselage. Airplanes have good flight autonomy and speed, but are limited in slow and precise maneuvering, and cannot hover. Gliders are similar to airplanes, but do not have an engine to propel themselves. Finally, rotorcrafts are aircrafts that rely on one or several rotor blades to get vertical thrust and fly. Tilting rotor blades or adjusting the speed of one or several of them with respect to the other ones is what permits the aircraft to move

in a different direction. Table 4.2, developed in [40], gives an excellent comparison of airplanes, rotorcrafts, and blimps for a number of relevant factors, taking into account the miniaturization of the aircraft. Balloons were excluded because of their incapacity to control their flight, and therefore their unsuitability for this thesis' application.

Table 4.2: UAV comparison focused on miniaturization  
(1 = bad, 3 = good)

	Airplane	Rotorcraft	Blimp
Power cost	2	1	3
Control cost	2	1	3
Payload/volume	3	2	1
Maneuverability	2	3	1
Degrees Of Freedom	1	3	1
Stationary flights	1	3	3
Low-speed flights	1	3	3
Vulnerability	2	2	2
Vertical Takeoff/Landing	1	3	3
Endurance	2	1	3
Miniaturization	2	3	1
Usage	1	3	2

Of course, measuring antennas with an aircraft will require stationary and low-speed flights, maneuverability, as well as a payload of a few pounds. From table 4.2,

it can be seen that rotorcrafts are the best candidate for this application. Multi-rotors, which belong to the category of rotorcrafts, have become cheap and easy to make in the recent years. Consequently, they are considered the platform of choice from now on, and will be studied in the remainder of this chapter.



Figure 4.1: The arrangement used for the dynamical model of the quadcopter, illustrated on a DJI Phantom UAV.

## 4.2 Model and Components

### 4.2.1 Dynamics

Before moving onto the design rules of UAV multirotors, their dynamics shall be presented briefly so the reader can get an insight of how these platforms fly and are controlled. The author already studied and reported the modeling and control of multirotors, in [41]. All the derivations can be found therein. The modeling can also be found in [40]. The dynamical model of a quadrotor UAV is presented below, according to the arrangement shown in figure 4.1, [42]. It should be noted that the dynamics do not change for 6 or 8 rotors, hexacopter and octocopter respectively, these configurations just add redundancy to the platform.

$$\begin{bmatrix} \ddot{x} \\ \ddot{y} \\ \ddot{z} \end{bmatrix} = \begin{bmatrix} \frac{U1}{m} (c\psi s\theta c\phi + s\psi s\phi) \\ \frac{U1}{m} (s\psi s\theta c\phi - c\psi s\phi) \\ -g + \frac{U1}{m} (c\theta c\phi) \end{bmatrix} \quad (4.1)$$

$$\begin{bmatrix} \ddot{\phi} \\ \ddot{\theta} \\ \ddot{\psi} \end{bmatrix} = \begin{bmatrix} \frac{1}{I_x}[lU2 + (I_y - I_z)\dot{\theta}\dot{\psi} - \dot{\theta}\sum_{i=1}^4 -1^i J_r \Omega_i] \\ \frac{1}{I_y}[lU3 + (I_z - I_x)\dot{\phi}\dot{\psi} + \dot{\phi}\sum_{i=1}^4 -1^i J_r \Omega_i] \\ \frac{1}{I_z}[U4 + (I_x - I_y)\dot{\phi}\dot{\theta}] \end{bmatrix} \quad (4.2)$$

$$\begin{aligned}
U1 &= \sum_{i=1}^4 b\Omega_i^2; \\
U2 &= b(\Omega_4^2 - \Omega_2^2); \\
U3 &= b(\Omega_3^2 - \Omega_1^2); \\
U4 &= \sum_{i=1}^4 -1^i d\Omega_i^2,
\end{aligned} \tag{4.3}$$

where  $U1$ —thrust input—,  $U2$ —pitch input—,  $U3$ —roll input—, and  $U4$ —yaw input—are the control inputs;  $x$ ,  $y$ , and  $z$  represent the position of the UAV in space;  $\phi$ ,  $\theta$ , and  $\psi$  represent the attitude angles about each axis respectively;  $m$  is the mass of the UAV;  $g$  is the gravitational constant;  $l$  is the arm length;  $I_x$ ,  $I_y$ , and  $I_z$  are the inertia parameters of the UAV about each axis respectively;  $b$  is the thrust factor;  $d$  is the drag factor;  $J_r$  is the rotors inertia; and  $\Omega_i$  denotes the speed of the  $i^{th}$  rotor.

From equations 4.1 through 4.3 it follows that:

- The dynamics of the UAV are highly nonlinear and coupled.
- Moving in altitude ( $z$ ) is accomplished by changing the thrust  $U1$ , while moving horizontally (in  $x$  and  $y$ ) relies on the attitude of the copter—pitch and roll—as well as the thrust. More precisely, the thrust is the vertical force—along  $z$ — produced by all rotors and proportional to the square of their speeds.
- The roll and pitch angles depend on the speed difference of opposite rotors ( $U2$  and  $U3$ )—this is called vectoring the thrust, while the yaw angle depend on the countertorque of each rotor with respect to its successive neighbor ( $U4$ ).

Therefore controlling a multirotor is a challenge, more complicated than standard linear control techniques. A good option is adaptive control, which tunes itself while the flight is being performed, to, like the name suggests, adapt to its changing environment. This technique is set forth in [41], [43].

## 4.2.2 Block Diagram

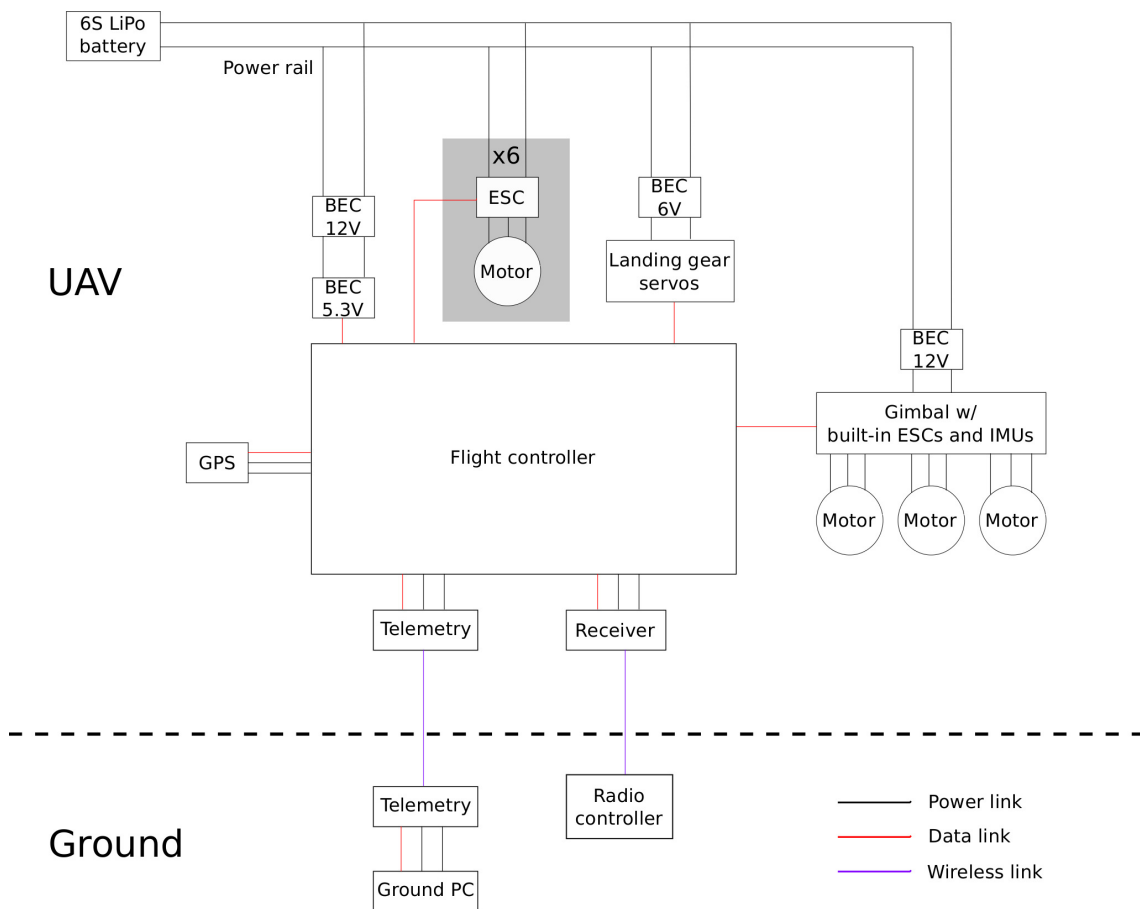


Figure 4.2: The block diagram of the in-house hexacopter at the ARRC.

Before moving on to the design process of the UAV, it is a good idea to analyze a typical UAV block diagram. Such a diagram is presented in figure 4.2, for the in-house ARRC hexacopter. The real platform, along each element from the

block diagram, save for the Electronic Speed Controllers (ESC), are shown in figure 4.3. The part list is available in section A, table A.1. The heart of a UAV is the flight controller, it is the system that gathers data from and communicates with the different components of the UAV to ensure that it carries out the given mission, or flies according to the Radio Controller (RC) inputs. The flight controller is supplied power from one battery, and through two Battery Elimination Circuits (BEC) that lower the voltage to the right level. Motors—and propellers attached to them—give the platform its thrust and capacity to move in the air, while ESCs send the proper signals to them according to the flight controller’s orders. Similarly the retractable landing gear is actuated by two servomotors. The gimbal, on which the antenna is mounted, is actuated by 3 motors—for roll, pitch and yaw. Similarly to the flight controller, the landing gear servos, and the gimbal are powered by the batteries through BECs. Other accessories are connected to the flight controllers: a GPS module that estimates the position of the UAV from satellite constellations, a receiver module that receives orders from the RC, and a telemetry module used to relay information to the ground station through its own telemetry module.

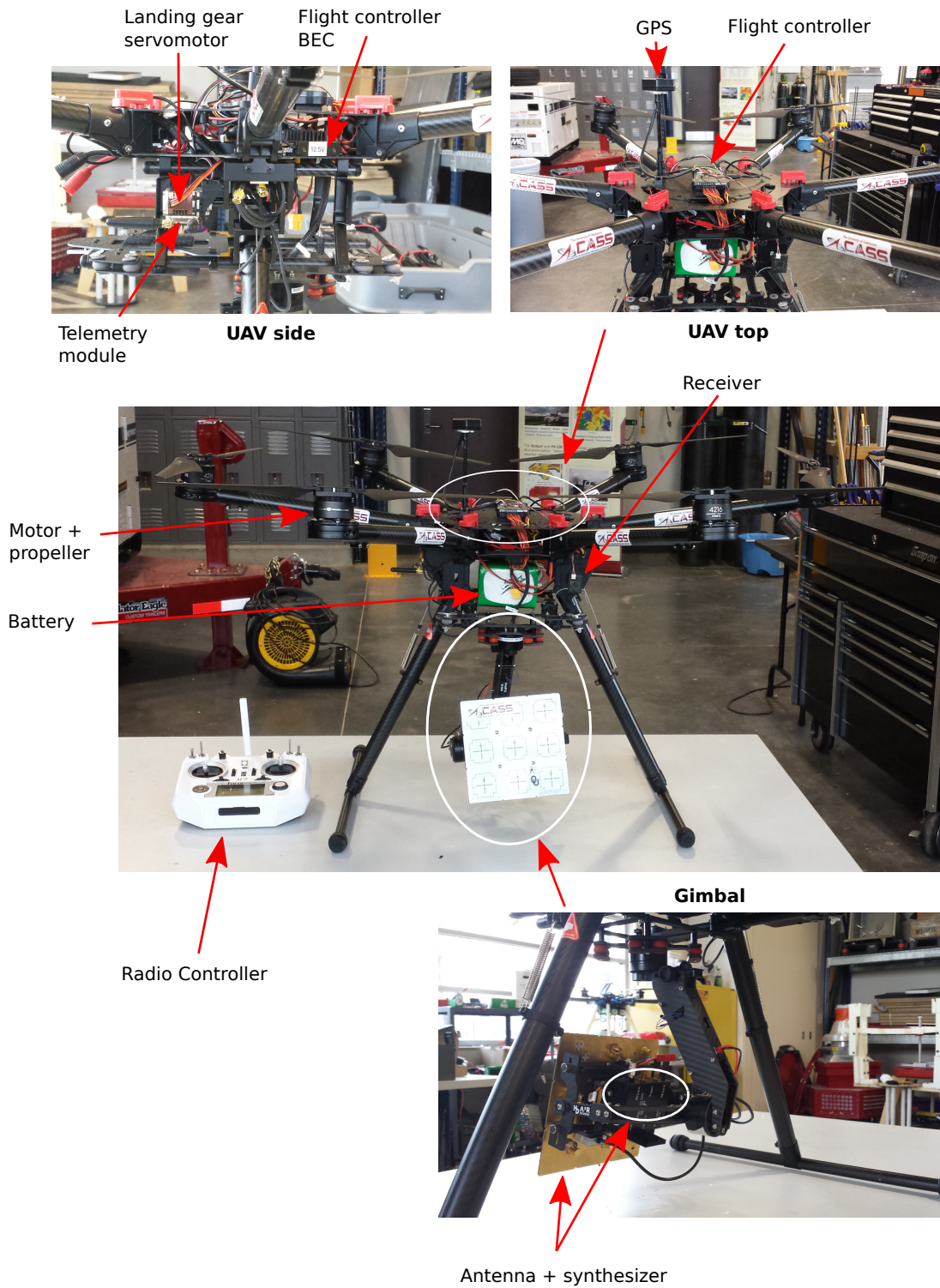


Figure 4.3: The in-house hexacopter platform with its components shown.

## 4.3 Design

### 4.3.1 Frame and gimbal

The first step in the design is to choose a frame type. The most common frame types, along their advantages and drawbacks, are, [44]:

- The bicopter—2 rotors. This design was used at the beginning of the commercial UAV era, when components were not as diverse and easy to find. It is a rather unstable design that's hard to control.
- The tricopter—3 rotors. This design was also used substantially at the beginning of the commercial UAV era, for the same reasons. It can be optimized for small sizes, but is not suited for bigger sizes and payloads.
- The quadcopter—4 rotors. The quadcopter is undeniably the most popular structure in the multirotor world. As the dynamical model shows, it is the simplest structure that allows the UAV to move by just changing the speed of the motors. The main drawback of the quadrotor is that it lacks redundancy, which means that if a motor fails it will most likely end up in the platform crashing.
- The hexacopter and octocopter—6 and 8 rotors respectively. Contrary to the quadrotor, these platforms are redundant and can keep flying and land safely if a motor fails. Since they have more motors, they also have more thrust, therefore permitting the hauling of higher payloads, which is useful for photography and video applications. The reduction in propeller size however, since there is less spacing between motors, means that the endurance will be

lesser. Lastly, these platforms have an increased complexity which can make them more prone to failures.

In the case of the system presented herein, the quadcopter or the hexacopter seem to be the best alternatives. The redundancy as well as the higher payload capacity offered by the hexacopter however, looks like the best approach out of the two. Within the quadcopter and the hexacopter, there are two popular frames, shown in figures 4.4 and 4.5: the + frame and the X frame. The dynamics and characteristics remain the same, regardless which one is used. Once the frame type

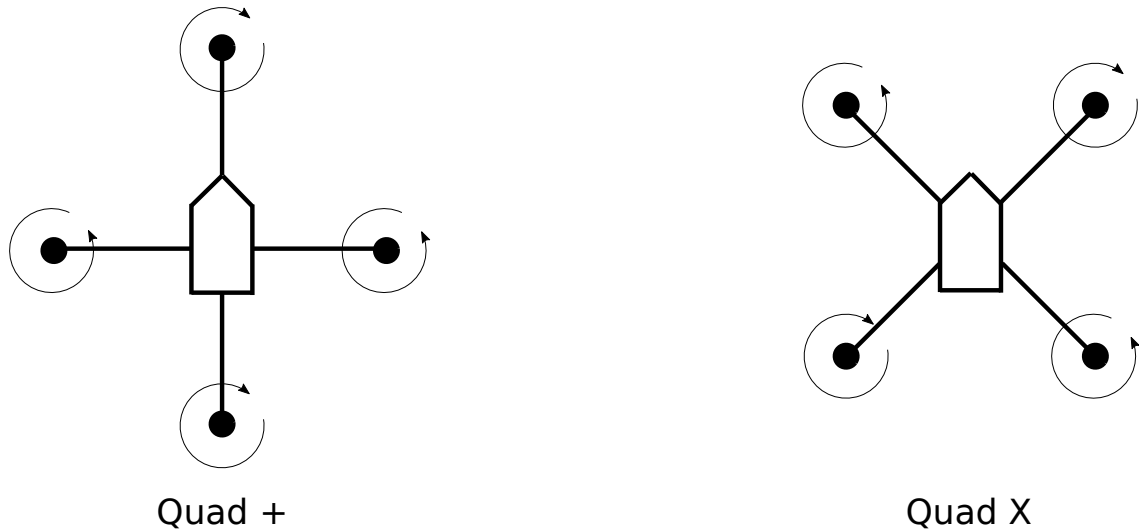


Figure 4.4: The two most popular frame types for the quadcopter: + and X frames. The direction of rotation for each motor is also indicated—Clockwise (CW) and Counter-Clockwise (CCW).

has been chosen, the size is another factor. The size of the frame will dictate how big the propellers can be. As will be seen in the next paragraph, bigger propellers are better for the system presented in this thesis. Therefore, a big frame is preferable. For the in-house hexacopter at the ARRC, the DJI S900 frame was chosen, which can accommodate 18-inch propellers.

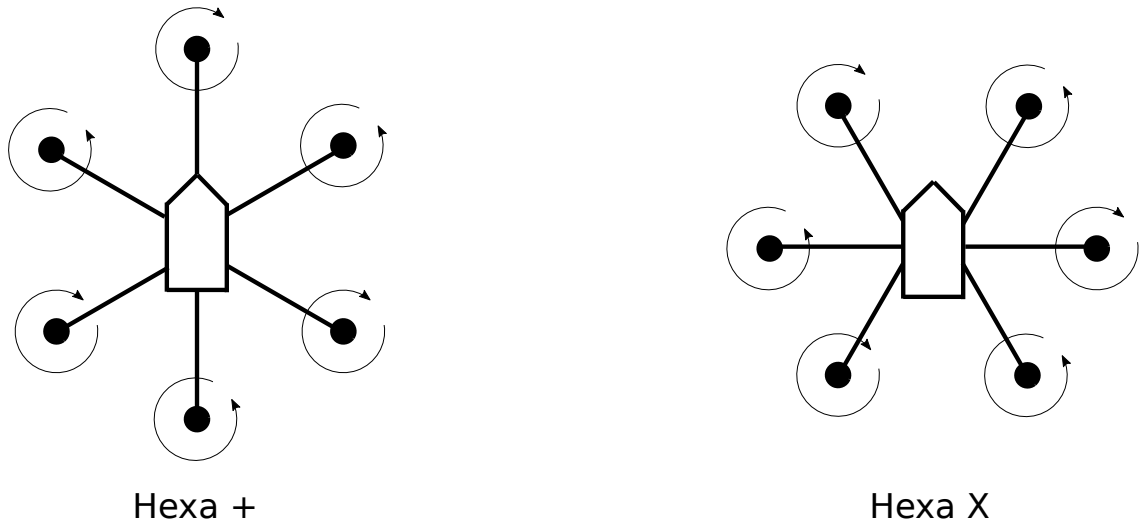


Figure 4.5: The two most popular frame types for the hexacopter: + and X frames. The direction of rotation for each motor is also indicated—Clockwise(CW) and Counter-Clockwise (CCW).

The gimbal is chosen according to three factors, its dimensions—so that there is enough clearance under the UAV to mount it, its payload capacity, and its weight. Since gimbals are used to mount cameras for video applications that do not have stringent positioning requirements, their positioning accuracy is not a consistent sales argument. The one used on the in-house ARRC hexacopter is the Infinity MR S2, which weighs 560 g, and can carry payloads up to 900 g. The payload capacity is deemed to be sufficient for carrying a single layer patch antenna array, alongside its integrated power divider/combiner and synthesizer.

### 4.3.2 Propulsion Systems

The propulsion system includes the motors, propellers, and ESCs. Assuming the frame has already been chosen The design flow for this stage is as follows:

- Determine the total weight of the UAV as closely as possible. This will determine the necessary thrust.
- Choose the propeller size according to the needs of the application and the frame size.
- Choose the motor with the efficiency and thrust required by the application. It also needs to match the chosen type of propeller.
- Choose the ESC that matches the motor.

Even if not all the components have been chosen, the total weight of the multi-copter needs to be evaluated. It dictates how much power will be needed to get the platform off the ground, fly at a reasonable speed, and be responsive enough. No golden rule exists but the most common one is, [45]:

$$T = 2W, \tag{4.4}$$

where  $T$  is the total thrust of the UAV, in kg, and  $W$  is the total weight in the UAV, in kg. It essentially means that 50% throttle is needed to hover the copter, while the remaining 50% is used to actually move. If the case of the hexacopter is taken, let us assume we are using the part list from table A.1, except for the propulsion system that we have to determine in this section. One of the most popular manufacturers of motors and propellers for UAV applications is T-Motor, and for 18×6.1 propellers they recommend the U7-KV420 motors. This will be used in this estimate. Table 4.3 sums up the weight of the copter, and of its different components. The total weight comes up to 7.26 kg.

Table 4.3: Weight estimate of the ARRC in-house hexacopter

Part	Weight (kg)
Frame	1.20
Motor and propeller	$0.35 \times 6$
Gimbal	0.56
Battery	2.4
Payload	0.50
Others	0.50
Total	7.26

Propellers have two characteristics: their diameter, and their pitch. The pitch is how far, in translation, the propeller moves for one complete revolution. As for the diameter, bigger propellers mean less thrust but more efficiency, whereas smaller propellers mean more thrust but less efficiency, [46]. Efficiency is defined as:

$$E = \frac{T}{W}, \quad (4.5)$$

where  $E$  is the efficiency,  $T$  is the thrust and  $W$  is the power delivered by the motor. The flight time will increase with the propeller size, whereas the speed and acceleration will decrease with propeller size. In the case of the system presented in this thesis, flight time is very important while speed and acceleration are not critical. Therefore, the propellers should be chosen to be as big as possible. As far as the pitch is concerned, higher pitch means that the speed and acceleration will grow,

while the efficiency will decrease, [46]. Consequently, lower pitch is required for our purpose. In the case of the hexacopter, the frame can accommodate propellers as large as 18 inches, which is the size that should be chosen for maximizing efficiency, and therefore flight time.

Now that the propellers have been chosen, the motors can be picked out. The most popular motors for UAVs are 3-phase brushless motors. As was previously mentioned, not any given motor is capable of spinning any propeller size. One of the motor's most important figures of merit is the KV rating. It is merely a number that describes, for a single Volt increase at the motor terminals, the increase of its speed in rpm. Typically, a motor with a lower KV rating spins more slowly, and spins larger propellers, whereas a motor with a higher KV rating spins faster, and spins smaller propellers. Unfortunately, there is not an available reference chart that links KV rating and propeller size, but manufacturers typically specify what propellers a given motor can spin. The efficiency, as defined in equation 4.5 is also an important factor, as it greatly influences the flight time. Furthermore, the thrust is also crucial because it determines how much flying power the drone will have, and the current draw is important to consider to see if the battery can provide enough current to all motors at the same time as well as the other UAV components. In the case of the propulsion system used for the estimate, it has a KV rating of 470, develops a maximum thrust of 3.3 kg per motor, with 6.71 efficiency and 20.5 A drawn. Therefore, 19.8 kg of thrust are available which largely satisfies equation 4.4. For the hexacopter the DJI E1200 Pro propulsion system was retained, as it includes 310-KV motors,  $17 \times 6$  propellers, and ESCs, and it is especially suited for

the DJI S900 frame. 3.9 kg of thrust is developed by each motor, which adds up to a total thrust of 23.4 kg. This is even better as the propulsion system used for the estimate. Moreover, the weight of propulsion system set is 345 grams, which is almost identical to what was used during the estimate.

The last step is to choose the ESCs. The important thing to consider is the current rating of the ESC, [47]. It needs to be at least as much as the maximum current draw of the chosen motor. There are some secondary aspects when choosing ESCs. First, ESCs are sold in single units or units including several ESCs. While the latter might seem nice, it should be kept in mind that if only one ESC is broken, the entire unit might have to be replaced. Then, there are 2 different reliable firmwares on the market for ESCs: SimonK and BLHeli. While no performance difference is noticeable between the two, BLHeli does offer a user-friendly interface to communicate with its ESCs during the calibration process. For the hexacopter, the ESCs are part of the propulsion system.

## 4.4 Other components

The most important components of the design have now been determined. There still remains:

- The flight controller.
- The GPS.
- The telemetry module.
- The RC and its receiver.

- The battery.

Unlike previously, there really is not any set of rules for choosing these components. What drives the choice of these components is mainly the price, as well as consumer reports.

One of the most common choices in the UAV community concerning the flight controller is the Pixhawk. Indeed, it is very cheap, open-source, can be interfaced with the majority of UAV components on the market, is compatible with most multicopter platforms, and has great reviews. It can be purchased in a bundle with a standard GPS receiver and 3DR telemetry radios for less than \$200. The RC is chosen based off of its ease of use, and number of channels available. The Spektrum DX9, delivered with its receiver the DSMX, was retained for the in-house hexacopter. Finally, the battery needs to be chosen. The first criterion is to have a voltage that matches that of the motors, which have the highest voltage requirement. The voltage depends on the material used in the battery and the number of cells. For instance, a 3S—3 cells—Lithium Polymer (LiPo) battery would be 11.1V since a LiPo cell is 3.7V. When it is charged it would be 12.6V since a charged LiPo cell is 4.2V. The capacity of the battery is an important parameter given in mAh. It represents the energy stored in the battery and determines the flight time of the UAV. There is the constant discharge constant that represents how much current can be drawn continuously from the battery. A constant discharge of 5C with a 2000 mAh battery would indicate that the battery can supply up to 10 A. The peak discharge represents how much current the battery can supply, but only over very short periods of time. A peak discharge of 10C with a 2000 mAh battery means that

20 A can be drawn from the battery for the amount of time that the manufacturer indicates. The Multistar LiPo 20000 mAh 6S 10C was the chosen battery for the in-house hexacopter.

## 4.5 Summary

In this section, UAVs were classified in four different groups. Following is an evaluation of 3 different types of aircraft—plane, blimp, and multirotor. It was concluded that multirotors, belonging to the heavier than air and motorized aircraft category, were the best suited thanks to its ease of use, maneuverability, low-speed and stationary flight capabilities, and payload capacity. The dynamics of the multirotor were presented and prove to be a challenge in terms of control. The block diagram of a typical multirotor was presented through the in-house ARRC hexacopter, and illustrated with pictures. Finally the design flow of a UAV was set forth. The frame is chosen first, as it determines the propeller size—important for efficiency and therefore flight time—, flight redundancy through the number of arms, and how big the gimbal can be. The latter is then chosen according to its dimensions and payload capacity. Once the weight estimate of the platform was established, and the propeller size chosen—which is limited by the frame size—, the motors were specified and ESCs matching their maximum current draw were chosen. Finally, the rest of the components were selected.

# Chapter 5

## Preliminary Results

Presented in this chapter are preliminary results of in situ antenna characterization tests using a UAV (DJI Phantom 3). The tests were performed both in an indoor antenna range facility and outdoors, in December 2015 and January 2016. The radiation pattern in one cut was measured:  $0^\circ$  elevation in azimuth, in V-polarization. To check the consistency of the measurement, two setup were implemented, as is shown in figure 5.1, by flying around the antenna in a circle, a), and by hovering while the antenna spins on itself, b). The setup will be presented, as well as the modeling of the probe on the UAV, and results both indoors and outdoors.

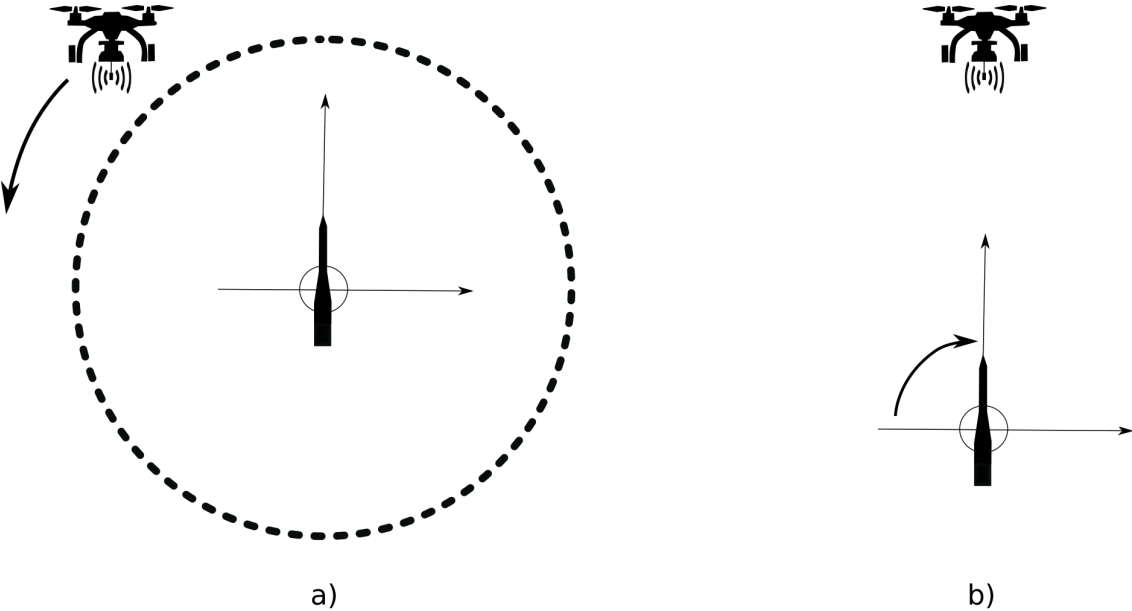


Figure 5.1: Top view of the scanning modes for the testings. a) The UAV flies around the AUT in a circle at 0-degree elevation. b) The UAV hovers in front of the AUT at 0-degree elevation while it spins on its turntable.

## 5.1 Setup

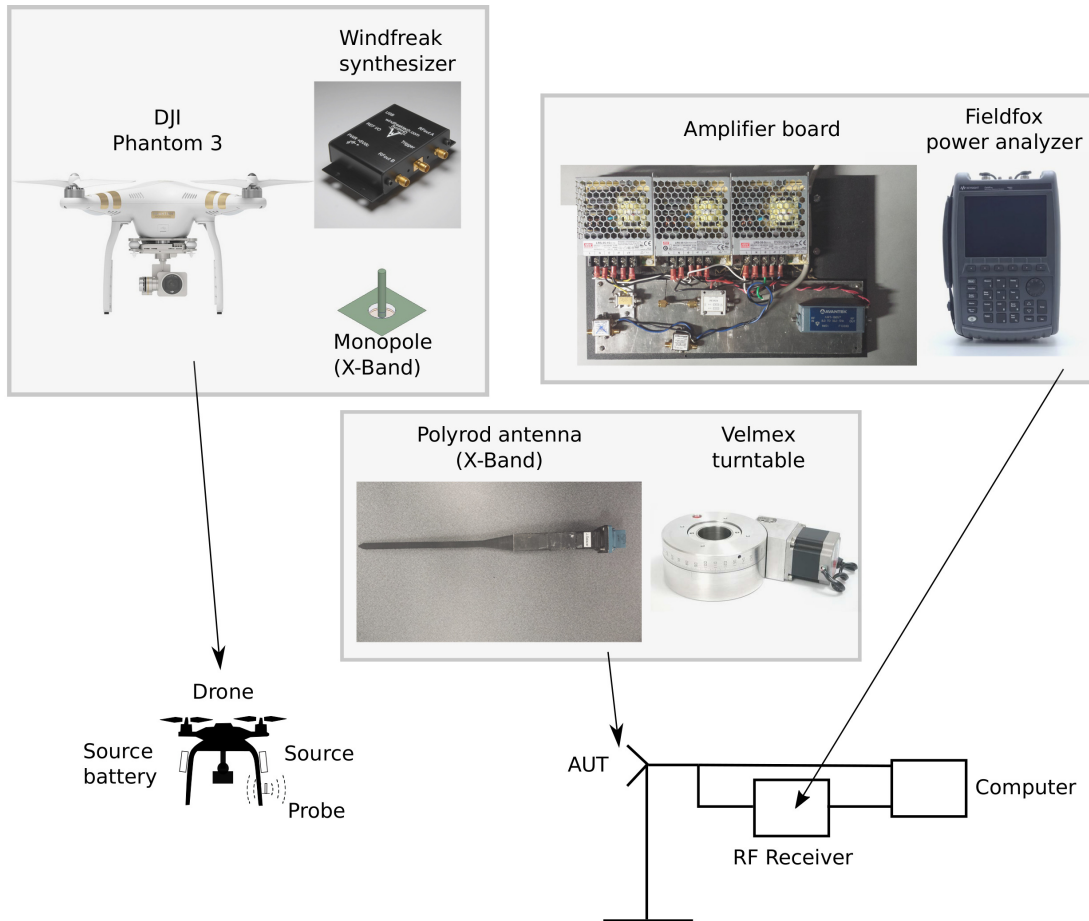


Figure 5.2: The setup used for the preliminary measurements. A DJI Phantom 3 was equipped with an X-Band monopole, fed by a Windfreak synthesizer. The AUT is an X-Band polyrod antenna, placed on a Velmex turntable, hooked up to an RF receiver, which is composed of an amplifier board and a Fieldfox power analyzer. The turntable and the power analyzer are controlled by the computer.

Figure 5.2 shows the setup. An X-band AUT was tested using a small monopole antenna (probe) attached to the frame of the UAV, since its gimbal cannot support any other additional payload than the mounted camera. An extra battery package was used to excite the RF synthesizer to transmit 24 dBm at 9.8 GHz. On the AUT side, a customized surface wave antenna is connected to an RF receiver, composed of a Low-Noise Amplifier(LNA) and amplifiers and a power spectrum analyzer, to

compensate for losses in the air and cables. The AUT rotates on a turntable in azimuth, which means the 0-degree elevation angle azimuthal cut of the radiation pattern is measured. The measurement procedure is fully automated by a LabVIEW program that controls the turntable as well as the power spectrum analyzer.

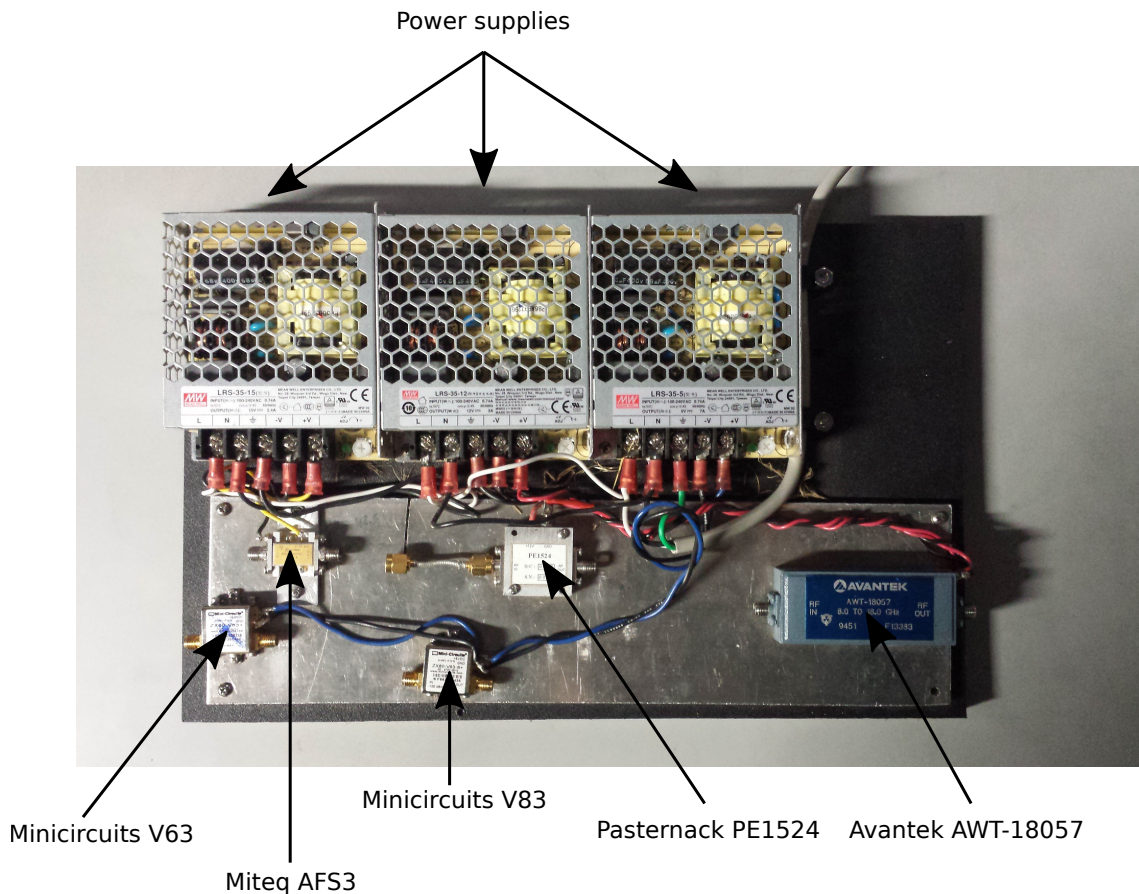


Figure 5.3: The amplifier board and its 5 amplifiers.

The amplifiers as well as the RF cables were characterized. The amplifier board comprises 5 amplifiers, as represented on figure 5.3:

- Pasternack PE1524 (LNA) from 2 to 18 GHz.
- Minicircuits V63 and V83, from 0.05 to 6 GHz and 0.020 to 4.7 GHz respectively.
- Avantek AWT-18057 from 8 to 18 GHz.

- Miteq AFS3 from 2 to 4 GHz.

Since the range of frequencies of interest for the testings at the ARRC range from S-Band to the bottom of X-Band, they amplifiers were characterized within the part of their operational range between 2 and 10 GHz with a Vector Network Analyzer (VNA). The transmission coefficient ( $S_{21}$ ) was measured, which represents their gain. These results are shown on figure 5.4.

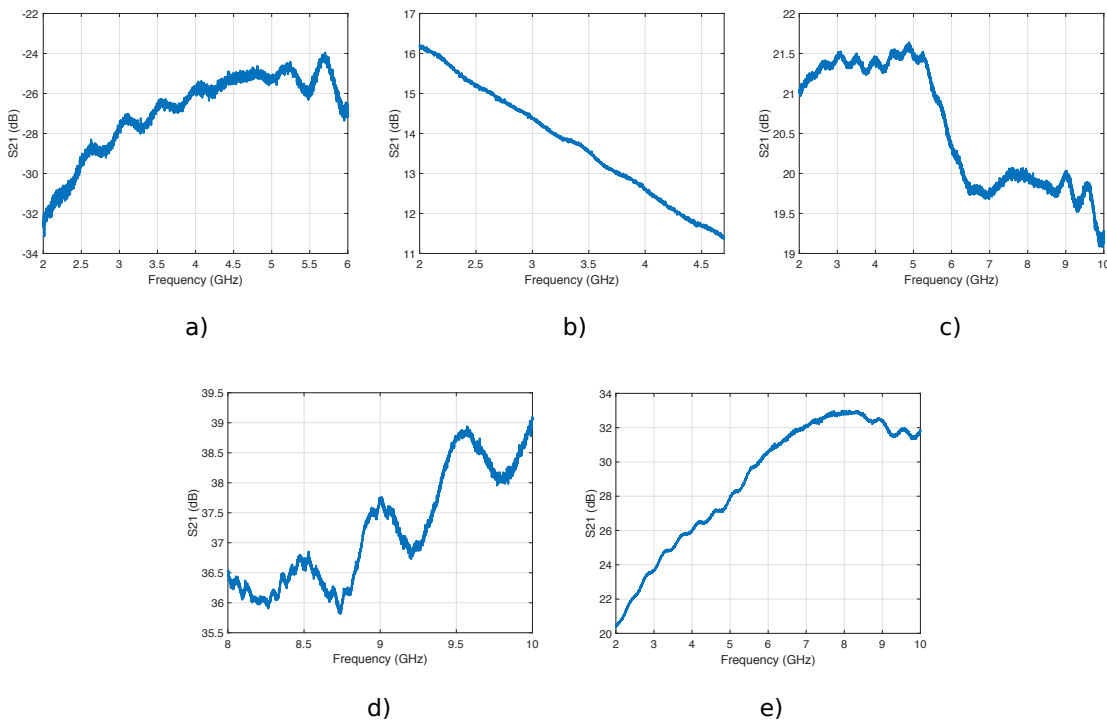


Figure 5.4: The gain for each amplifier in the frequency range of interest. a) Mini-circuits V63, b) Minicircuits V83, c) Pasernack PE1524, d) Avantek AWT-18057, and e) Miteq AFS3.

Two RF cables were used: one 33-foot cable between the AUT and the amplifier board, and a 6-foot one between the amplifier board and the power analyzer. The losses were characterized for both of these cables, which was measured as S<sub>21</sub> with a VNA. These results are shown on figure 5.5. It can be seen that the losses increase linearly with frequency, and that obviously, they are more important when the cable

is longer. The losses become very significant, in X-Band, as can be seen with the 33-foot cable, where they amount to 14 dB.

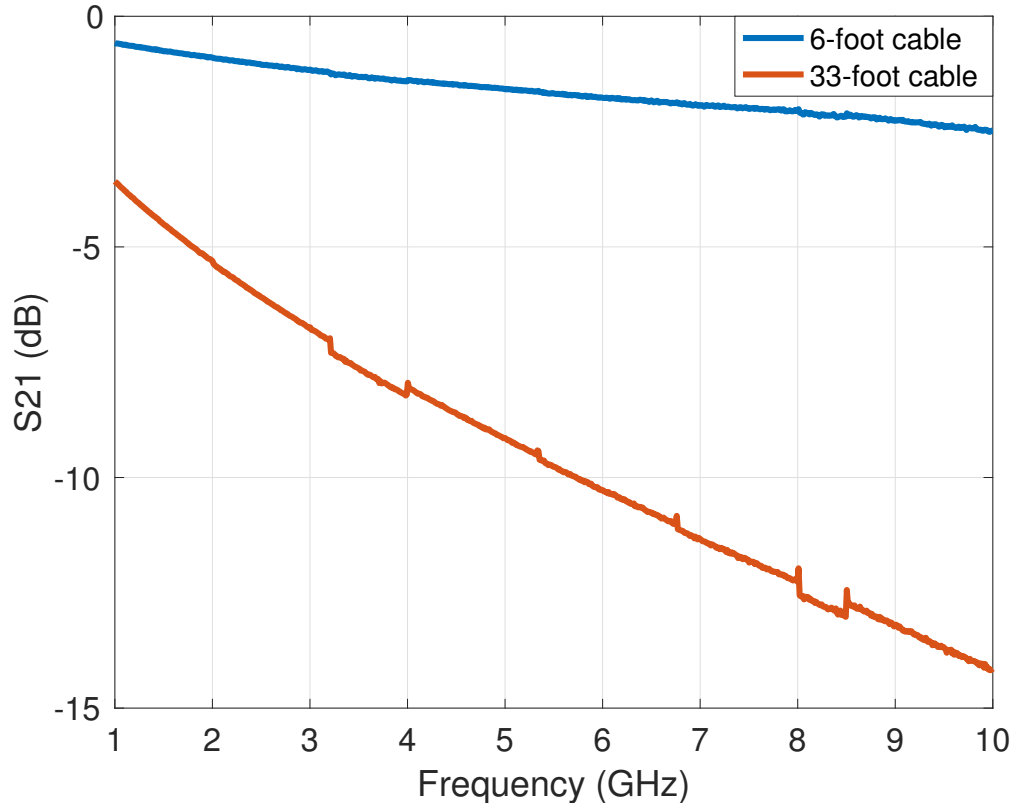


Figure 5.5: The losses versus frequency for both cables: 6-foot (blue) and 33-foot (red).

## 5.2 Source Modeling

Similarly to section 3.4.2, numerical simulations in Wipl-D were carried out to see how the structure of the UAV affects the antenna patterns of the probe. Since only V-polarization measurements were carried out, the simulations were run for a vertical  $\frac{\lambda}{4}$  monopole next one of the arms of the DJI Phantom 3. This arrangement can be seen on figure 5.6 a). Since the monopole has a very broad antenna pattern,

it is illuminating most of the UAV, as can be seen on figure 5.6 a), by the high current densities on the structure. This obviously causes the antenna patterns to be strongly affected, as can be seen on figure 5.6 b), c), and d). The cross-polarization levels are highly raised, about 15 to 20 dB in the D-Plane and the H-Plane. The co-polarization patterns are ripply, up to 3 to 4 dB in each plane. It is also interesting to note that in both the D-plane and the H-Plane, the co-polarization pattern loses from 5 to 10 dB for angles greater than 10 degrees.

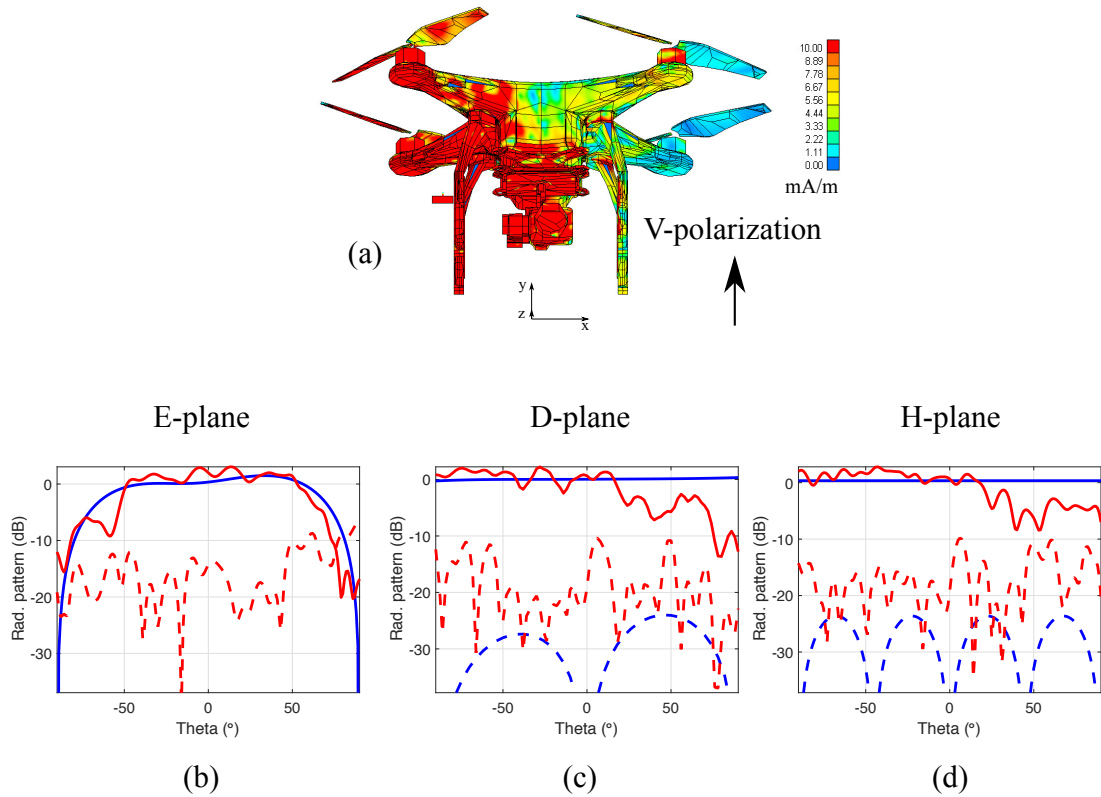


Figure 5.6: Effect of the UAV structure on the antenna pattern:  $\frac{\lambda}{4}$  monopole, vertically polarized. (a) Current density on the probe and the UAV structure. (b) E-Plane antenna patterns with and without the UAV (red and blue respectively). (c) D-Plane antenna patterns with and without the UAV (red and blue respectively). (d) H-Plane antenna patterns with and without the UAV (red and blue respectively).

## 5.3 Indoor Measurements

This part aims at characterizing the AUT in an ideal environment devoid of any reflections caused by the ground and the outdoor surroundings. Neither the vector network analyzer, nor the positioner of the indoor far-field chamber were used. Instead our own setup described above was used. Using this RF system gives more realistic reference measurements with which the outdoors measurements can be compared. Four different kinds of measurements were carried out. The first measurement, considered as a reference case, consisted in using the antenna monopole as a probe without the UAV platform. The result is illustrated in red in Figure 5.7 (bottom). For the second measurement, the antenna probe is mounted on the frame of the UAV when it is turned off. The result, which is illustrated in green in the same figure, shows no impact of the Phantom 3 on the AUT radiation pattern cut. The third measurement, illustrated in blue, represents the AUT radiation pattern cut when the UAV blades are rotating, but when the UAV is not flying. Similarly to the previous case, where the UAV's blades are moving, the AUT radiation pattern cut is not affected. For the fourth measurement, the Phantom 3 was in hovering mode. A Visual Positioning System (VPS) based on ultrasound sensors and a camera, in addition to high contrast line grids, were used to keep the UAV stable. The AUT radiation pattern cut, shown in black in this case, is overlapped with the previous measurements. Discrepancies of about 2 dB were observed. These discrepancies can be attributed to the lack of accuracy of the VPS for indoor application, and also

to the magnitude oscillation of the probe pattern, as could be seen in the previous paragraph.

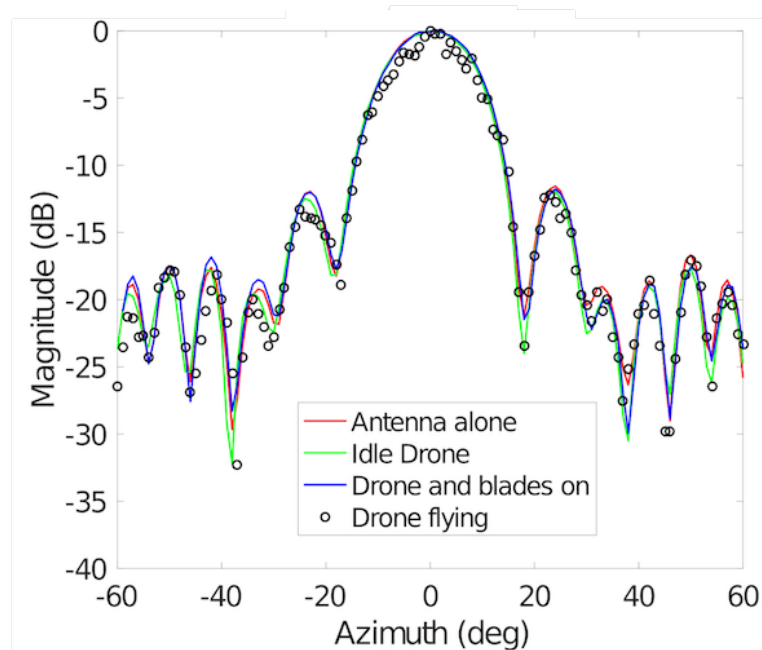
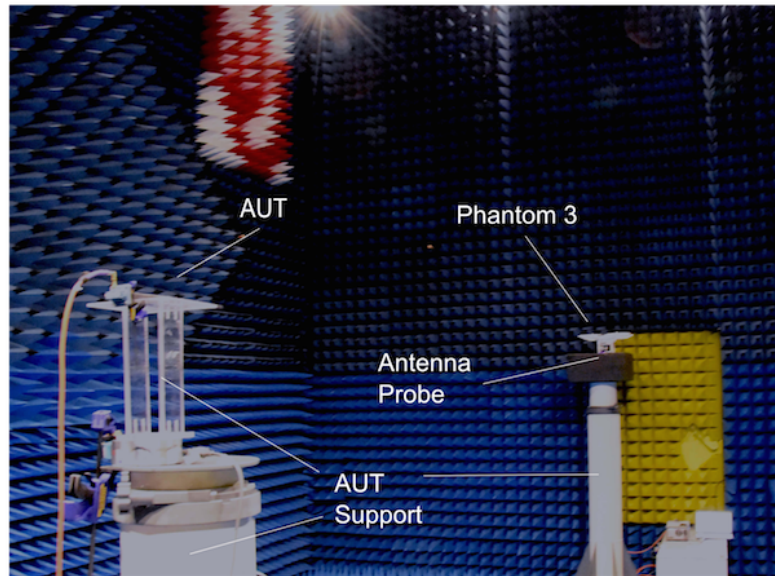


Figure 5.7: The indoor arrangement—top—and results—bottom. The testings were carried out inside a FF anechoic chamber at the ARRC, with the setup represented in figure 5.2. The results show 4 different patterns: the probe without the UAV, the probe with the UAV off, the probe with the UAV on and not flying, and the probe with the UAV hovering.

## 5.4 Outdoor Measurements

In this paragraph, the AUT patterns were measured outside at KAEFS (Kessler Atmospheric and Ecological Field Station), an OU facility. The setup considerations are identical to those of the previous section. In this experiment two measurements were performed: a) Measurement of the AUT in scanning mode while the UAV was in hovering mode. b) Measurement of the AUT while the UAV was flying in a circular pattern around it.

The results can be seen in Figures 5.8 d) and e). The reference pattern cut shown in red was measured with the monopole mounted on a mast. In Figures 5.8 d), the measured pattern cut when the UAV is hovering is shown. It exhibits discrepancies in the order of 2.7 dB in the main beam, and 3 dB in the sidelobe region. The ripples can be attributed to several factors : the windy conditions (12 mph), the standard GPS accuracy as well as a non-zero roll angle because of payload and the ripples in the probe pattern. In Figure 5.8 e), the AUT pattern cut when the UAV was flying around is shown. It is seen that a better agreement was reached because the UAV was more stable in the circular flight pattern than the hovering mode.

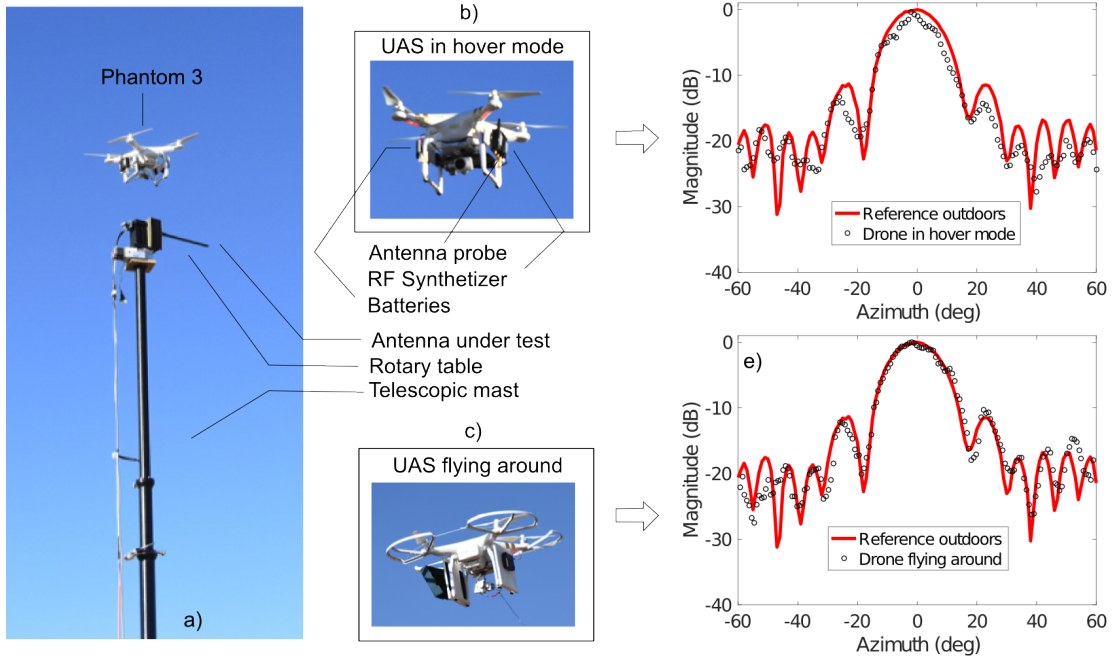


Figure 5.8: The outdoor arrangement alongside the results. a) shows the UAV in the sky in the background and the AUT on its turntable and telescopic mast in the foreground. b) shows the UAV in hover mode with the corresponding antenna pattern on the right. c) shows the UAV in flight mode—circular scan, with the corresponding antenna pattern on the right.

## 5.5 Summary

In this section, a preliminary version of the UAV-based in situ antenna characterization system was presented. First, the setup was thoroughly described, describing each component specifically. The modeling of the probe used on the UAV, a  $\frac{\lambda}{4}$  X-Band monopole, was presented, and it was found that the antenna patterns were very affected, up to 5 dB with respect to the intrinsic antenna patterns. Then an indoor measurement campaign was presented, in an effort to establish a reference antenna pattern for the AUT in an ideal environment devoid of reflections, to establish the effect of the UAV structure on the measurements, and to study the efficacy

of its VPS and how much error it introduces on the measurements. It was found that a maximum of 2 dB was present with respect to the reference, when the VPS was used. Other cases showed perfect agreement with the reference. Finally the results of an outdoor measurement campaign were presented, for both the case where the UAV hovers and the AUT rotates, and the UAV flies around the AUT when it is not moving. Discrepancies of up to 3 dB were found in both cases.

## Chapter 6

### Conclusion

The need to characterize antennas in their operational environments is real, to account for it when measuring their performances. This is what has driven the development of this thesis. As early as 1965, research scientists were striving to carry out this task, with just a probe attached to a balloon, [6]. A more precise technique, involving a helicopter with a probe mounted on it, appeared in 1988, but remains hard to implement and very costly, [7], [8]. As UAVs became available to the public with the capability of flying according to pre-defined user missions and carrying payloads of a few pounds, the helicopter could be replaced with the UAV, [10]. However, the work that has been done so far with this technique involves VHF and UHF antennas only, pointing at zenith, and with low directivity. This greatly simplifies the measurements. A similar system was proposed to tackle the task of in situ antenna characterization, on a more general scale.

Antenna requirements were first listed for weather and airport surveillance radars, as well as 5G antennas. Weather radars have particularly stringent requirements on the beamwidth—less than a degree—, the gain—about 45 dBi—, as well as the cross-polarization isolation—less than 40 dB. For 5G base station antennas, the only true requirement is a gain of about 30 dBi. General measurement requirements were studied, particularly phase and amplitude taper requirements over the AUT

aperture, as well as the effect of ground reflections for large distances between the probe and the AUT, and link budget requirements. It was discovered that for very directive antennas, such as weather radars, the FF distance has to be carefully chosen to be able to measure the first sidelobe accurately. Namely,  $\frac{8a^2}{\lambda}$  should be used instead of the standard  $\frac{2a^2}{\lambda}$ . Subsequently, it was seen that the amplitude taper over the AUT aperture has no effect on the measurements even if a  $3 \times 3$  patch antenna array is used as a probe. It was shown that ground reflections can make the electric field at the AUT aperture vary between zero and twice the incident value, for large distances between the probe and the AUT. Finally, link budget analysis was carried out for the WSR-88D, the RaXPOL, and a typical 5G base station antenna. With a noise floor of 80 dBW and a  $3 \times 3$  patch antenna array, the SNR remained above a detectable threshold for all of these cases to measure the antenna patterns.

Then, design considerations and tradeoffs pertaining to the use of UAVs were exposed. Namely, scanning strategies, ground reflections—more thoroughly than in chapter 2—, positioning accuracy, as well as the probe antenna patterns in presence of the UAV structure were discussed. For each scanning strategy—spherical, cylindrical, and planar—, equations were derived for the distance to be covered to measure a cut. They were illustrated through the same 3 cases as before. Unsurprisingly, the spherical scan is the most efficient in terms of mission distance, and therefore time. Then the emphasis was put on a thorough analysis of ground reflections, without any approximation this time. Once again, considering the same 3 relevant cases, their effect on antenna pattern measurements was shown. It was seen that when the reflected ray is captured in the sidelobes of the AUT, the effect

of ground reflections is greatly mitigated. Subsequently, the positioning accuracy of the critical UAV components, for the in-house ARRC hexacopter, was studied: for standard GPS, RTK GPS, IMUs, and gimbals. Particularly, the real advantage of the RTK GPS over the standard GPS was set forth, with an improvement of 2 orders of magnitude on the positioning accuracy. It was also observed that the UAV can improve its positioning accuracy, compared to that of the GPS, thanks to the Kalman filter onboard that uses GPS, IMU, and barometer data. The gimbal system was not found to have significant positioning drift. The effects of the UAV position and gimbal drifts on the measurements were formulated theoretically. The position drift effect was illustrated through the three relevant cases, and found to be significant for RaXPol and the 5G base station antenna. RTK or PPK can correct these errors in post-processing. The gimbal drift effect was found to be insignificant, if under  $1^\circ$ , regardless of the probe directivity. The antenna patterns of the probe mounted on the UAV were studied. Three platforms, the ARRC in-house octocopter and hexacopter, as well as the commercial DJI Phantom 3, were studied with the central embedded element of a dual-polarized  $3 \times 3$  array. Then the focus was placed on the hexacopter with 3 more excitations of the same array: central row, central column, and all elements. Finally a study with the same hexacopter but with a  $2 \times 2$  version of the array, with all elements excited, was presented. It was found that the more directive the probe, the less its patterns are affected. Similarly the smaller the UAV structure, the less the patterns are affected. The central column, and all elements of the  $3 \times 3$  array are the best configurations, because the patterns are almost unaffected by the UAV structure. The power divider/combiners might

be harder to design for these configurations however. This is why the  $2 \times 2$  array was considered as an option, since the power divider/combiner is easier to devise for this configuration. Unfortunately, its patterns were found to be more ripply.

In chapter 4, the emphasis was put on how to design a UAV for in situ antenna characterization. First UAVs were classified in four different groups: lighter than air, heavier than air, and each of these separated in motorized and non-motorized categories. An evaluation, according to different factors, of 3 different types of aircraft was done. It was found that multirotors, belonging to the heavier than air and motorized aircraft category, was the best suited thanks to its ease of use, maneuverability, low-speed and stationary flight capabilities, and payload capacity. Following this, the dynamics of the multirotor were presented, and it was seen that maneuverability was indeed easy since only the change in motor speeds, together, or with respect to one another is needed to fly. However, it was seen that the model is highly non-linear and coupled, rendering the control task a challenge. The block diagram of a typical multirotor was presented and illustrated with pictures. Finally, the design flow of a UAV was set forth. The frame is chosen first, as it determines the propeller size—important for efficiency and therefore flight time—, flight redundancy through the number of arms, and how big the gimbal can be. The latter is then chosen according to its dimensions and payload capacity. Once the weight estimate of the platform was established, and the propeller size chosen—which is limited by the frame size—, the motors were specified and ESCs matching their maximum current draw were chosen. Finally, the rest of the components were selected.

In the final chapter, a preliminary version of the UAV-based in situ antenna characterization system was presented. First, the setup was thoroughly described, describing each component specifically. The modeling of the probe used on the UAV, a  $\frac{\lambda}{4}$  X-Band monopole, was presented, and it was found that the antenna patterns were very affected, up to 5 dB with respect to the intrinsic antenna patterns. Then an indoor measurement campaign was presented, in an effort to establish a reference antenna pattern for the AUT in an ideal environment devoid of reflections, to establish the effect of the UAV structure on the measurements, and to study the efficacy of its VPS and how much error it introduces on the measurements. It was found that a maximum of 2 dB was present with respect to the reference, when the VPS was used. Other cases showed perfect agreement with the reference. Finally the results of an outdoor measurement campaign were presented, for both the case where the UAV hovers and the AUT rotates, and the UAV flies around the AUT when it is not moving. Discrepancies of up to 3 dB were found in both cases.

This thesis has laid down requirements and tradeoffs for in situ antenna characterization using UAVs, and has established the proof of concept. A system which permits repeatable and reliable characterization of weather radar systems and 5G base station antennas particularly, needs to be implemented. It starts with using a UAV carrying a probe whose antenna patterns are almost unaffected by the structure, as outlined in chapter 3.4. Ideally the UAV should be equipped with a RTK system to benefit from its positioning accuracy, but PPK is sufficient to correct for the position errors, reported in 3.3 in post-processing. The UAV also needs to be able to implement the scanning strategies discussed in chapter 3.1, as well as

provide a common timestamp between its position and the AUT measurements to reconstruct the antenna patterns. Finally, following the recommendations of chapter 3.2, the measurement configuration must be carefully chosen as to mitigate the ground reflections as much as possible. The first measurement campaign will aim at characterizing the Advanced Technology Demonstrator (ATD) from Massachusetts Institute of Technology (MIT) Lincoln Laboratories. The ATD is the demonstrator for the MPAR project. Appendix B features the same analysis that was done for the WSR-88D, RaXPoI, and the 5G base station antenna, for the ATD. The ATD has the following characteristics:

- It comprises 76 panels for a total of 4864 elements.
- It has an area of 12.6 m<sup>2</sup> and a maximum dimension of 4.06 m.
- It has a gain of 42.3 dBi, beamwidths of 1.7° in azimuth and 1.6° in elevation, a peak power of 58.4 kW, and operates at 3.1 GHz.

## Bibliography

- [1] “IEEE Standard Test Procedures for Antennas,” *ANSI/IEEE Std 149-1979*, p. s, 1979.
- [2] B. Isom, R. Palmer, R. Kelley, J. Meier, D. Bodine, M. Yeary, B.-L. Cheong, Y. Zhang, T. Y. Yu, and M. I. Biggerstaff, “The Atmospheric Imaging Radar: Simultaneous Volumetric Observations Using a Phased Array Weather Radar,” *Journal of Atmospheric and Oceanic Technology*, vol. 30, no. 4, pp. 655–675, 2013.
- [3] A. L. Pazmany, J. B. Mead, H. B. Bluestein, J. C. Snyder, and J. B. Houser, “A Mobile Rapid-Scanning X-band Polarimetric (RaXPoL) Doppler Radar System,” *Journal of Atmospheric and Oceanic Technology*, vol. 30, no. 7, pp. 1398–1413, 2013.
- [4] B. L. Cheong, R. Kelley, R. D. Palmer, Y. Zhang, M. Yeary, and T. Y. Yu, “PX-1000: A Solid-State Polarimetric X-Band Weather Radar and Time-Frequency Multiplexed Waveform for Blind Range Mitigation,” *IEEE Transactions on Instrumentation and Measurement*, vol. 62, pp. 3064–3072, Nov 2013.
- [5] G. Zhang, S. Karimkashi, L. Lei, R. Kelley, J. Meier, R. Palmer, C. Futon, R. J. Doviak, A. Zahrai, and D. S. Zrnic, “A Cylindrical Polarimetric Phased Array Radar Concept A Path to Multi-mission Capability,” in *2013 IEEE International Symposium on Phased Array Systems and Technology*, pp. 481–484, Oct 2013.
- [6] J. Steele, “Measurement of antenna radiation patterns using a tethered balloon,” *IEEE Transactions on Antennas and Propagation*, vol. 13, pp. 179–180, Jan 1965.
- [7] J. E. Lejerkranz and F. Enquist, “Field strength measurement and antenna radiation pattern plotting using heli-borne equipment,” in *1988 International Broadcasting Convention, IBC 1988*, pp. 137–142, Sep 1988.
- [8] R. G. Manton and K. L. Beeke, “HF antenna radiation patterns over real terrain,” in *1988 International Broadcasting Convention, IBC 1988*, pp. 143–147, Sep 1988.
- [9] C. Raucy, E. de Lera Acedo, N. Razavi-Ghods, D. Gonzalez-Ovejero, and C. Craeye, “Low-cost near field pattern measurement technique for aperture array characterization,” in *2013 7th European Conference on Antennas and Propagation (EuCAP)*, pp. 661–665, April 2013.
- [10] G. Virone, A. M. Lingua, M. Piras, A. Cina, F. Perini, J. Monari, F. Paonessa, O. A. Peverini, G. Addamo, and R. Tascone, “Antenna Pattern Verification

System Based on a Micro Unmanned Aerial Vehicle (UAV),” *IEEE Antennas and Wireless Propagation Letters*, vol. 13, pp. 169–172, 2014.

- [11] G. Virone, F. Paonessa, O. A. Peverini, G. Addamo, R. Orta, R. Tascone, A. Lingua, M. Piras, P. Bolli, G. Pupillo, and J. Monari, “Antenna pattern measurement with UAVs: Modeling of the test source,” in *2016 10th European Conference on Antennas and Propagation (EuCAP)*, pp. 1–3, April 2016.
- [12] F. Paonessa, G. Virone, P. Bolli, G. Pupillo, J. Monari, F. Perini, A. Mattana, G. Naldi, M. Poloni, M. Schiaffino, A. M. Lingua, M. Piras, P. Dabove, I. Aicardi, G. Addamo, O. A. Peverini, R. Orta, and R. Tascone, “The UAV-based test source as an end-to-end verification tool for aperture arrays,” in *2016 International Conference on Electromagnetics in Advanced Applications (ICEAA)*, pp. 886–889, Sept 2016.
- [13] F. Paonessa, G. Virone, E. Capello, G. Addamo, O. A. Peverini, R. Tascone, P. Bolli, G. Pupillo, J. Monari, M. Schiaffino, F. Perini, S. Rusticelli, A. M. Lingua, M. Piras, I. Aicardi, and P. Maschio, “VHF/UHF antenna pattern measurement with unmanned aerial vehicles,” in *2016 IEEE Metrology for Aerospace (MetroAeroSpace)*, pp. 87–91, June 2016.
- [14] F. Paonessa, G. Virone, I. Aicardi, A. M. Lingua, M. Piras, P. Maschio, P. Bolli, G. Addamo, O. A. Peverini, R. Orta, and R. Tascone, “Recent results in antenna pattern measurement with UAVs,” in *2015 International Conference on Electromagnetics in Advanced Applications (ICEAA)*, pp. 720–721, Sept 2015.
- [15] G. Virone, F. Paonessa, E. Capello, O. A. Peverini, G. Addamo, R. Tascone, R. Orta, M. Orefice, A. Lingua, M. Piras, I. Aicardi, P. Bolli, J. Monari, F. Perini, G. Pupillo, and M. Schiaffino, “UAV-based antenna and field measurements,” in *2016 IEEE Conference on Antenna Measurements Applications (CAMA)*, pp. 1–3, Oct 2016.
- [16] G. Virone, F. Paonessa, O. A. Peverini, G. Addamo, R. Orta, R. Tascone, and P. Bolli, “Antenna pattern measurements with a flying far-field source (Hexacopter),” in *2014 IEEE Conference on Antenna Measurements Applications (CAMA)*, pp. 1–2, Nov 2014.
- [17] G. Virone, F. Paonessa, A. Tibaldi, Z. Farooqui, G. Addamo, O. A. Peverini, R. Tascone, P. Bolli, A. Mattana, J. Monari, G. Naldi, F. Perini, G. Pupillo, M. Schiaffino, A. M. Lingua, M. Piras, P. Maschio, I. Aicardi, I. H. Bendea, and A. Cina, “UAV-based radiation pattern verification for a small low-frequency array,” in *2014 IEEE Antennas and Propagation Society International Symposium (APSURSI)*, pp. 995–996, July 2014.
- [18] F. Paonessa, G. Virone, G. Addamo, O. A. Peverini, R. Tascone, E. de Lera Acedo, E. Coln-Beltrn, N. Razavi-Ghods, P. Bolli, G. Pupillo, G. Naldi, J. Monari, A. M. Lingua, M. Piras, I. Aicardi, and P. Maschio, “UAV-based pattern measurement of the SKALA,” in *2015 IEEE International*

*Symposium on Antennas and Propagation USNC/URSI National Radio Science Meeting*, pp. 1372–1373, July 2015.

- [19] F. Üstner, E. Aydemir, E. Güle, M. İlarıslan, M. Çelebi, and E. Demirel, “Antenna radiation pattern measurement using an unmanned aerial vehicle (UAV),” in *2014 XXXIth URSI General Assembly and Scientific Symposium (URSI GASS)*, pp. 1–4, Aug 2014.
- [20] A. M. Picar, C. Marqu, M. Anciaux, H. Lamy, and S. Ranvier, “Antenna pattern calibration of radio telescopes using an UAV-based device,” in *2015 International Conference on Electromagnetics in Advanced Applications (ICEAA)*, pp. 981–984, Sept 2015.
- [21] S. Duthoit, J. L. Salazar, W. Doyle, A. Segales, B. Wolf, C. Fulton, and P. Chilson, “A new approach for in-situ antenna characterization, radome inspection and radar calibration, using an Unmanned Aircraft System (UAS),” in *2017 IEEE Radar Conference (RadarConf)*, pp. 0669–0674, May 2017.
- [22] M. Skolnik, *Radar Handbook*. McGraw-Hill, second ed., 1990.
- [23] F. H. Raab, R. Caverly, R. Campbell, M. Eron, J. B. Hecht, A. Mediano, D. P. Myer, and J. L. B. Walker, “HF, VHF, and UHF systems and technology,” *IEEE Transactions on Microwave Theory and Techniques*, vol. 50, pp. 888–899, Mar 2002.
- [24] R. J. Doviak, “A Memorandum on Comparisons of Weather and Aircraft Surveillance Radar requirements to Determine Key Features for a 10-cm MPAR,” tech. rep., National Severe Storms Laboratory,, 2015.
- [25] R. Doviak, M. Weber, and D. Zrníc, “Comparisons of weather and aircraft surveillance radar requirements to determine key features for a 10-cm multi-function phased array radar,” in *2016 IEEE International Symposium on Phased Array Systems and Technology (PAST)*, pp. 1–6, Oct 2016.
- [26] FAA, “Multifunction Phased Array Radar (MPAR); Notional Functional Requirements Document,” tech. rep., Federal Aviation Administration, April 2015.
- [27] C. Fulton, J. Herd, S. Karimkashi, G. Zhang, and D. Zrníc, “Dual-polarization challenges in weather radar requirements for multifunction phased array radar,” in *2013 IEEE International Symposium on Phased Array Systems and Technology*, pp. 494–501, Oct 2013.
- [28] I. T. Union, “Technical feasibility of IMT in bands above 6 GHz,” Tech. Rep. ITU-R M.2376-0, International Telecommunication Union, jul 2015.
- [29] A. I. Sulyman, A. T. Nassar, M. K. Samimi, G. R. Maccartney, T. S. Rappaport, and A. Alsanie, “Radio propagation path loss models for 5G cellular networks in the 28 GHz and 38 GHz millimeter-wave bands,” *IEEE Communications Magazine*, vol. 52, pp. 78–86, September 2014.

- [30] T. S. Rappaport, S. Sun, R. Mayzus, H. Zhao, Y. Azar, K. Wang, G. N. Wong, J. K. Schulz, M. Samimi, and F. Gutierrez, “Millimeter Wave Mobile Communications for 5G Cellular: It Will Work!,” *IEEE Access*, vol. 1, pp. 335–349, 2013.
- [31] F. Khan, Z. Pi, and S. Rajagopal, “Millimeter-wave mobile broadband with large scale spatial processing for 5G mobile communication,” in *2012 50th Annual Allerton Conference on Communication, Control, and Computing (Allerton)*, pp. 1517–1523, Oct 2012.
- [32] M. Matin, “Review on Millimeter Wave Antennas- Potential Candidate for 5G Enabled Applications,” vol. 5, p. 98, 12 2016.
- [33] S. Rajagopal, S. Abu-Surra, Z. Pi, and F. Khan, “Antenna Array Design for Multi-Gbps mmWave Mobile Broadband Communication,” in *2011 IEEE Global Telecommunications Conference - GLOBECOM 2011*, pp. 1–6, Dec 2011.
- [34] C. A. Balanis, *Antenna Theory: Analysis and Design, 3rd Edition*. Wiley, 2005.
- [35] C. C. Cutler, A. P. King, and W. E. Kock, “Microwave Antenna Measurements,” *Proceedings of the IRE*, vol. 35, pp. 1462–1471, Dec 1947.
- [36] F. T. U. Josef Cihlar, “Dielectric Properties of Soils as a Function of Moisture Content,” Tech. Rep. NANA-CR-141868, Remote Sensing Laboratory, nov 1974.
- [37] “Evaluating inertial measurement units,” in <https://www.edn.com>.
- [38] S. Vatansever and I. Butun, “A broad overview of GPS fundamentals: Now and future,” in *2017 IEEE 7th Annual Computing and Communication Workshop and Conference (CCWC)*, pp. 1–6, Jan 2017.
- [39] “WIPL-D,” in <https://www.wipl-d.com>.
- [40] S. Bouabdallah, P. Murrieri, and R. Siegwart, “Design and control of an indoor micro quadrotor,” in *Robotics and Automation, 2004. Proceedings. ICRA '04. 2004 IEEE International Conference on*, vol. 5, pp. 4393–4398 Vol.5, April 2004.
- [41] S. T. Duthoit, *General Exam: Modelling and Control of a Multirotor Vehicle*.
- [42] “DJI Phantom,” in <http://www.harveynorman.ie>.
- [43] E. Lavretsky and K. A. Wise, “Robust adaptive control,” in *Robust and Adaptive Control*, Springer, 2013.
- [44] “Advanced MultiCopter Design,” in <http://ardupilot.org>.
- [45] “How to choose the right motor for your multicopter drone,” in <http://www.dronetrest.com>.

[46] “The UAV Guide: Propeller,” in *<http://wiki.theuavguide.com>*.

[47] “What to consider when buying a ESC for your multicopter,” in *<http://www.dronetrest.com>*.

# Appendix A

## Hexacopter part list

Table A.1: Part list of the ARRC in-house hexacopter

Part type	Part model	Price (\$)
Frame	DJI S900 frame	1200
Propulsion system	DJI E1200 Pro	$270 \times 6$
BEC	CC BEC Pro 20A	35
Flight controller + GPS + Telemetry	Pixhawk + NEO-M8N + 3DR	170
Gimbal	Infinity MR S2	950
RC	Spektrum DX9	450
Receiver	Spektrum DSMX	35
Battery	Multistar 20 Ah 6S 10C	449

## Appendix B

### ATD

#### B.1 Link Budget

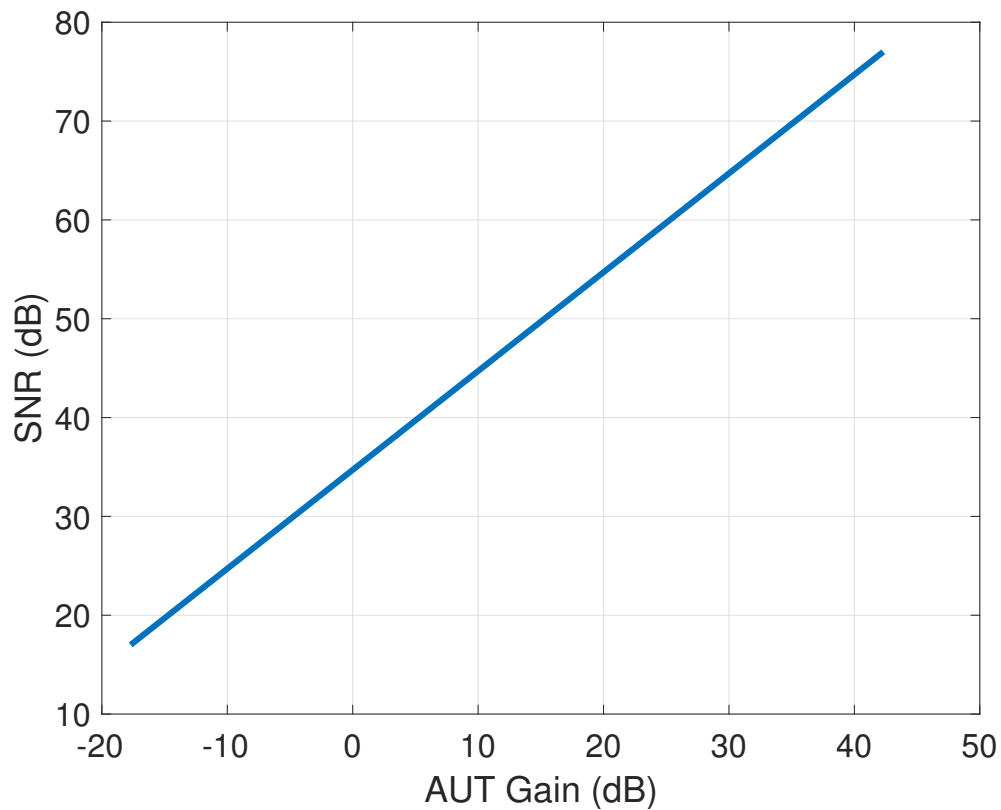


Figure B.1: Link budget (SNR) for the ATD versus its antenna gain. Parameters for these antennas are summed up in appendix B. The FF distance was chosen according to the  $8\frac{a^2}{\lambda}$  criterion for accurate sidelobe level measurements. A 12-dBi  $3\times 3$  patch antenna array was used, and the noise floor is -80 dBW.

## B.2 Scan Types

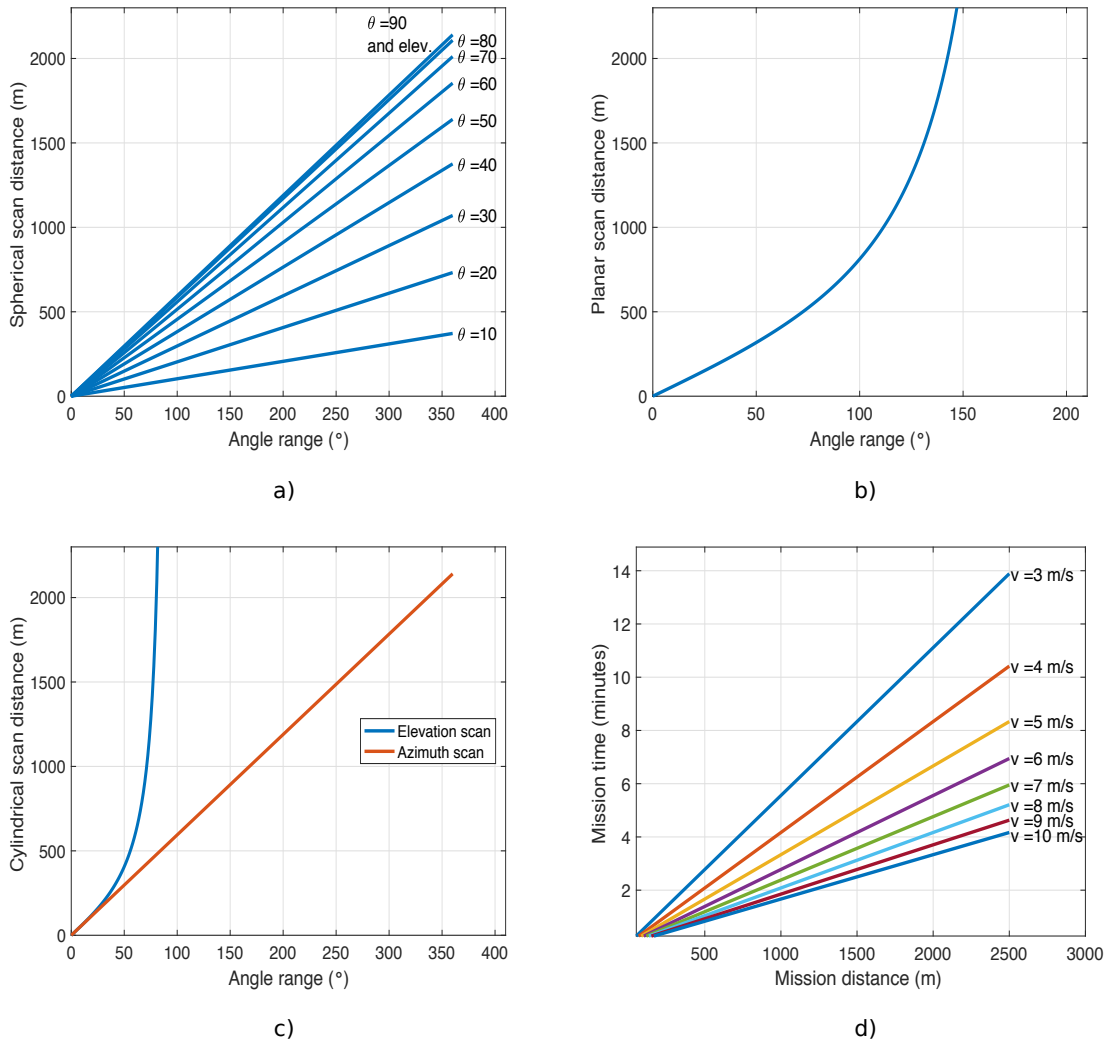


Figure B.2: The different scanning strategies illustrated with the ATD at a FF distance of 341 m. The distance to be covered is shown versus the range of angles covered for the measured cut. The time needed to cover a certain distance with the UAV is shown, for different flight speeds. a) shows the spherical scan at different elevation angles in azimuth, while the elevation scans are represented by the azimuth scan at  $\theta = 90^\circ$ . b) shows the planar scan in the  $x - y$  plane above the antenna. c) shows the cylindrical scan both in azimuth in elevation. d) shows the time needed for the UAV to complete a mission of a given distance, for different speeds.

## B.3 Ground Reflections

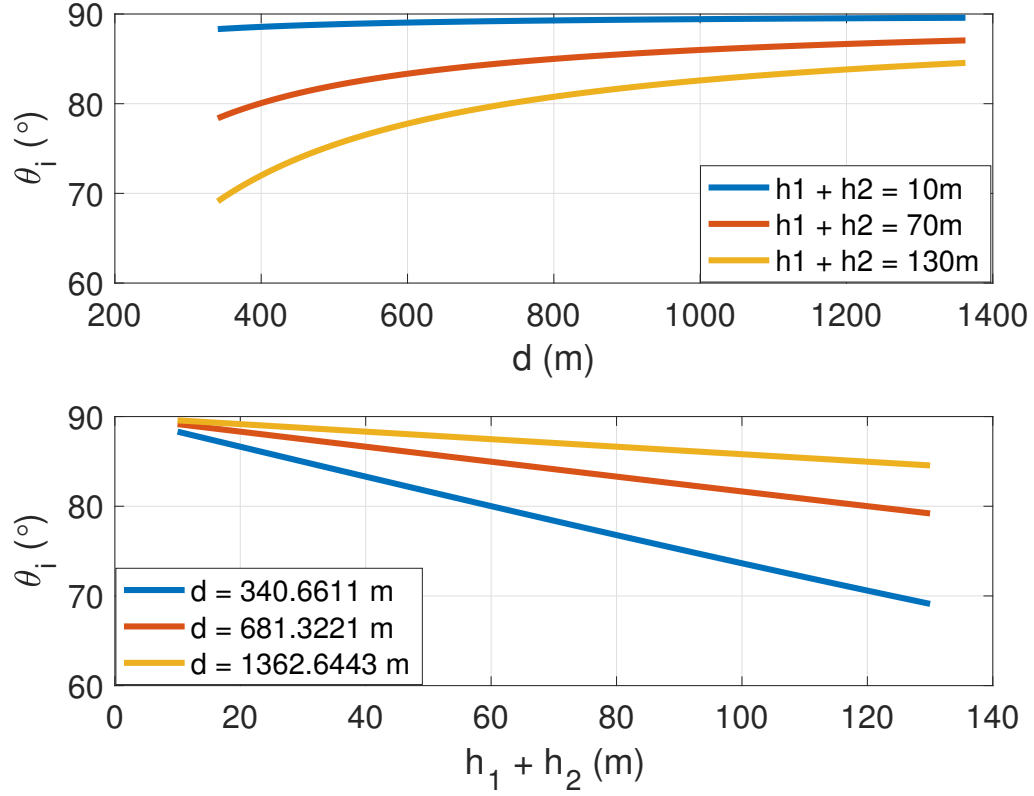


Figure B.3: Incident angle  $\theta_i$  for the ATD. The top plot shows  $\theta_i$  versus distance for 3 different values of  $h_1 + h_2$ , representing low, medium, and maximum. The bottom plot shows  $\theta_i$  versus  $h_1 + h_2$  for the 3 different values of the measurement distance, once the FF distance, twice the FF distance, and four times the FF distance.

## B.4 Positioning Accuracy

Table B.1: Effect of the UAV position drift on  $\Delta\Phi$ ,  $\Delta\theta$ , and  $\Delta PL$  for the ATD

	$\Delta\Phi_{max}(\circ)$	$\Delta\theta_{max}(\circ)$	$\Delta PL_{max}(dB)$
ATD	0.17	0.25	0.026